# FEEDBACK CONTROL OF A PERMANENT MAGNET BIASED, HOMOPOLAR MAGNETIC BEARING SYSTEM

A Thesis

by

VISHAL ASHOK WADHVANI

Submitted to the Office of Graduate Studies of
Texas A&M University
in partial fulfillment of the requirements for the degree of

MASTER OF SCIENCE

May 2011

Major Subject: Mechanical Engineering

# FEEDBACK CONTROL OF A PERMANENT MAGNET BIASED, HOMOPOLAR MAGNETIC BEARING SYSTEM

A Thesis

by

VISHAL ASHOK WADHVANI

Submitted to the Office of Graduate Studies of
Texas A&M University
in partial fulfillment of the requirements for the degree of

MASTER OF SCIENCE

Approved by:

| | |
|---|---|
| Chair of Committee, | Alan B. Palazzolo |
| Committee Members, | Bryan P. Rasmussen |
| | Rashid Abu Al-Rub |
| Head of Department, | Dennis O'Neal |

May 2011

Major Subject: Mechanical Engineering

# ABSTRACT

Feedback Control of a Permanent Magnet Biased, Homopolar Magnetic Bearing System. (May 2011)

Vishal Ashok Wadhvani, B.E., University of Pune

Chair of Advisory Committee: Dr. Alan B. Palazzolo

Magnetic bearings are increasingly being used in a wide variety of applications in the industry such as compressors, turbines, motors, generators etc. Also, there are different types available depending upon their construction. The research presented here investigates a high temperature permanent magnet biased magnetic bearing system which is jointly being researched by National Aeronautics and Space Administration (NASA) and Electron Energy Corporation (EEC). The purpose of this research was to develop a permanent magnet biased magnetic bearing system using high temperature (HT) permanent magnets (PM) developed by EEC. This system was designed for high performance, high temperature (1000F) and high speed applications. The entire system consisted of two radial bearings, two catcher bearings, one axial thrust bearing and a motor. The central rotor shaft is powered by a high temperature permanent magnet motor to be able to run at the designed conditions of 20,000 rpm. This thesis documents the design of a feedback control law that stabilizes this HTPM biased AMB levitated system and summarizes efforts to build a test rig for the HT tests of the machine. A decentralized PD control law is used to achieve successful levitation.

An existing PD analog controller with single input single output (SISO) control law for each axis (previously used for a flywheel test rig) is used as a feedback controller for this HTPM magnetic bearing system. Modeling and simulation of the resulting closed loop system is done in Matlab to test for stability and an iterative approach leads to optimum values of proportional and derivative gain pairs. The notch filter locations are also determined through this closed loop iterative simulation.

# DEDICATION

To my family and friends.

## ACKNOWLEDGEMENTS

I would like to express my sincere thanks to my committee chair Dr. Alan B. Palazzolo for his encouragement, support and patience throughout the course of my research. I would also like to express my gratitude to Dr. Bryan P. Rasmussen and Dr. Rashid Abu Al-Rub for being on my thesis committee and their support.

Special thanks go to Mr. Randall Tucker for his expert guidance in getting the test rig together and providing innovative suggestions. Thanks are extended to Layne Wylie, Cole Easterling, Alex Wendeborn, George Montgomery, my colleague Ashwanth Narain and others who shared time with me; and provided helpful comments and suggestions during the research phase. I would also like to thank Dr. Heeju Choi from the Electron Energy Corporation (EEC) for providing the permanent magnets and support in this project.

Individual thanks to all my friends and the department faculty for making my time at Texas A&M University a wonderful experience. Finally, thanks to my mother and father for their unfettered support and encouragement during the entire course of my study.

# NOMENCLATURE

| | |
|---|---|
| AMB | Active Magnetic Bearing |
| CDM | Current Distribution Matrix |
| DOF | Degree of Freedom |
| EEC | Electron Energy Corporation |
| FTC | Fault Tolerant Control |
| HT | High Temperature |
| NASA | National Aeronautics and Space Administration |
| PD | Proportional Derivative Control law |
| PM | Permanent Magnet |
| SISO | Single Input Single Output Control law |
| TAMU | Texas A&M University |
| TF | Transfer Function |
| VCEL | Vibration Control and Electromechanics Laboratory |

# TABLE OF CONTENTS

Page

Page

Page

## LIST OF FIGURES

Page

Page

Page

Page

Page

Page

Page

## LIST OF TABLES

Page

# 1. INTRODUCTION

## 1.1 Preface

A magnetic bearing is an electromechanical device, in which a means of magnetic field is used to maintain the relative position between a rotating component and the stationary component. Magnetic bearings can be broadly categorized into two types: passive and active. In general, a passive magnetic bearing is made with permanent magnets, while an active magnetic bearing (AMB) is made with electromagnets and depending on its construction can have permanent magnets as helper poles. The present work focuses on a Homopolar permanent magnet biased AMB, and a simplified block diagram of the commonly used magnetic bearings is shown in Figure 1-1.

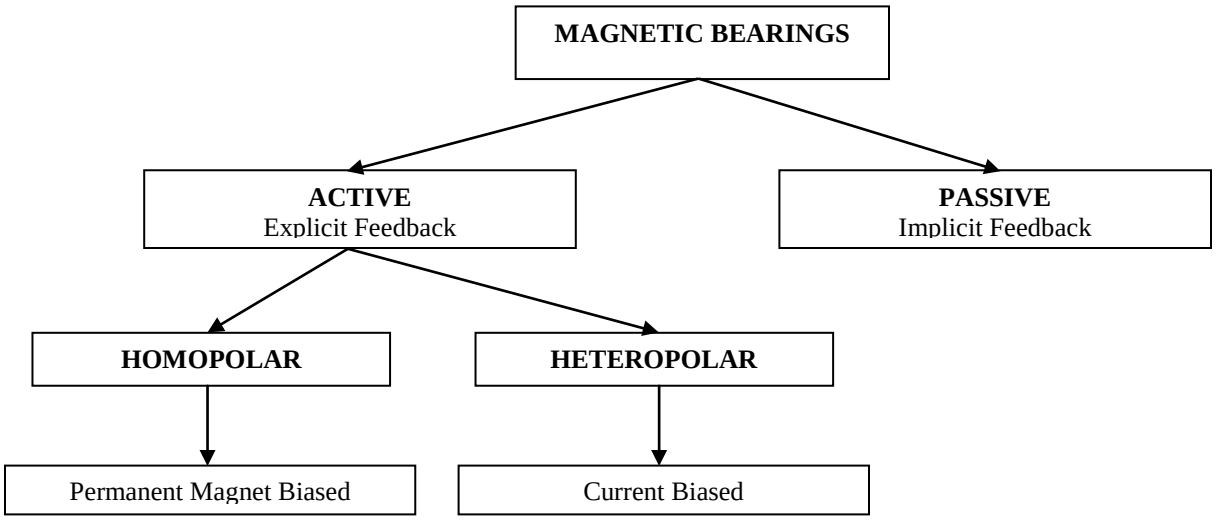


Figure 1-1 Broad classification of commonly used magnetic bearings [1]

---

This thesis follows the style and format of *Journal of Mechanical Design.*

Heteropolar Magnetic Bearings- The principle of operation for these bearings is shown in Figure 1-2(a). If we consider a particular axial location, the bias flux changes direction several times around the circumference of the rotor in the air gap. In these types of bearings, there are many losses which are created due to current constantly being applied to provide the bias flux and change of current flux direction on rotor which increases with speed.

Homopolar Magnetic Bearings- The principle of operation for these bearings is shown in Figure 1-2(b). If we consider a particular axial location, the bias flux stays in the same direction around the circumference of the rotor in the air gap. In these types of bearings, permanent magnets provide the bias flux without any electrical current and hence eliminate additional wiring and energy losses. The control flux, which provides the dynamic magnetic forces, is provided by an electromechanical coil.

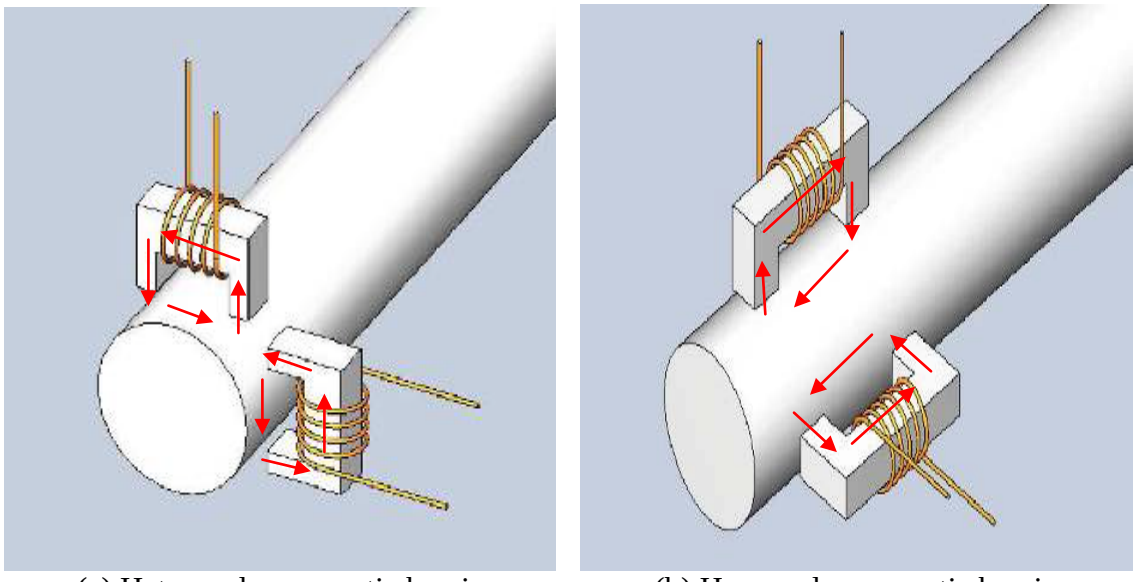

(a) Heteropolar magnetic bearing (b) Homopolar magnetic bearing

Figure 1-2 Working principle of the two different types of magnetic bearings [1]

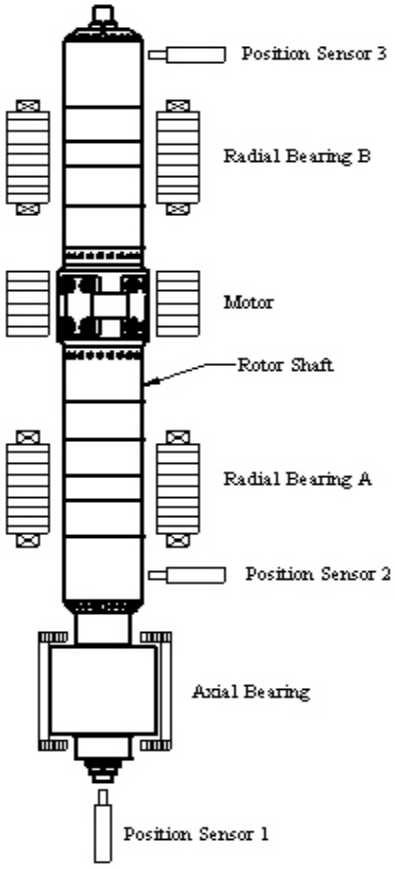


Figure 1-3 Outline of the complete magnetic bearing system

Figure 1-3 shows the general system assembly for the present research work and the components used are labeled explicitly.

In this assembly, there are five DOFs and hence five axes to control. The auxiliary mechanical bearings (catcher bearings) that are often used in conjunction with the magnetic bearings to help during startup conditions while the magnetic bearings are being powered up or as a backup under any failure, are not shown in the above diagram. Feedback control is used to adjust the stiffness and damping parameters of the AMB system, to remove the effects of modal vibrations.

Any rotating body will not exert any variable disturbing force on its supports when the axis of rotation coincides with one of the principal axes of inertia of the body. This is an ideal condition since it is difficult to achieve a perfect mass distribution in the normal process of manufacturing due to errors in machining and material properties of the rotor. Due to this variable centrifugal forces (dependent upon speed) are exerted by the heavier side of the rotor, which produce vibrations.

In case of unbalance of the rotor assembly, two vibration modes (or rigid body modes) are possible: the assembly may rotate about a tilted axis (conical mode (a)) or about a translated parallel axis (b) as shown in Figure 1-4. In the cylindrical mode (latter case), the motion is an orbit of the shaft about its center of mass. Since the effect of unbalance increases with speed, it is a major speed limiting factor. To remove the undesirable effect of these vibrations and establish safe and quiet operation, control becomes necessary.

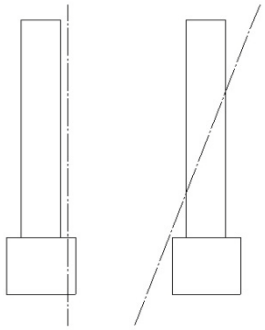

(a) (b)

Figure 1-4 Rigid body modes

Apart from the rigid body modes described above, there also exists bending modes shown in Figure 1-5 due to the flexibility of the rotor and it comes into picture at the high rotational speeds of operation. These bending modes change location with the speed of operation and control of such complicated dynamics become difficult to model and analyze. Each bending mode has a characteristic excitation frequency which might be same as the rotational frequency of the rotor resulting in a catastrophe due to the inability of the Magnetic Bearings to control this oscillation. Since the Magnetic Bearings are located at only two positions along the entire shaft, the control of bending modes which resonate along the entire length of the shaft becomes impossible. Due to this, the design of the control system is done in such a way so as not to excite any bending modes. This is done using moving notch filters; these filters prevent any information at the bending mode frequencies from reaching the AMB controller, thus preventing any controller output at frequencies which would excite the bending modes [2]. For a more complete analysis of an AMB system, higher dimensional models are required.

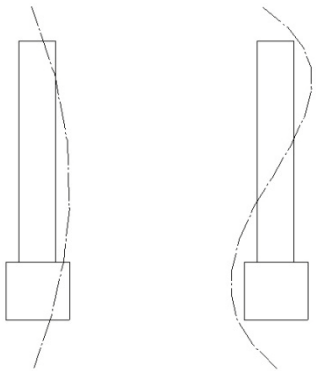

(a) (b)

Figure 1-5 Bending modes

In order to select a bearing for any particular application, there are two major characteristic features (stiffness and damping) which affect their suitability for the application under consideration.

### 1.1.1 *Stiffness*

Using Hooke's Law, the stiffness of a bearing can be shown to be analogous to the spring constant. However, magnetic bearing stiffness can be negative. As can be seen in Figure 1-6, the magnetic force $F_m$ behaves in an opposite way to the mechanical spring force $F_s$: Whereas the latter *increases* and even changes its sign with increasing distance *x*, thus producing a repelling effect which stabilizes the rotor motion around the equilibrium point ($x_0$), the magnetic force *decreases* dramatically with increasing air gap *s* (constant bias current i assumed), which results in an unstable behavior. Thus when a constant current is passed through the electromagnet's coils so as to levitate the rotor to an equilibrium position, then, if the stiffness is positive, the rotor returns to its equilibrium position after a disturbance or load due to the magnetic force (Figure 1-6) resulting in stable behavior. However, if the stiffness is negative, the rotor moves away from the equilibrium point since any disturbance to the rotor position is amplified by the magnetic force. Fortunately, this negative stiffness of a magnetic bearing can be made positive by using feedback control.

### 1.1.2 *Damping*

The amount of damping defines the bearing's ability to dampen vibrations and make the system stable. It depends upon the stiffness in that higher the stiffness, higher

amount of damping should be chosen in order to achieve satisfactory results. Since the amount of damping can be controlled electronically in an active magnetic bearing, it can be easily adapted to the application on field. This is not possible in a passive magnetic bearing systems using permanent magnets and hence restricting their application zone. Generally, an active magnetic bearing uses attractive forces generated by electromagnets to support a rotating shaft. Using a homopolar construction, permanent magnets can be used as helper poles to provide the bias flux while electromagnets are used to provide the control flux (which is the basis for current research work).

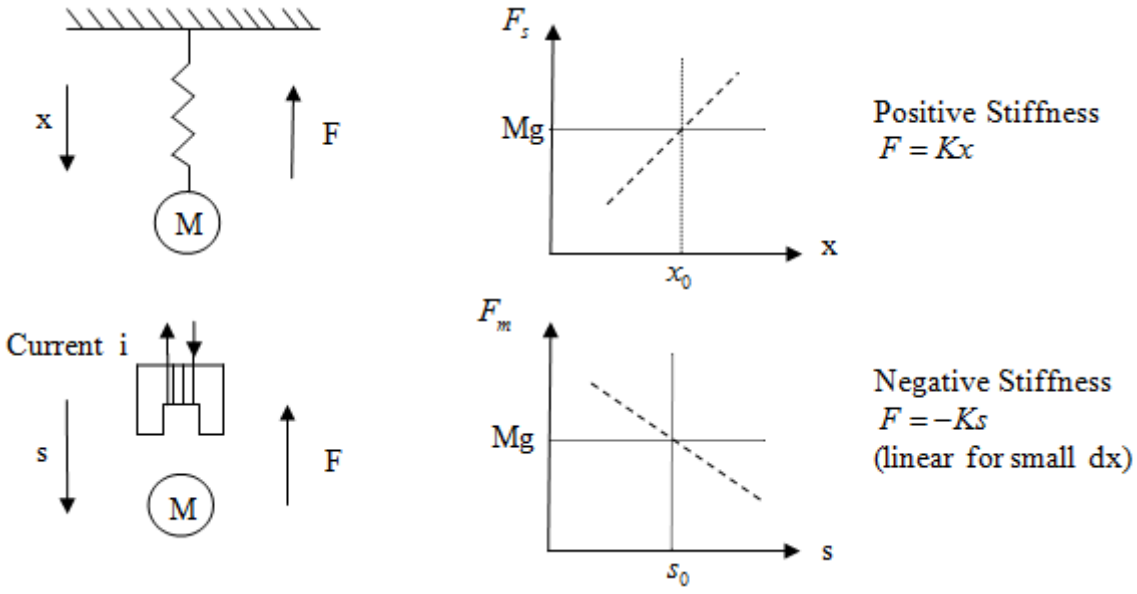


Figure 1-6 Positive and negative stiffness

## 1.2 Objectives

The primary objective of the current research work is:

1. To develop a feedback control system for the permanent magnet biased magnetic bearing system to levitate the spinning rotor at the designed conditions.
2. Conceptualize and fabricate new components as per requirement to assemble all the components of the complete universal magnetic bearing system.
3. Write a Matlab Code to completely simulate the whole magnetic bearing system and test for stability.
4. From the MATLAB code, find the optimal gain (proportional and derivative) set values which result in a maximum value for the minimum value of eigenvalue damping ratio $\zeta$ for any set of PD gains.

## 1.3 Literature review

A collection of point charges cannot be maintained in a stable stationary equilibrium configuration solely by the electrostatic interaction of the forces arising from the charges, was proved by Samuel Earnshaw in 1842 [3]. This law applies to any inverse-square law force field such as electric, magnetic, and gravitation force-fields [4]. These fields are divergenceless $(\nabla \cdot F(x) = 0)$ in free space as they are derived from a potential which satisfies Laplace's equation. Therefore, a stable equilibrium of particles cannot exist and there will be instability in at least one direction i.e. there is no point in empty space where the field of forces is directed inward from all directions thus explaining the nonexistence of a stable passive magnetic bearing system. However, there

are some loopholes where this theorem is not applicable like time-varying fields, diamagnetic materials, ferrofluids and active-feedback systems. An active magnetic bearing feedback system is investigated in the current research work and it is also one of the common methods to circumvent Earnshaw's Theorem [5].

A permanent magnet biased magnetic bearing that has the characteristics of the coplanar geometry is usually known as a homopolar design [6]. This geometry of electromagnetic bearings with permanent magnet bias was described by Meeks et al. [7]. Homopolar bearing designs generally have a permanent magnet in the back-iron to provide the bias flux. Electric coils can also be used in place of permanent magnets to provide for this bias flux to the stators. The supply of bias flux by permanent magnets leads to advantages in the form of reduced electrical power requirements and also as a consequence power lost due to coil current is decreased. Sortore et al. [8] released experimental data that showed significant reduction in power consumption by permanent magnet biased Homopolar bearings. Lee, Hsio, and Ko [9] described various equations and developed advanced circuit models to predict and calculate the flux paths and other parameters for bearings using permanent magnets. A comparison between the predicted and measured force and stiffness characteristics of bearing were performed by Imlach, Blair, and Allaire [10].

This thesis is focused on a certain type of double plane bearing biased with permanent magnets in the poles. Masayuk [11], and Nagaghiko [12] have proposed bearings with magnets in the poles. However, the bearing that are presented here are different in that the poles with permanent magnets are designed for supplying 500 lb.-f at 1000°F and permanent magnets only provide the bias flux.

Palazzolo and Kenny [13] of TAMU-VCEL described the single plane magnetic bearing with permanent magnet that has lower coil resistance. For high temperatures of 1000 °F, Provenza, Palazzolo, Hansen et al. [14] had described the open loop, experimental force and power measurements of a radial magnetic bearing and rotor speeds upto 15,000 rpm. Mohiuddin [15] described and demonstrated the working of a high speed and high temperature electromagnetic axial bearing. Gandhi, Palazzolo et al. [6] provided the development of the high temperature radial magnetic bearings along with the radial force measurements at high temperatures 1000 F. Zhang, Palazzolo et al. [16] designed and developed the high temperature brushless DC motor to provide the drive torque for spinning the system at the designed conditions.

## 1.4 Contribution

This present thesis work provides a feedback control law that successfully stabilizes the HTPM biased AMB levitated system and summarizes efforts to build a test rig for the HT tests of the machine. The main contribution of the present work is as follows:

- Development of a feedback control law for the mechanical system, to levitate the spinning rotor at high temperatures and high speeds.
- Provide a basic foundation in the form of a fully functional test rig for future research with *permanent magnet biased* and *fault tolerant* magnetic bearings.
- With the use of an analog controller for the current research, this thesis gives an outline of the different components which can be used for achieving feedback.

## 1.5 Novelty

Conventional Magnetic bearing use electromagnets to provide the required flux in order to levitate the shaft along with the temperature operating limitations. The novelty of this research is the use of permanent magnets to provide the bias flux even at high temperatures of around 1000F. The unique feature of these bearings is their fault tolerant capability where in continued stable operation of the bearing is ensured even in case of sudden failure of a coil or a power amplifier (This is achieved using the concept of flux coupling [6]). Simulation of this high temperature permanent magnet biased magnetic bearing system has been done using finite element formulation in Matlab.

## 1.6 Significance

The inherent advantages of the magnetic bearings is widely increasing their application region with some of their current use being in vacuum and clean room techniques, flywheel for energy storage applications, high speed machining applications, medical devices such as blood pumps, beverage industry and turbomachinery. The novel high temperature permanent magnet bearings can be used in applications such as air turbines (where bearings need to operate near heat source), deep subsea pump and compression motors (due to high temperature operating conditions). Also the permanent magnet bias reduces the resources required in terms of current required to carry static loads, further widens their application area.

## 1.7 Features and advantages of magnetic bearings

- Working without any mechanical contact, magnetic bearings have low bearing losses, long life, reduced maintenance, and do not require any type of lubrication. Due to this, they can work in an environment where contamination is a big issue such as vacuum systems.
- There is considerable saving in costs due to absence of lubrication and reduced maintenance.
- Stiffness and damping of an AMB system can be controlled electronically and hence proving useful in applications where these characteristics are critical.
- Very high rotational speeds can be achieved due to no contact and restriction on it only being imposed by the material properties of the rotor. Peripheral speeds of 300 m/s are a standard in state of-the-art AMB applications, a value not reachable by most other bearings [17].
- Vibrations can be actively damped in magnetic bearings by changing important properties of stiffness and damping. Modern digital control systems are available for such purposes.
- Dynamic forces due to unbalance can be cancelled by allowing the rotor to rotate about its axis of inertia.
- Magnetic bearings allow building of test rigs where non conservative bearing forces can be measured accurately apart from other bearing influences. They can be used to generate forces which can be imposed in a test setup to identify rotor dynamics and also help identify unknown parameters such as damping, unbalances or process forces in a conventional oil film bearing.

- Due to their built-in instrumentation, magnetic bearings can be used for monitoring the health of the system and preventing hazards.

# 2. FEEDBACK CONTROL

## 2.1 Theory

A Magnetic Bearing is open loop unstable i.e. the rotor is attracted to one side due to the negative stiffness of the bearing and attached in position. A well designed feedback control mechanism has to overcome this and put in some effort at the start to provide a stable levitation. A very strong simplification of a practical magnetic bearing i.e. a one degree of freedom system is shown in the Figure 2-1.

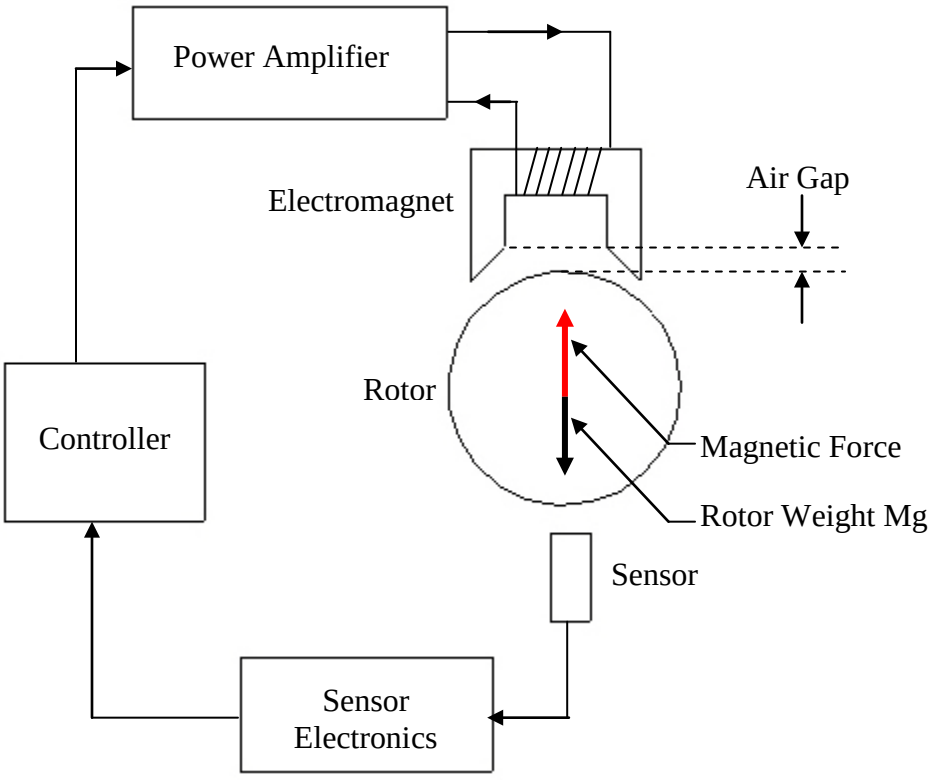


Figure 2-1 Basic closed loop magnetic bearing model

This model is a very basic tool to develop the mathematics of the magnetic bearing system and in practice a very complex arrangement of a number of electromagnets is used to support the flexible rotor. The combination of the power amplifier and the electromagnets (also called electromagnetic actuator) provides the required magnetic forces to stably levitate the rotor in its desired position. The controller provides the signal to the actuators (to increase or decrease the current in the coils). A very important task of this controller is to levitate the rotor in its desired position and stabilize the complete closed loop system over a wide range of frequencies by regulating an appropriate current value in the bearing electromagnets. The position sensors provide information on the position of the rotor in the magnetic field and convey the deviation of the rotor from the desired position in the form of an output voltage. Important magnetic bearing properties depend on the power amplifier & electromagnet design i.e. amplifier voltage & current, bearing geometry and number of turns & inductance of the coil.

### 2.1.1 *Mathematical model of a simple magnetic bearing control system*

A magnetic bearing system can be thought of as a mechanical spring damper system to develop the basic mathematics without sensor, amplifier or other complex dynamics. Due to its inherent negative stiffness, the magnetic force due to a magnetic bearing can be written as:

$$f(x,i) = -k_s x + k_i i \tag{2.1}$$

In the Equation (2.1), $k_s$ is the position stiffness and $k_i$ is the current stiffness in the linearized range. Similarly for a conventional mechanical spring – damper system, we have:

$$f = -kx - c\dot{x} \tag{2.2}$$

Equivalence between the two forces can be thought of as the magnetic bearing force must account for stable levitation of the rotor in its equilibrium point. Hence the magnetic bearing has to provide a restoring force in case of deviation of the rotor position from the equilibrium point and attenuate the oscillations around the operating point. After equating Equations (2.1) and (2.2), the important task of the controller (stable levitation) boils down to find out an appropriate value of control current i which will provide stable levitation of the rotor in its equilibrium point.

$$i = -\frac{(k - k_s)x + c\dot{x}}{k_i} \tag{2.3}$$

A very important interest in any controlled system is to achieve acceptable closed loop behavior which can be assessed by observing the closed loop eigenvalues of the complete system. Using Newton's law, the desired control force is expressed as:

$$m\ddot{x} = -kx - c\dot{x} \tag{2.4}$$

The well-known second order differential equation of a spring mass system is thus obtained.

$$m\ddot{x} + c\dot{x} + kx = 0 \tag{2.5}$$

Assuming a solution of the form $x = e^{\lambda t}$ and inserting it in Equation (2.5), we get:

$$(m\lambda^2 + c\lambda + k) \cdot e^{\lambda t} = 0 \tag{2.6}$$

Since $e^{\lambda t} \neq 0$, we get a characteristic polynomial whose roots (eigenvalues) are complex conjugate pairs.

$$m\lambda^2 + c\lambda + k = 0 \tag{2.7}$$

The roots for Equation (2.7) can be given by,

$$\lambda_{1,2} = \frac{-c \pm \sqrt{c^2 - 4mk}}{2m} = \frac{-c}{2m} \pm \sqrt{\frac{c^2}{4m^2} - \frac{k}{m}} \tag{2.8}$$

Since $\frac{c^2}{4m^2} < \frac{k}{m}$, we have

$$\lambda_{1,2} = \frac{-c}{2m} \pm i \cdot \sqrt{\frac{k}{m} - \frac{c^2}{4m^2}} \tag{2.9}$$

Let $\sigma = \frac{c}{2m}$ and $\omega = \sqrt{\frac{k}{m} - \frac{c^2}{4m^2}}$

Therefore,

$$\lambda_{1,2} = -\sigma \pm i \cdot \omega \tag{2.10}$$

The complex plane plot of these closed loop eigenvalues is shown in Figure 2-2. From Equation (2.9), it can be seen that stiffness $k$ primarily affects the imaginary part of the eigenvalues with an increase in its value, increasing the frequency component $\omega$. The damping $c$ on the other hand, influences both the real and imaginary part in that an

increase in its value causes an increase in the negative real part (i.e. pushing the eigenvalues farther to the left side and increasing stability) while reducing the frequency component. However, very large values of damping yield real eigenvalues which lead to a stable system but its performance is not satisfactory in this case since one eigenvalue approaches zero (case of overcritical damping). A detailed analysis of the stiffness and damping guides in selecting appropriate proportional and differential gains of the controller for a stable closed loop system will be described in the next section. Figure 2-3 shows the open loop eigenvalues.

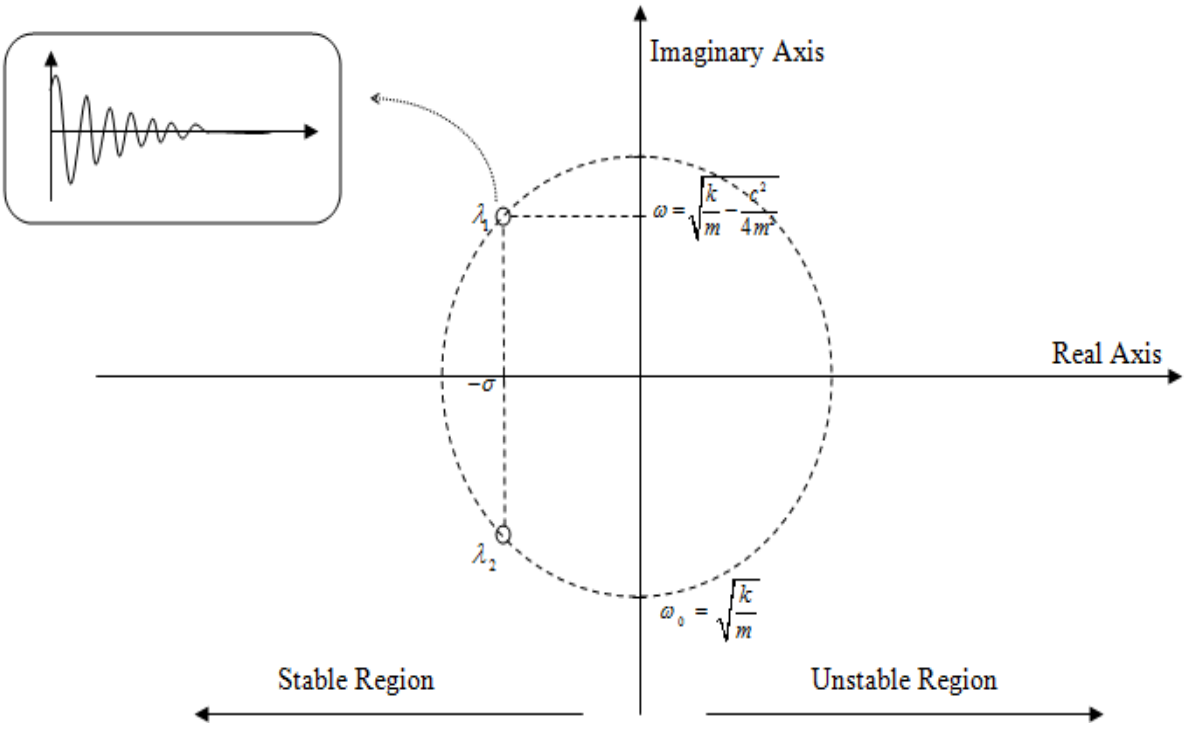


Figure 2-2 Eigenvalues of a closed loop stable system

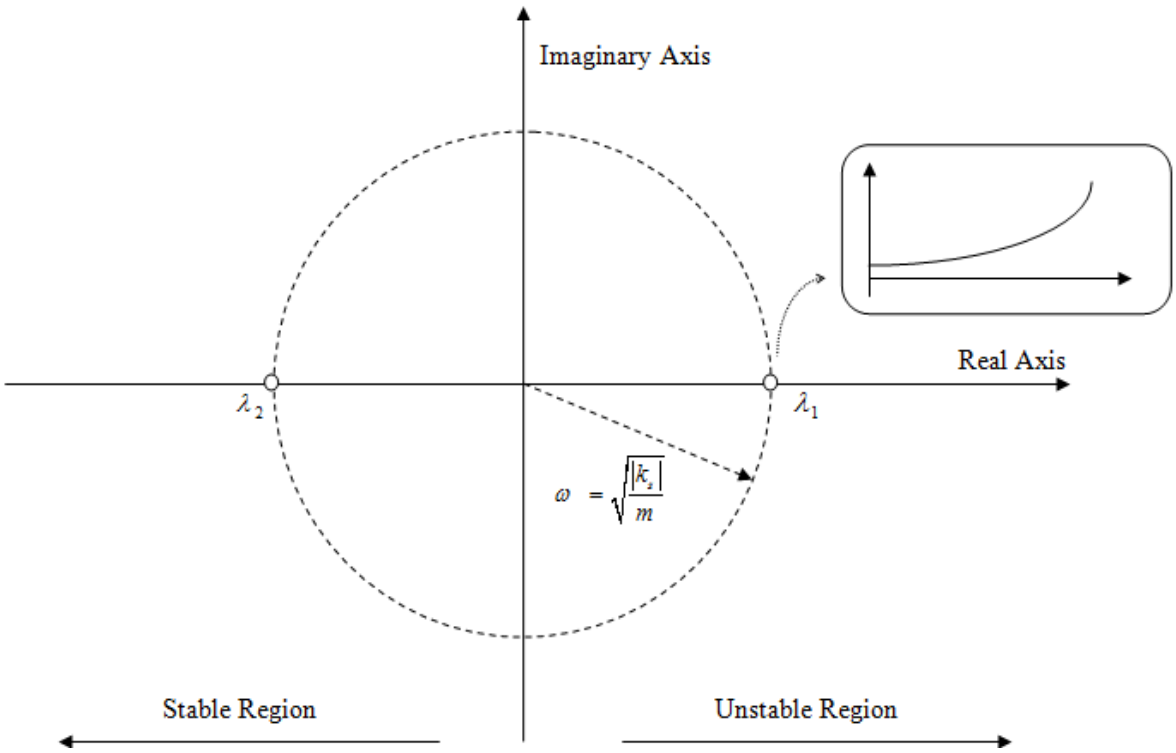


Figure 2-3 Eigenvalues of an open loop unstable system

### 2.1.2 *Selection of stiffness and damping - PD control law*

From Equation (2.3), we can write:

$$i = -\frac{(k - k_s)}{k_i} x - \frac{c}{k_i} \dot{x} \tag{2.11}$$

This controller current given by Equation (2.11) can be divided into two parts; a proportional feedback with control parameter P and a differential feedback with control parameter D. Each of these parameters can be written as shown below:

$$P = \frac{k - k_s}{k_i}, \; D = \frac{c}{k_i}$$

These are well known with the name proportional and derivative gains in a Proportional – Derivative (PD) control law. Appropriate values of these gain parameters are chosen for a particular closed loop system keeping the required stiffness and damping in mind. Since stiffness and damping are the most essential properties of any bearing, they are preselected for each application and affect the size of the bearing along with the power amplifier rating in case of magnetic bearings.

Very low stiffness values may be difficult to realize since the closed loop eigenvalues are located close to the origin requiring an exact knowledge of the inherent bearing negative stiffness and a small change may lead to instability. Similarly, large values of stiffness pose high eigenfrequencies which require appropriate high bandwidth of controller to handle the dynamics of the system. Selection of damping is proportional to the amount of stiffness to achieve satisfactory performance of the system. An extensive analysis on the selection of stiffness and damping can be found in [17]. Figure 2-4 shows the effect of control parameters on the closed loop eigenvalues.

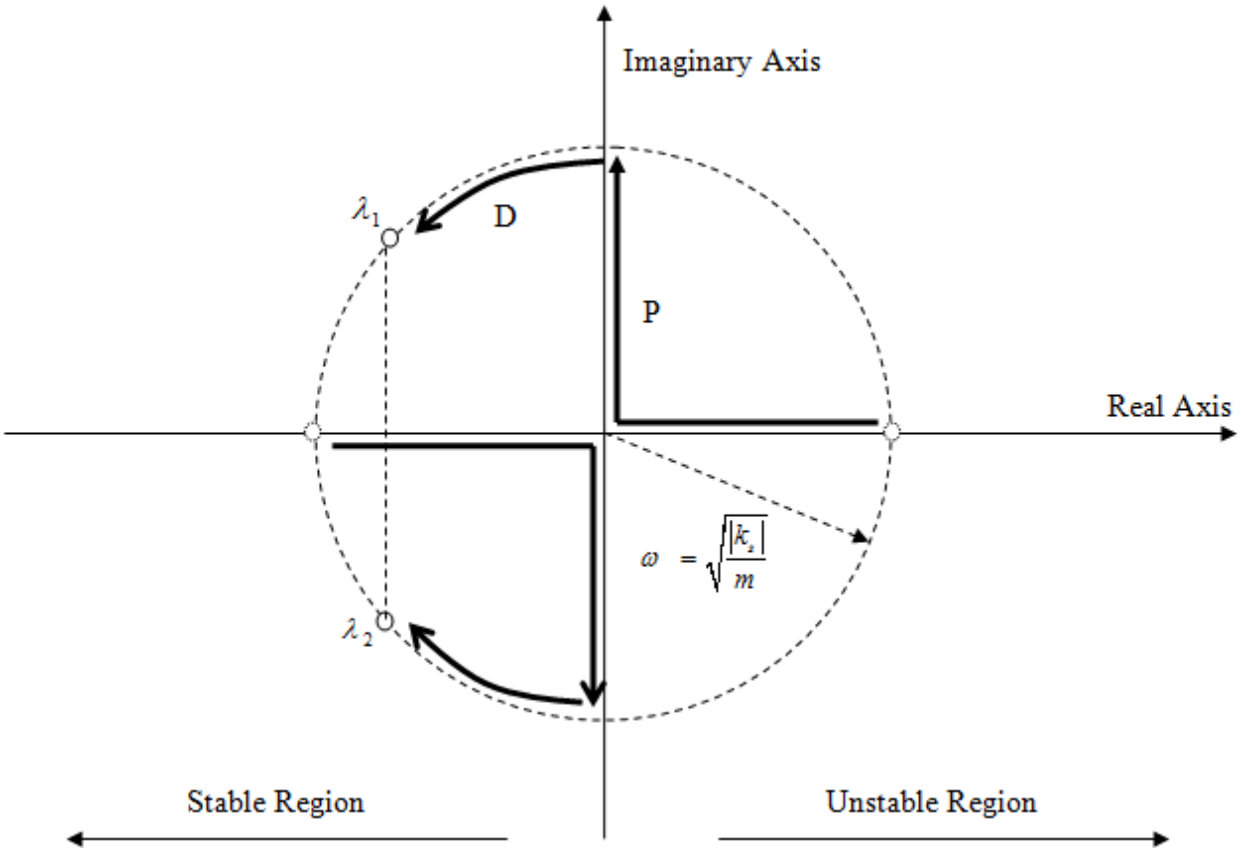


Figure 2-4 Effect of control parameters P & D on the closed loop eigenvalues [17]

An integrating part is also sometimes incorporated in addition to the proportional and derivative gains to overcome the deficiency of a pure Proportional – Derivative (PD) control which results in a change of the steady position with a change in external load. To overcome these, an exact knowledge of the negative bearing stiffness and external force magnitude is required which is accomplished using an integrator. However, a very high value of integral gain must not be chosen since it introduces a phase lag in the frequency response of the controller. A schematic diagram of a PD control scheme for a complete mechanical plant is shown in Figure 2-5.

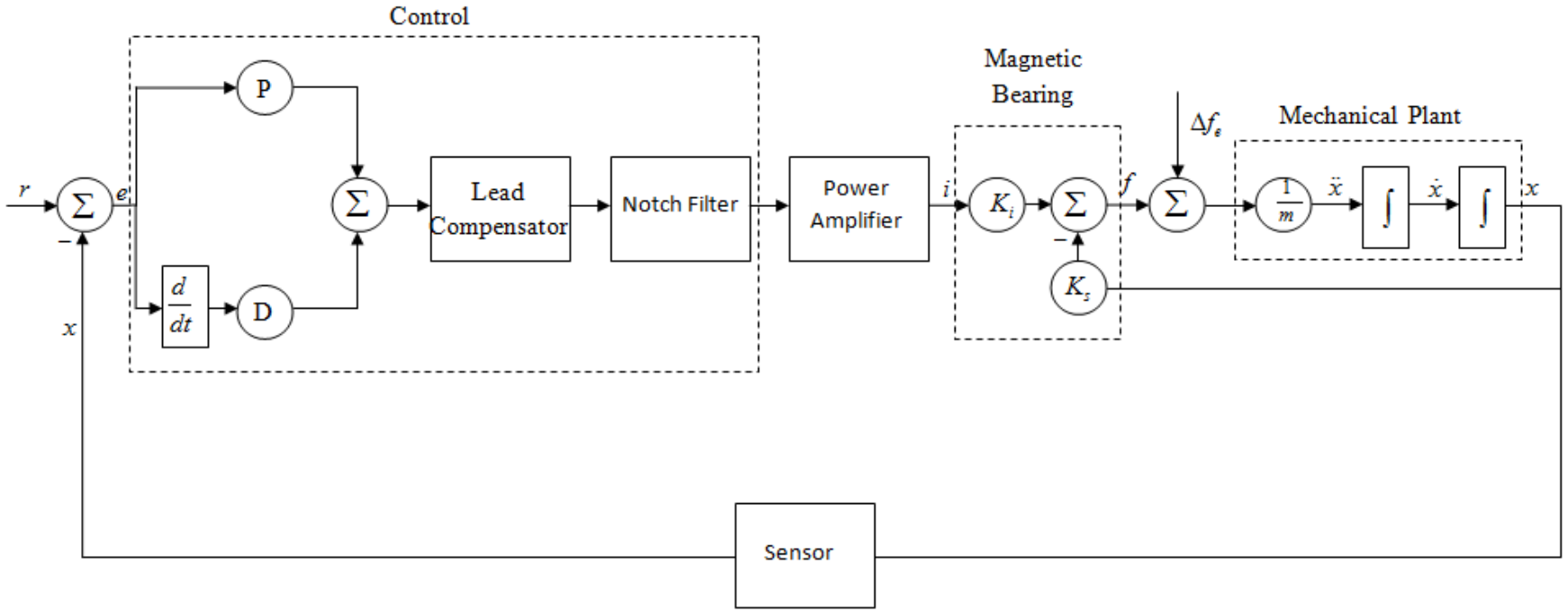


Figure 2-5 Control architecture of the magnetic bearing system

## 2.2 Feedback control system model

Figure 2-7 shows the basic model diagram of the feedback controller which is used for universal magnetic bearing system to be run at designed conditions of 1000F temperature and 20,000 rpm speed.

A short description on the essential individual elements of the closed loop system is described in the following lines.

Rotor: The rotor shaft, made of Inconel 718 (non-magnetic) for the two radial bearings and Hiperco 27 (magnetic) for the axial bearing is assembled from its individual parts (Figure 2-6), will provide the high temperature Kaman sensors with its position feedback in the X & Y direction at the two radial locations (Figure 4-19) while the axial sensor at the bottom will provide the position feedback of the rotor in the Z direction. All sensors are calibrated for linearity in a given range which gives the distance between the shaft and the sensor from the output voltage reading of the sensors.

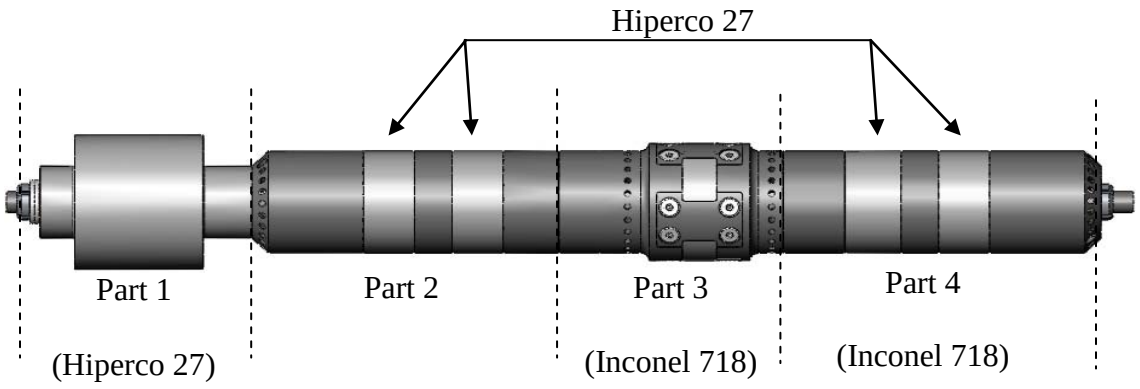


Figure 2-6 Rotor shaft assembled together from individual parts

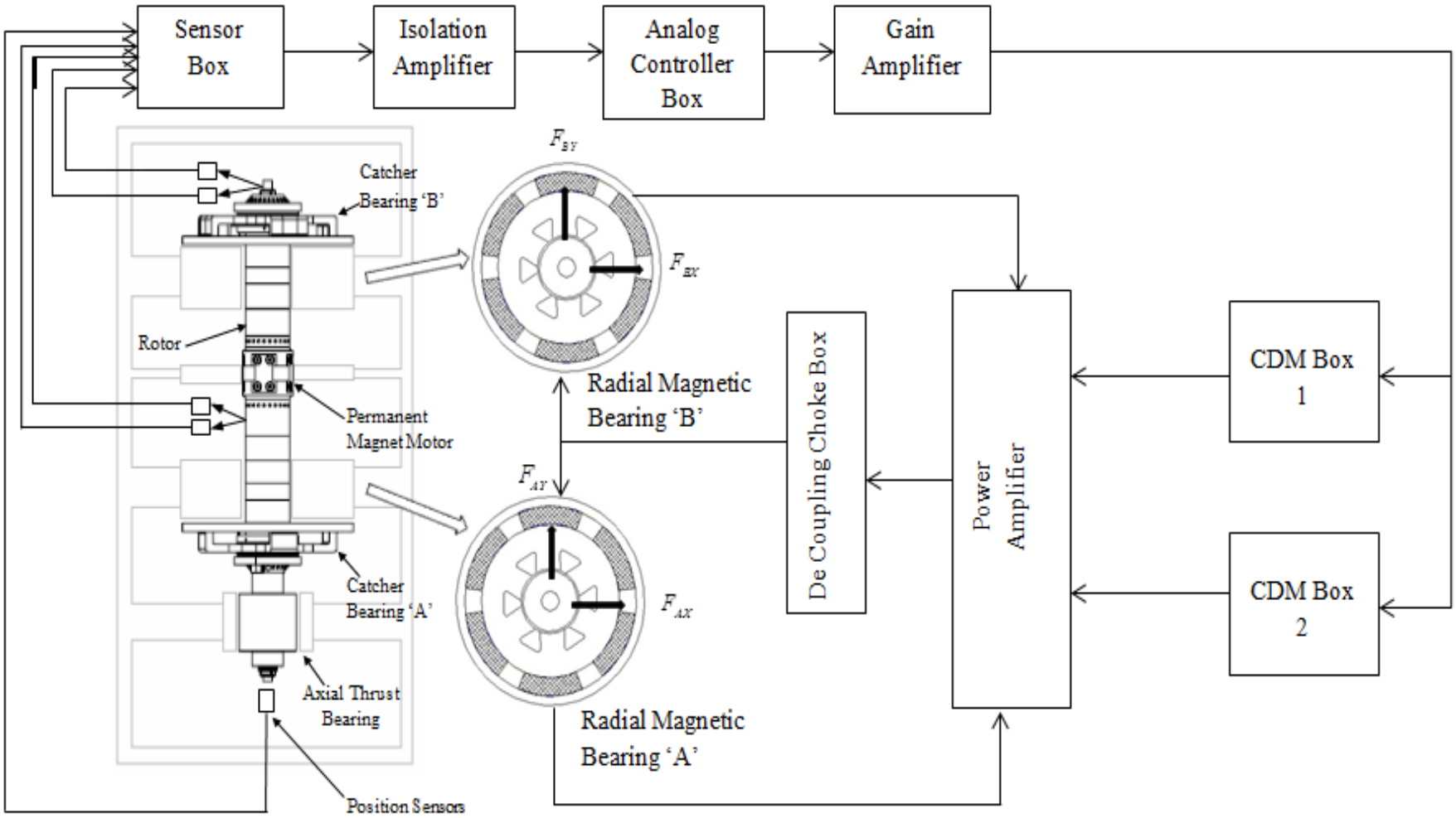


Figure 2-7 Magnetic bearing control system model

Controller: The controller used is a decentralized PD analog controller which takes in input from all the 5 sensors (2 sensors at top radial location for X&Y, 2 sensors at bottom radial location for X&Y, 1 axial sensor at the bottom) and sends an output voltage corresponding to the shaft position at each location as shown in Figure 2-8.

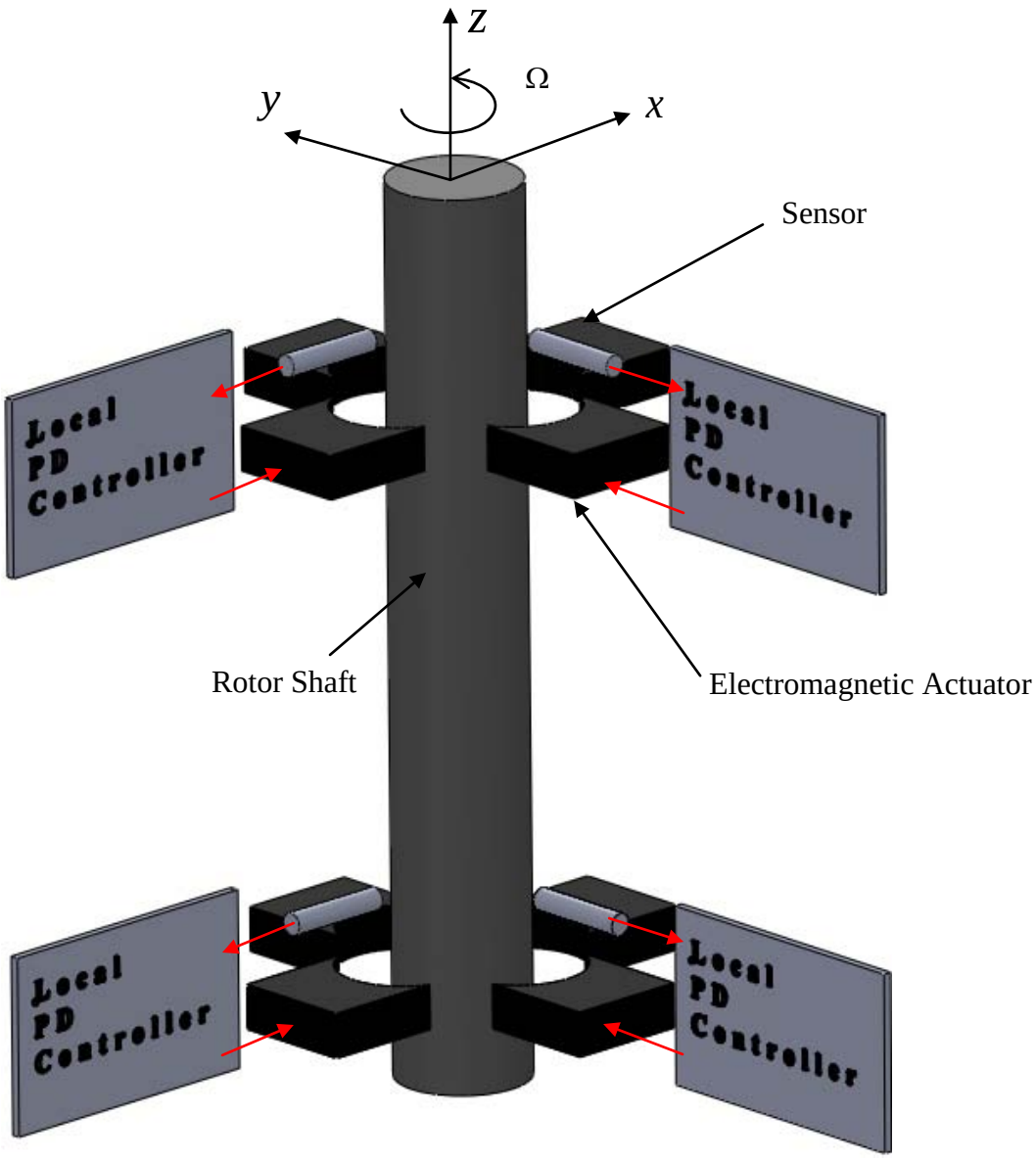


Figure 2-8 Decentralized control structure with PD control [17]

CDM: The current distribution matrix box (CDM) takes in input from the controller for the 5 primary sensing axis and outputs six voltages to the power amplifiers to be distributed in each radial bearing (for the six coils in it) and one output voltage for the axial thrust bearing.

Power Amplifiers (Servoamplifier): The output voltages from the current distribution matrix boxes are too low to be used directly for powering the coils and hence power amplifiers are used which step up the voltage value to an extent that the output current follows the original input voltage in phase from the CDM but at an amplified value.

Decoupling Choke Box: The flowing current causes mutual and self-inductances within the bearing coils due to Faraday's Law. The inductance matrix of an isolated radial bearing is singular because flux conservation introduces a dependency relation between the fluxes. This produces a potentially unstable operation state for the power amplifiers. By using a decoupling choke box and adjusting its parameter values (namely air gap, cross sectional area of the core and number of turns), the inductance matrix becomes full rank and the mutual inductances become zero. Hence a single decoupling core is added to the radial bearing to eliminate inductance effects and ensure circuit stability. The decoupling choke box is only used for the two radial bearings due to the very close proximity of the 6 poles in the magnetic bearing. Figure 2-9(b) shows the construction of the decoupling choke box. Each C core is connected to 3 poles of a magnetic bearing i.e. the 3 windings on a single C core are connected to 1, 2 & 3 numbered pole pairs (see Figure 3-39 Wiring scheme employed to make the interconnections and external wire for details).

(a) 3 windings on each laminated C core

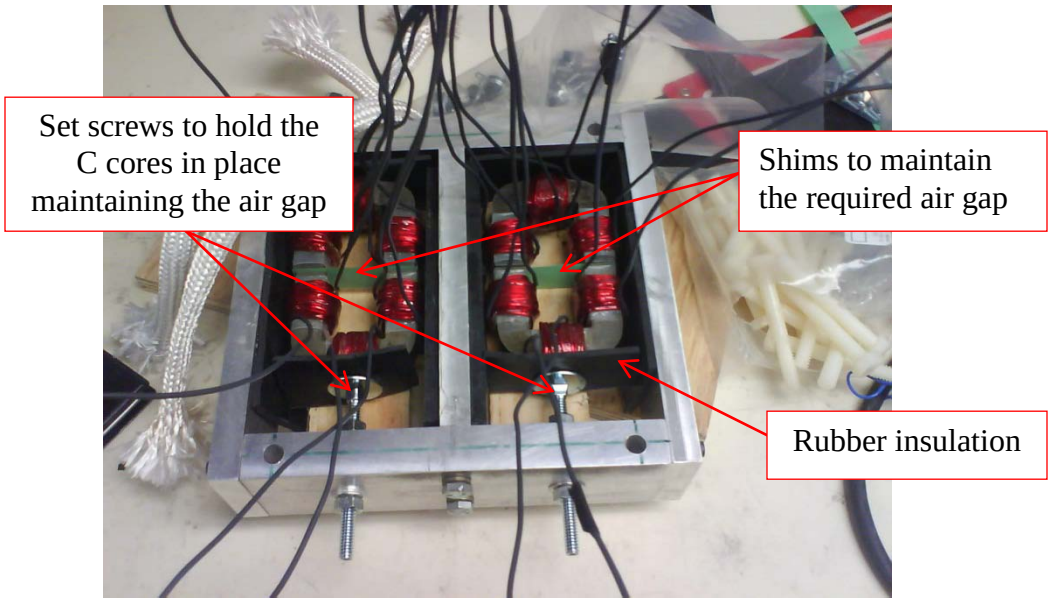


(b) Construction of the decoupling choke box

Figure 2-9 Decoupling choke box

Radial Magnetic Bearing: The final output from the decoupling choke box goes into the six coils of the radial bearing electromagnetic actuator which provide the required levitating effect at the two locations.

# 3. ELECTRICAL SYSTEM

The power electronics form an integral part of the complete universal magnetic bearing system. The model of the complete controller system is shown in Figure 2-7. All the components, which are used, had to be calibrated and tested before using it on the EEC universal magnetic bearing system. The following sections summarize the testing and calibration of the different components.

## 3.1 Sensor

The KD1925 high temperature Kaman sensors are used for sensing the shaft position in the five directions of interest (described in detail in 4.6.3). Five sets of sensor – sensor cable – sensor box drive slot had to be chosen for the 5 directions of interest and such choice was made keeping the noise output from the sensors to be a minimum. This was done since otherwise the controller would give an output voltage to this noise signal of the sensor and cause undesirable oscillatory movement of the shaft. The radial clearance in the magnetic bearings is 17 mils while in the catcher bearings it is 8 mils. Hence different permutations of the available choices (8 sensors, cables and slots) were made to the keep the sensor noise to a minimum (below 1 mil). Table 3-1 lists the five sets which are used. Assuming the sensors to have a resolution of 50 mV/mil [6], all the following sets were observed to have a noise level less than 1 mil.

Table 3-1 Set of sensor-cable-sensor box drive slot used for each corresponding axis

| Bearing | Sensing Direction | Sensor # | Cable # | Drive Slot # |
|---|---|---|---|---|
| Top Radial Bearing | X Direction | S0121249-01-06 | S0121249-01-07 | 3 |
| | Y Direction | S0121249-01-02 | S0121249-01-02 | 7 |
| Bottom Radial Bearing | X Direction | S0121249-04-01 | S0121249-01-04 | 2 |
| | Y Direction | S0121249-01-01 | S0121249-01-03 | 5 |
| Axial Thrust Bearing | Z Direction | S0121249-01-07 | S0121249-01-08 | 4 |

## 3.2 Sensor box

The high temperature Kaman sensors provide position feedback to this sensor box and this in turn provides an appropriate voltage output. The sensors, which are used, are calibrated using this sensor box to provide appropriate readings. Figure 3-1 shows the test setup for calibration and the steps outlined in the user manual were followed for tuning.

Primarily the Zero, Gain and Linearity (Coarse and Fine) parameters on the sensor box were adjusted to have the sensors output an appropriate voltage in the linear range. The sensors saturated at 55 mils distance from the target. A curve fitting of the calibration data (shown in Figure 3-2 , Figure 3-3, Figure 3-4, Figure 3-5 & Figure 3-6) is done to obtain an empirical relation which would the give the distance in mils for the corresponding voltage reading of the respective calibrated sensor. This is done to obtain the exact shaft position within the magnetic bearing clearance space which could be used to correlate with the results obtained from the simulation of the complete system.

On the assembled static system, all the sensors are set at the center of their linear range (approx. 30 mils) since the shaft is magnetically attached to one side and the exact magnetic field center is unknown.

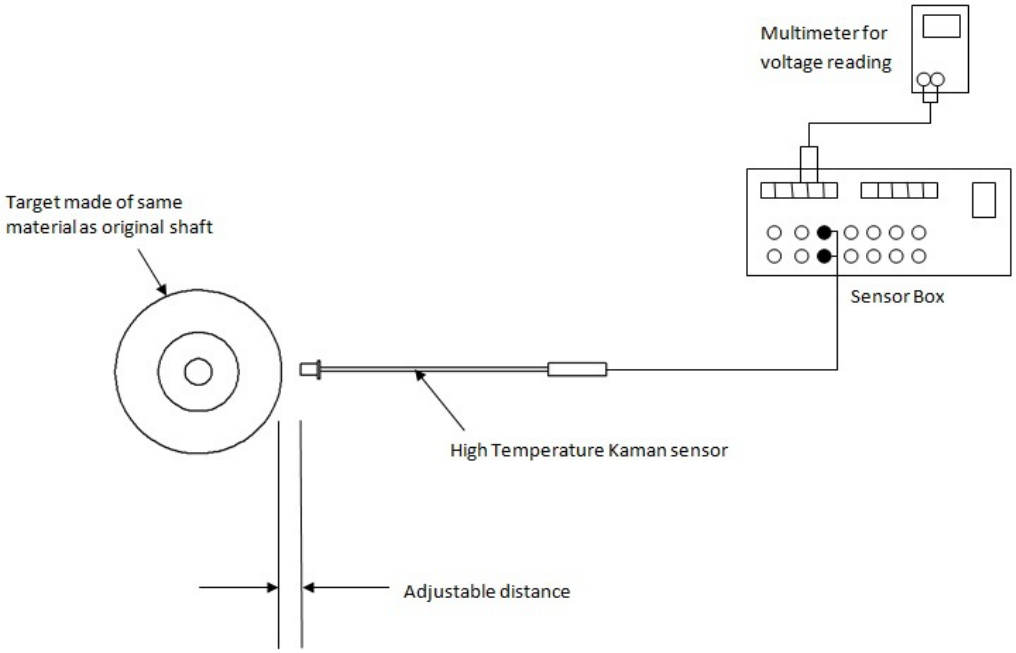


Figure 3-1 Experimental setup to calibrate all the 5 sensors

| Set 1 | |
|---|---|
| Sensor S0121249-01-06 | Cable S0121249-01-07 |
| Drive Slot # 3 | |

| Mil | Voltage |
|---|---|
| 0 | 0.00223 |
| 9.5 | 0.416 |
| 15 | 0.729 |
| 18.5 | 0.845 |
| 26 | 1.211 |
| 29.5 | 1.412 |
| 38.5 | 1.972 |
| 51 | 2.537 |

| y = 0.0506x - 0.0483 |
|---|
| R2 = 0.997 |

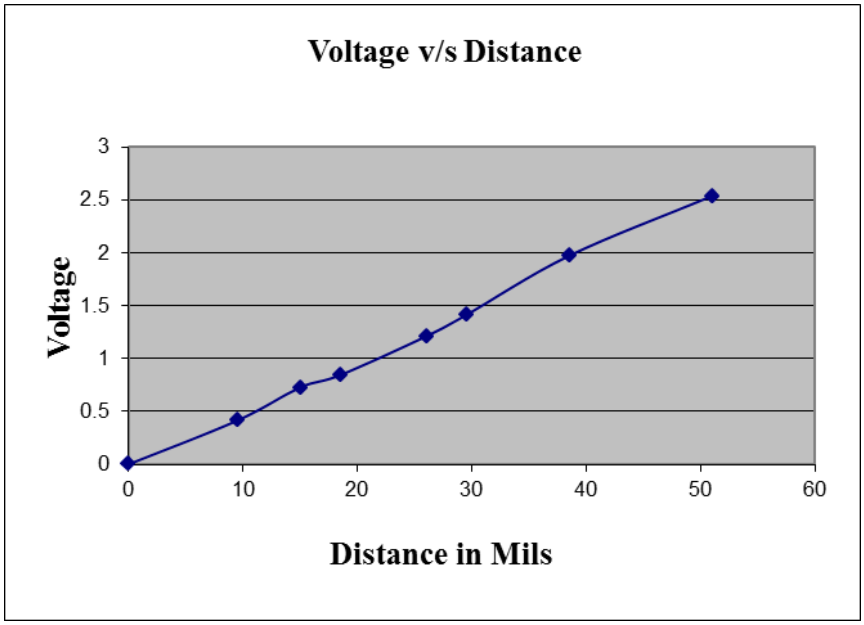


Figure 3-2 Calibration data for top radial bearing X direction sensor

| Set 2 | |
|---|---|
| Sensor S0121249-01-02 | Cable S0121249-01-02 |
| Drive Slot # 7 | |

| Mil | Voltage |
|---|---|
| 0 | 0.015 |
| 9.5 | 0.47 |
| 15 | 0.745 |
| 18.5 | 1.036 |
| 26 | 1.276 |
| 29.5 | 1.408 |
| 38.5 | 1.803 |
| 51 | 2.533 |

| y = 0.0481x + 0.0304 |
|---|
| R2 = 0.9944 |

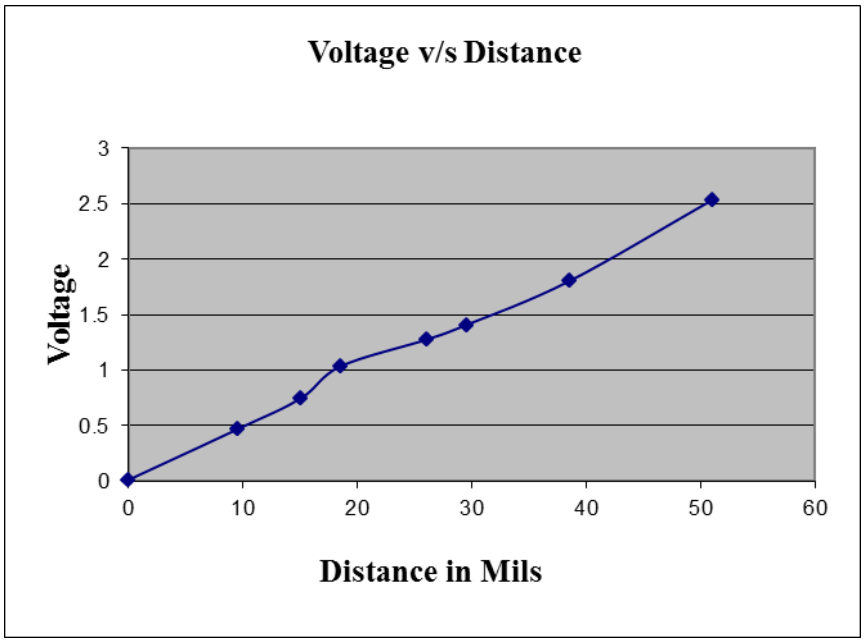


Figure 3-3 Calibration data for top radial bearing Y direction sensor

| Set 3 | |
|---|---|
| Sensor S0121249-04-01 | Cable 21249-01-04 |
| Drive Slot # 2 | |

| Mil | Voltage |
|---|---|
| 0 | 0.004 |
| 9.5 | 0.493 |
| 15 | 0.747 |
| 18.5 | 1.045 |
| 26 | 1.318 |
| 29.5 | 1.572 |
| 38.5 | 2.012 |
| 51 | 2.641 |

| y = 0.0519x + 0.0098 |
|---|
| R2 = 0.9979 |

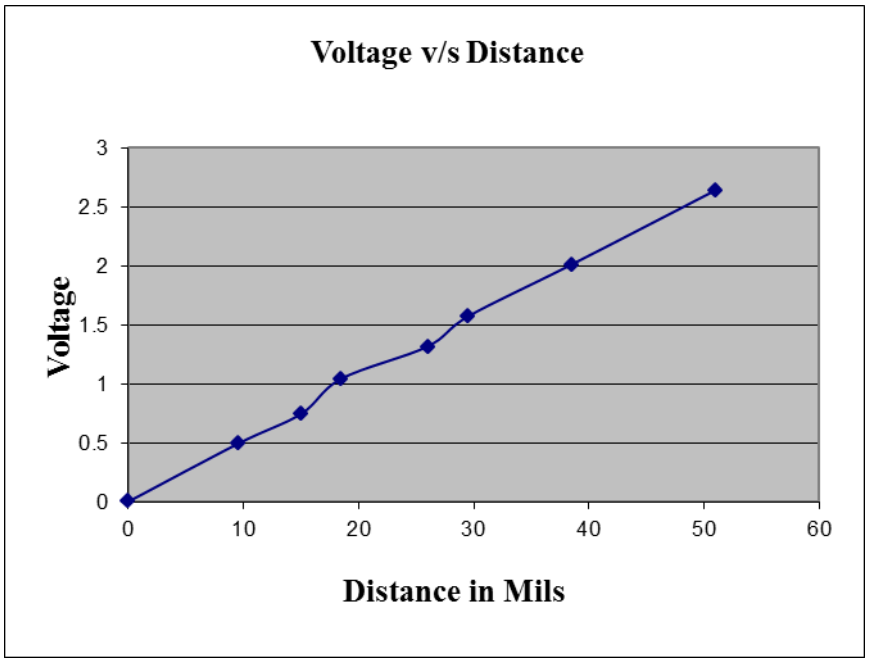


Figure 3-4 Calibration data for bottom radial bearing X direction sensor

| Set 4 | |
|---|---|
| Sensor S0121249-01-01 | Cable S0121249-01-03 |
| Drive Slot # 5 | |

| Mil | Voltage |
|---|---|
| 0 | -0.0034 |
| 9.5 | 0.445 |
| 15 | 0.763 |
| 18.5 | 0.9 |
| 26 | 1.253 |
| 29.5 | 1.464 |
| 38.5 | 1.823 |
| 51 | 2.573 |

| y = 0.0497x - 0.0157 |
|---|
| R2 = 0.9977 |

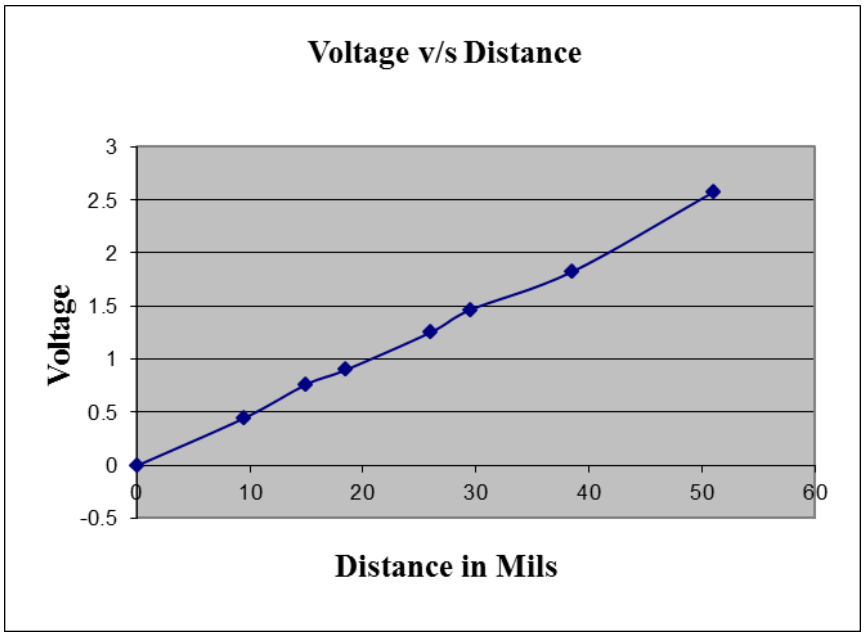


Figure 3-5 Calibration data for bottom radial bearing Y direction sensor

| Set 5 | |
|---|---|
| Sensor S0121249-01-07 | Cable S0121249-01-08 |
| Drive Slot # 4 | |

| Mil | Voltage |
|---|---|
| 0 | -0.02 |
| 9.5 | 0.483 |
| 15 | 0.744 |
| 18.5 | 1.026 |
| 26 | 1.175 |
| 29.5 | 1.453 |
| 38.5 | 1.943 |
| 51 | 2.593 |

| y = 0.0505x - 0.0118 |
|---|
| R2 = 0.994 |

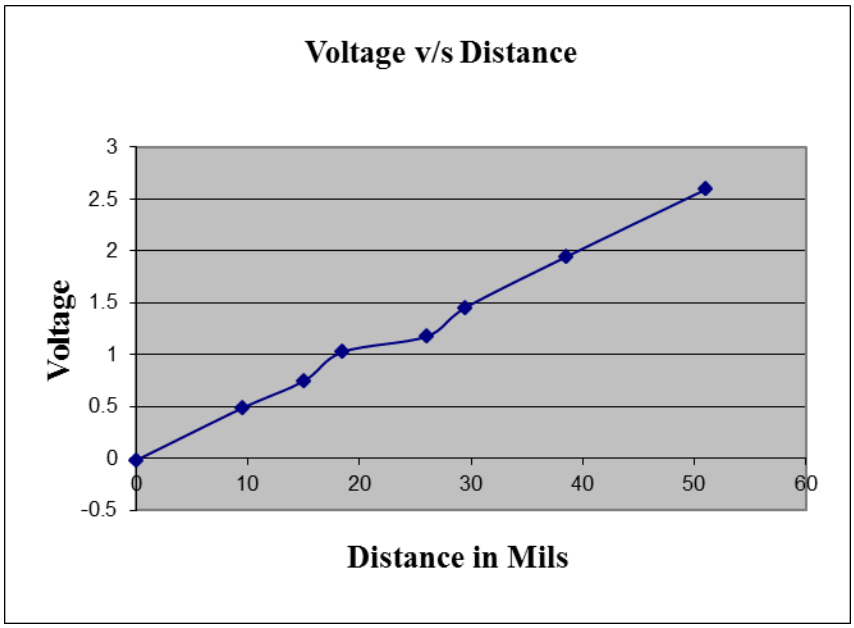


Figure 3-6 Calibration data for axial thrust bearing Z direction sensor

### 3.3 Isolation amplifier

Isolation amplifiers are a source of electrical safety and provide electrical isolation to the instruments they are connected to. Instruments connected to common mode voltages allow the ground currents to circulate, without an isolation barrier, leading to a noisy representation of the signal being measured. Given the criticality of the output measurement from the sensors which would be given as input to the controller to provide appropriate feedback action, an isolation amplifier is used in between the path from the output of the sensor box to the controller input. They also eliminate the measurement errors caused by grounding loops. In addition, if the common mode voltage and/or current is sufficient, isolation amplifiers also help protect against the possibility of any instrument malfunctioning due to the potentially destructive voltages.

Figure 3-7 shows the test procedure for testing the isolation amplifier for the EEC universal system. The gain on the amplifier was observed to be unity for each channel as shown in Table 3-2.

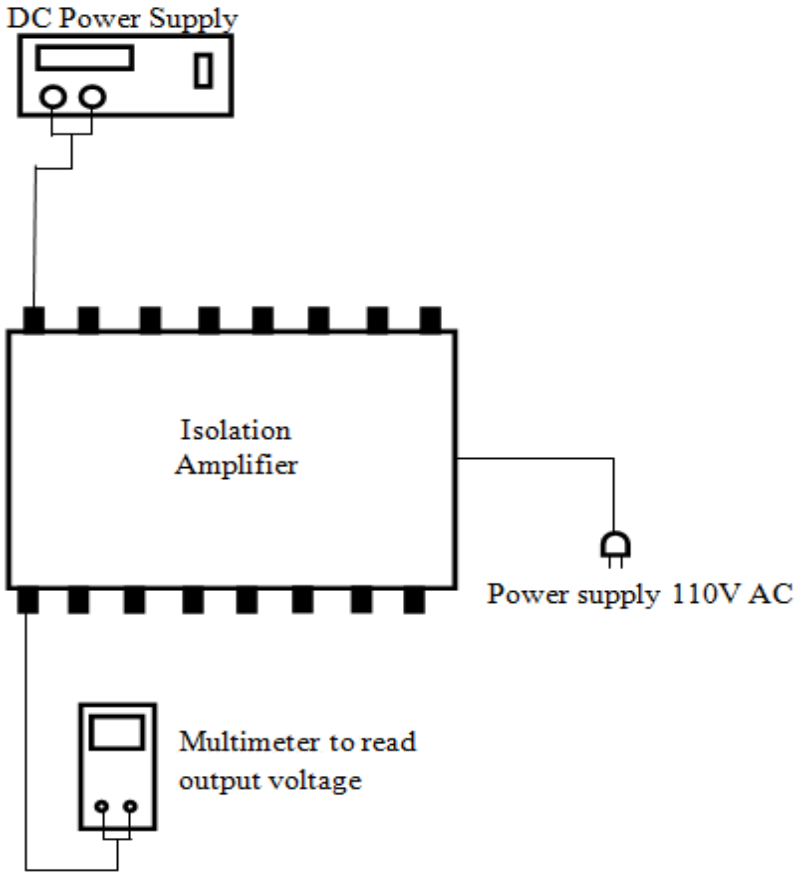


Figure 3-7 Experimental setup to test the isolation amplifier

Table 3-2 Test data results

| Channel | DC input<br>mv | Amplifier output<br>mv | Gain = Output/Input |
|---|---|---|---|
| 1 | 106 | 103.7 | ≈1 |
| 2 | 105.1 | 98 | ≈1 |
| 3 | 104.4 | 104.6 | ≈1 |
| 4 | 103.9 | 90.3 | ≈1 |
| 5 | 103.4 | 88.8 | ≈1 |
| 6 | 103 | 95.1 | ≈1 |
| 7 | 102.5 | 102.1 | ≈1 |
| 8 | 102.2 | 93.4 | ≈1 |

### 3.4 Local PD controller

A decentralized PD controller is used for the EEC universal system. This controller design has a local SISO PD control law for each axis of control as shown in Figure 2-8. The complete circuit implemented on the breadboard for one axis is shown in Figure 3-8.

This controller was previously used for a PLM flywheel system and since its robustness was demonstrated with its successful operation, it is used for the EEC universal system by changing the gain parameters and notch frequency locations. An experimental procedure was conducted to obtain the transfer function for each axis channel using LabVIEW and test its adaptivity for the magnetic bearing system.

Figure 3-9 shows the experimental procedure to obtain the transfer function and the results obtained. The function generator had to be swept across to and fro in the frequency range of interest for each channel in order to have a good coherence in the data recorded by the LabVIEW system. Figure 3-10, Figure 3-11, Figure 3-12, Figure 3-13 & Figure 3-14 show the transfer function measured using this experimental setup.

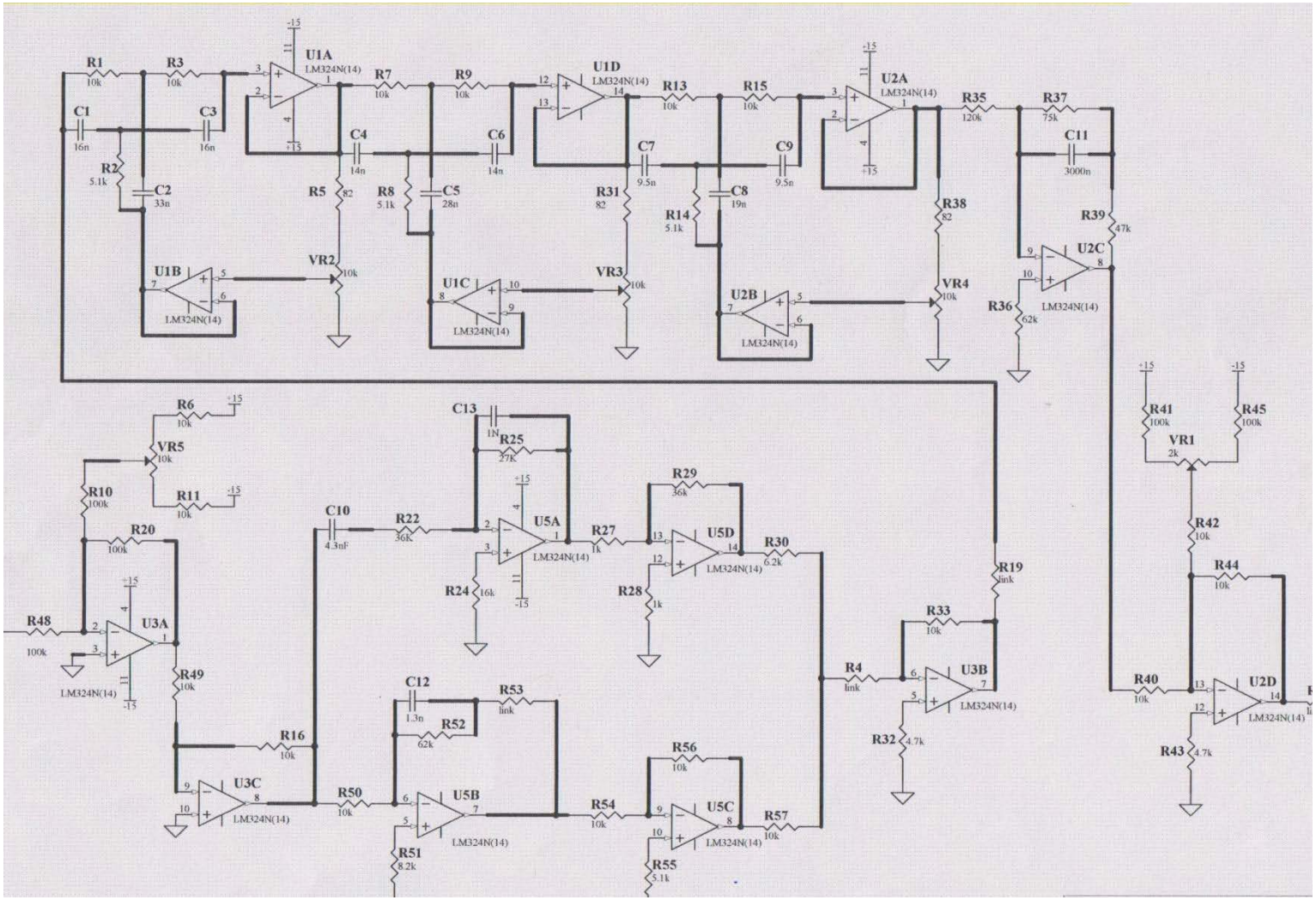


Figure 3-8 Circuit diagram illustration of the PD controller for a single axis

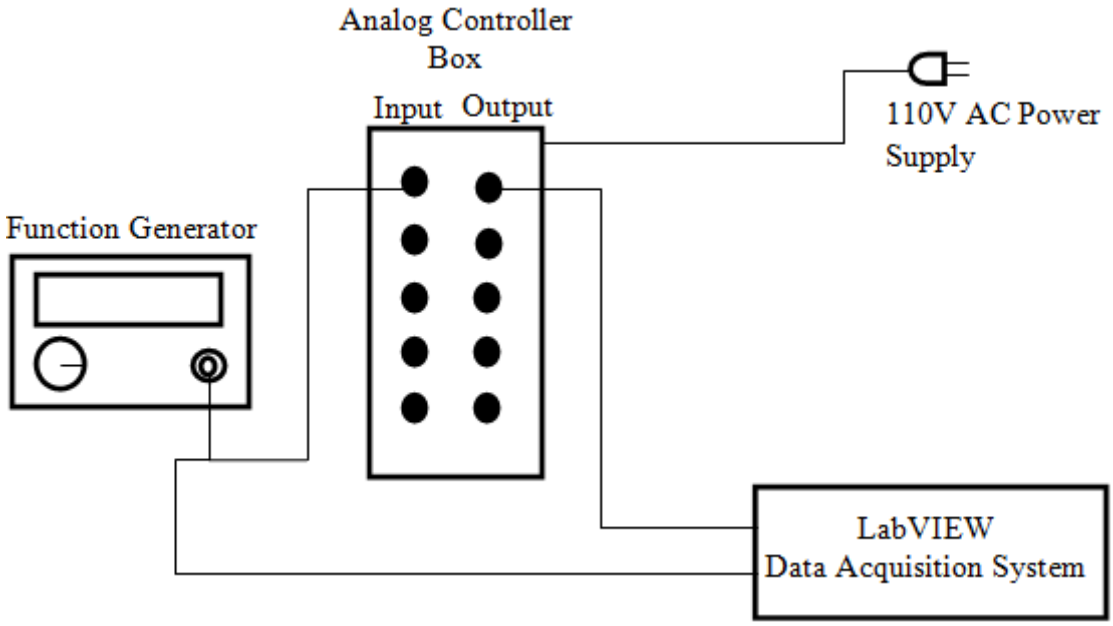


Figure 3-9 Experimental test procedure to obtain transfer function for each channel

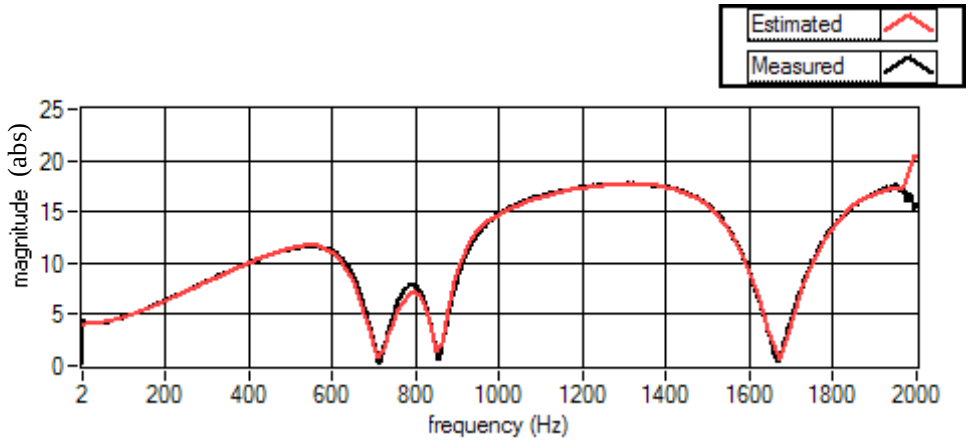


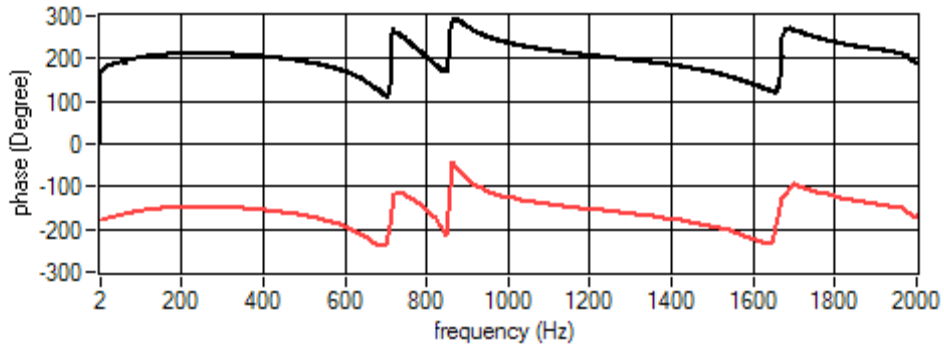


Transfer Function

| | | | | | | | |
|---|---|---|---|---|---|---|---|
| | numerator | | | | | | |
| 0 | -33.8739 | -0.0337169 | -3.47573E-6 | -3.3698E-9 | -1.09022E-13 | -1.04233E-16 | -1.11649E-21 |
| | denominator | | | | | | |
| 0 | 8.46925 | 0.00238607 | 1.08918E-6 | 2.18366E-10 | 4.22528E-14 | 6.17309E-18 | 5.86837E-22 |

Transfer Function

| | | | | | | | |
|---|---|---|---|---|---|---|---|
| | numerator | | | | | | |
| 7 | -1.06505E-24 | -3.48251E-30 | -3.36975E-33 | 0 | 0 | 0 | 0 |
| | denominator | | | | | | |
| 7 | 5.94278E-26 | 3.10688E-30 | 1.80579E-34 | 5.214E-39 | 0 | 0 | 0 |

Figure 3-10 Estimated transfer function obtained for top radial bearing X sensing direction channel

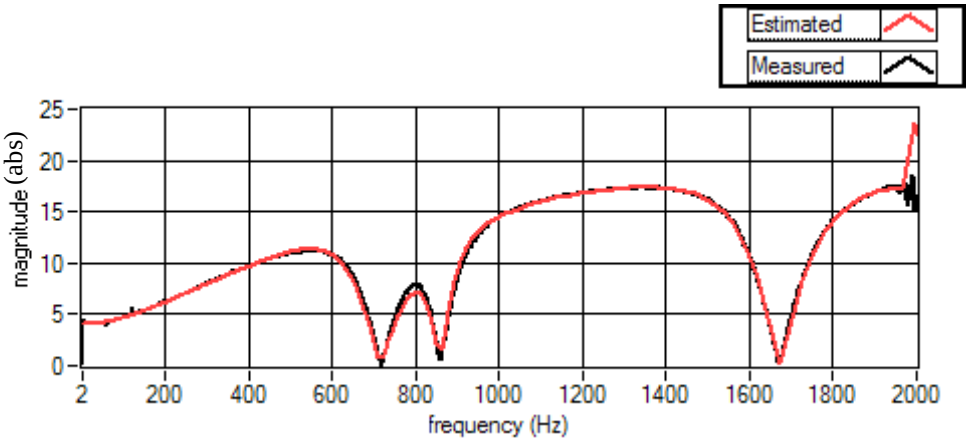


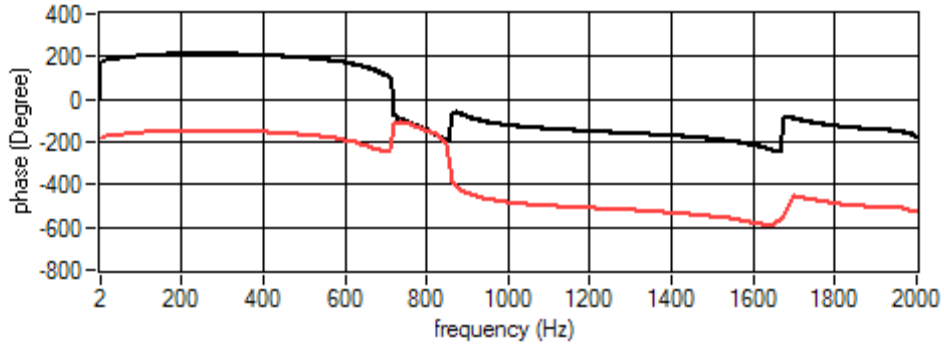


Transfer Function

| | | | | | | | |
|---|---|---|---|---|---|---|---|
| numerator | | | | | | | |
| 0 | -35.5359 | -0.0343219 | -3.55399E-6 | -3.40434E-9 | -1.09251E-13 | -1.04644E-16 | -1.10397E-21 |
| denominator | | | | | | | |
| 0 | 8.87405 | 0.00248935 | 1.12055E-6 | 2.25761E-10 | 4.27556E-14 | 6.36084E-18 | 5.85701E-22 |

Transfer Function

| | | | | | | | |
|---|---|---|---|---|---|---|---|
| numerator | | | | | | | |
| 7 | -1.06521E-24 | -3.42739E-30 | -3.36234E-33 | 0 | 0 | 0 | 0 |
| denominator | | | | | | | |
| 7 | 6.13432E-26 | 3.08778E-30 | 1.86899E-34 | 5.214E-39 | 0 | 0 | 0 |

Figure 3-11 Estimated transfer function obtained for top radial bearing Y sensing direction channel

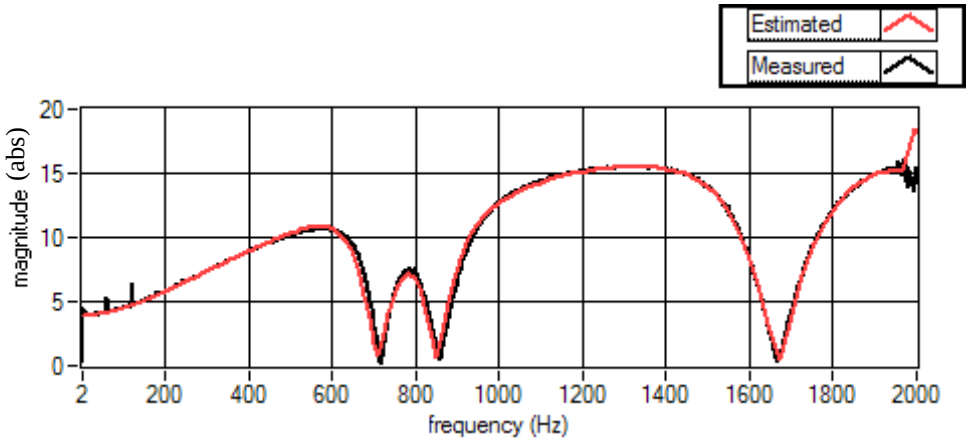


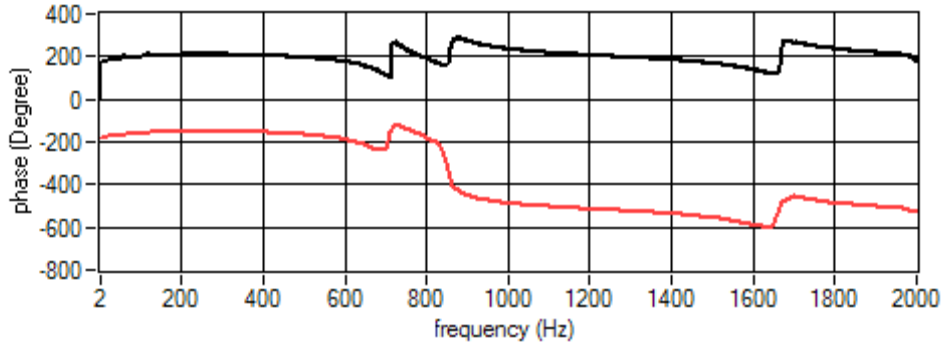


Transfer Function

| | | | | | | | |
|---|---|---|---|---|---|---|---|
| numerator | | | | | | | |
| 0 | -31.475 | -0.0278653 | -3.2133E-6 | -2.81036E-9 | -1.00212E-13 | -8.75965E-17 | -1.0218E-21 |
| denominator | | | | | | | |
| 0 | 8.0363 | 0.00217951 | 1.02073E-6 | 2.04466E-10 | 3.9896E-14 | 5.88681E-18 | 5.60142E-22 |

Transfer Function

| | | | | | | | |
|---|---|---|---|---|---|---|---|
| numerator | | | | | | | |
| 7 | -8.98278E-25 | -3.18553E-30 | -2.84837E-33 | 0 | 0 | 0 | 0 |
| denominator | | | | | | | |
| 7 | 5.72933E-26 | 3.0161E-30 | 1.75387E-34 | 5.214E-39 | 0 | 0 | 0 |

Figure 3-12 Estimated transfer function obtained for bottom radial bearing X sensing direction channel

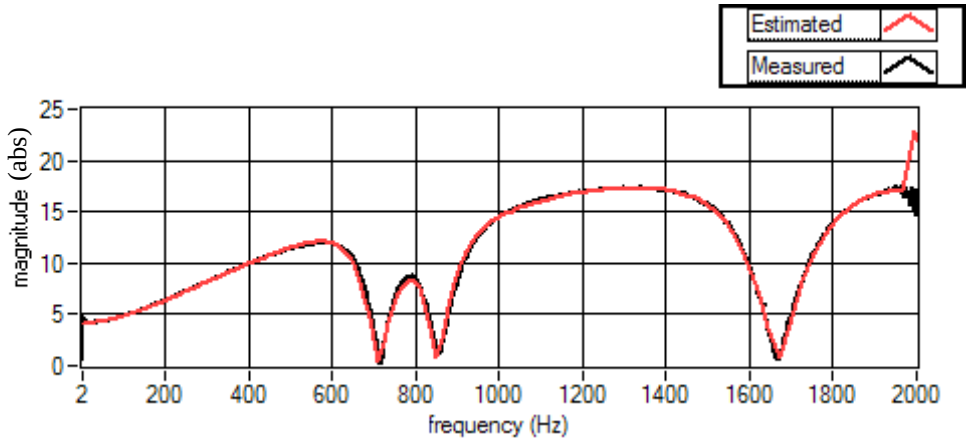


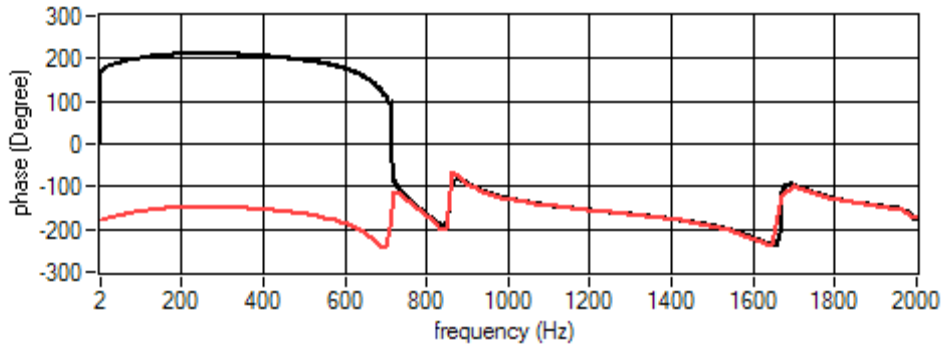


Transfer Function

| | | | | | | | |
|---|---|---|---|---|---|---|---|
| | numerator | | | | | | |
| 0 | -34.0928 | -0.0326081 | -3.48408E-6 | -3.26925E-9 | -1.09643E-13 | -1.01404E-16 | -1.12953E-21 |
| | denominator | | | | | | |
| 0 | 8.24002 | 0.00227145 | 1.03395E-6 | 2.1239E-10 | 4.00595E-14 | 6.12137E-18 | 5.60506E-22 |

Transfer Function

| | | | | | | | |
|---|---|---|---|---|---|---|---|
| | numerator | | | | | | |
| 7 | -1.03765E-24 | -3.55796E-30 | -3.286E-33 | 0 | 0 | 0 | 0 |
| | denominator | | | | | | |
| 7 | 5.9727E-26 | 3.01525E-30 | 1.83214E-34 | 5.214E-39 | 0 | 0 | 0 |

Figure 3-13 Estimated transfer function obtained for bottom radial bearing Y sensing direction channel

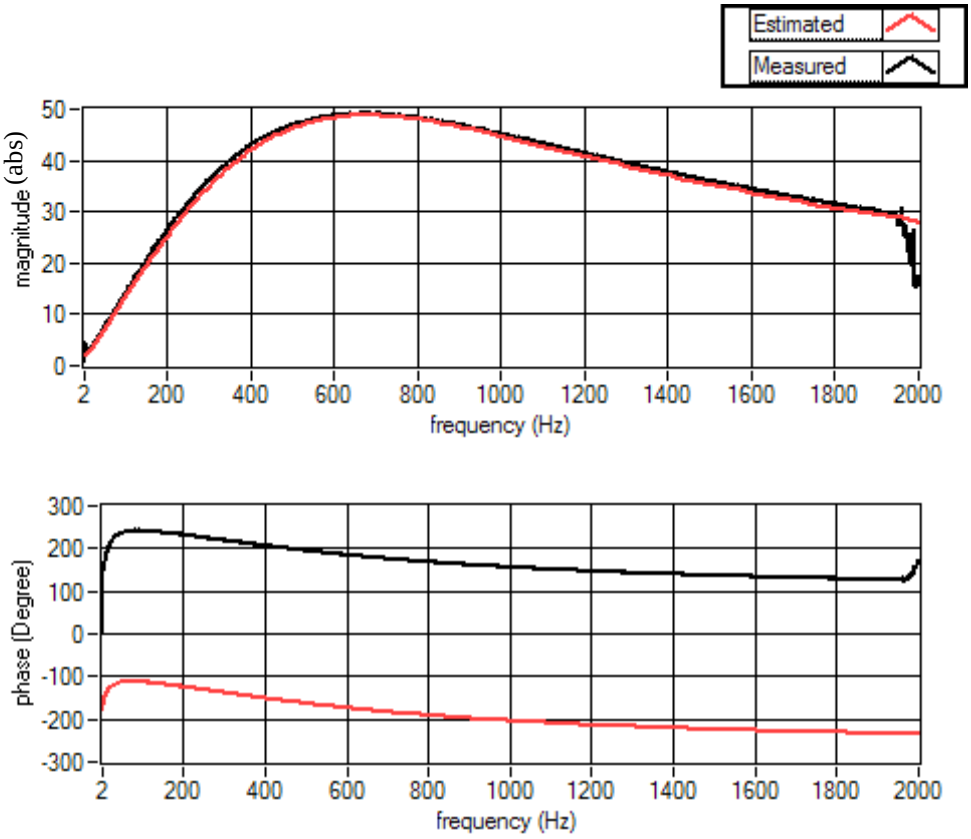


Transfer Function

| | | | | | | | |
|---|---|---|---|---|---|---|---|
| numerator | | | | | | | |
| 0 | -0.422678 | -0.00488613 | 0 | 0 | 0 | 0 | 0 |
| denominator | | | | | | | |
| 0 | 0.228994 | 0.000100271 | 1.26651E-8 | 0 | 0 | 0 | 0 |

Figure 3-14 Estimated transfer function obtained for axial thrust bearing Z sensing direction channel

In order to check the accuracy of the transfer function obtained (with LabVIEW), an analog test was carried out on each channel for which the transfer function was obtained. Figure 3-15 shows the testing procedure. Results showed good correlation between the data obtained and the LabVIEW transfer function as shown in Table 3-3 & Figure 3-16 , Table 3-4 & Figure 3-17 , Table 3-5 & Figure 3-18, Table 3-6 & Figure 3-19 and Table 3-7 & Figure 3-20.

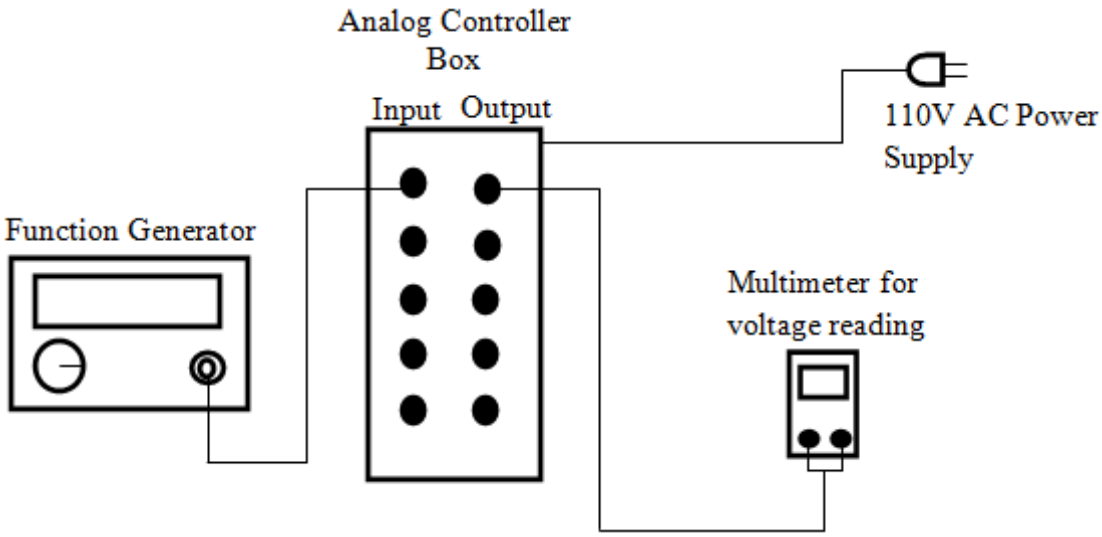


Figure 3-15 Experimental setup to verify the transfer function data obtained from LabVIEW system

Table 3-3 Measured multimeter voltage for RBX1 channel

| **Top Radial Bearing – X direction** | | | | |
|---|---|---|---|---|
| Frequency (Hz) | Input Voltage (V) | Output Voltage (V) | Amplitude (Output/Input) | Expected (from plot) |
| 200 | 0.43 | 2.81 | 6.534 | 6.535 |
| 800 | 0.41 | 3.35 | 8.17 | 7.665 |
| 1600 | 0.4 | 2.88 | 7.2 | 8.185 |
| 1800 | 0.4 | 4.68 | 11.7 | 12.59 |

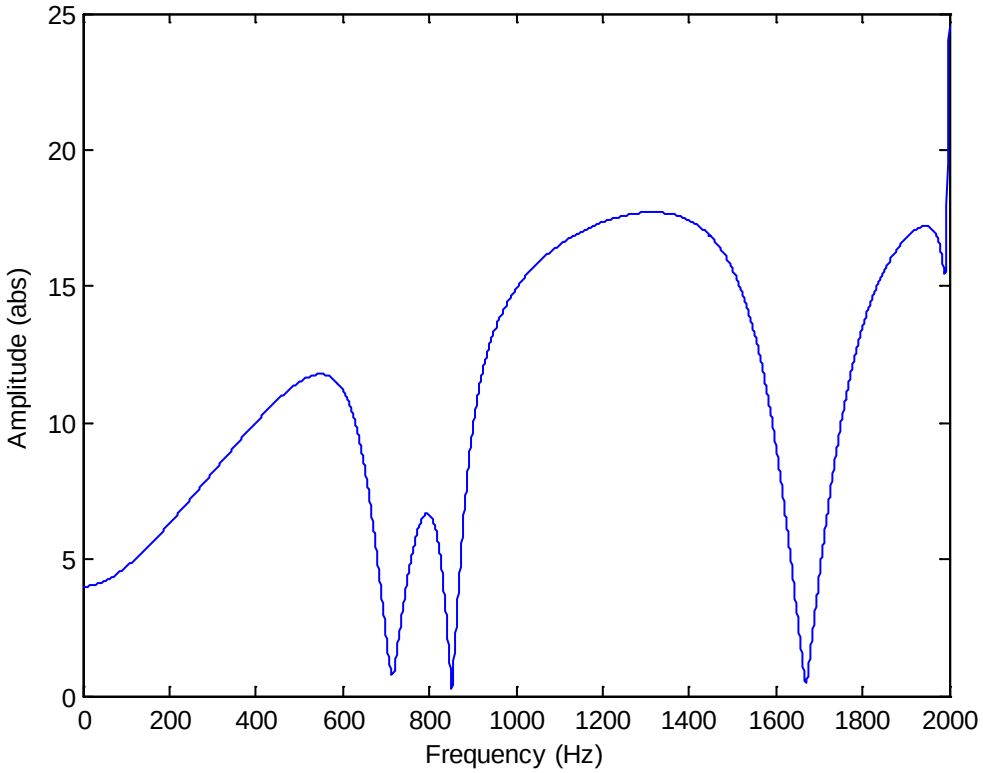


Figure 3-16 Magnitude plot of estimated transfer function for RBX1 channel

Table 3-4 Measured multimeter voltage for RBX2 channel

| **Top Radial Bearing – Y direction** | | | | |
|---|---|---|---|---|
| Frequency (Hz) | Input Voltage (V) | Output Voltage (V) | Amplitude (Output/Input) | Expected (from plot) |
| 200 | 0.45 | 2.77 | 6.155 | 6.156 |
| 1000 | 0.45 | 6.15 | 13.666 | 14.51 |
| 1400 | 0.45 | 6.99 | 15.533 | 16.26 |
| 1600 | 0.45 | 3.965 | 8.811 | 9.74 |

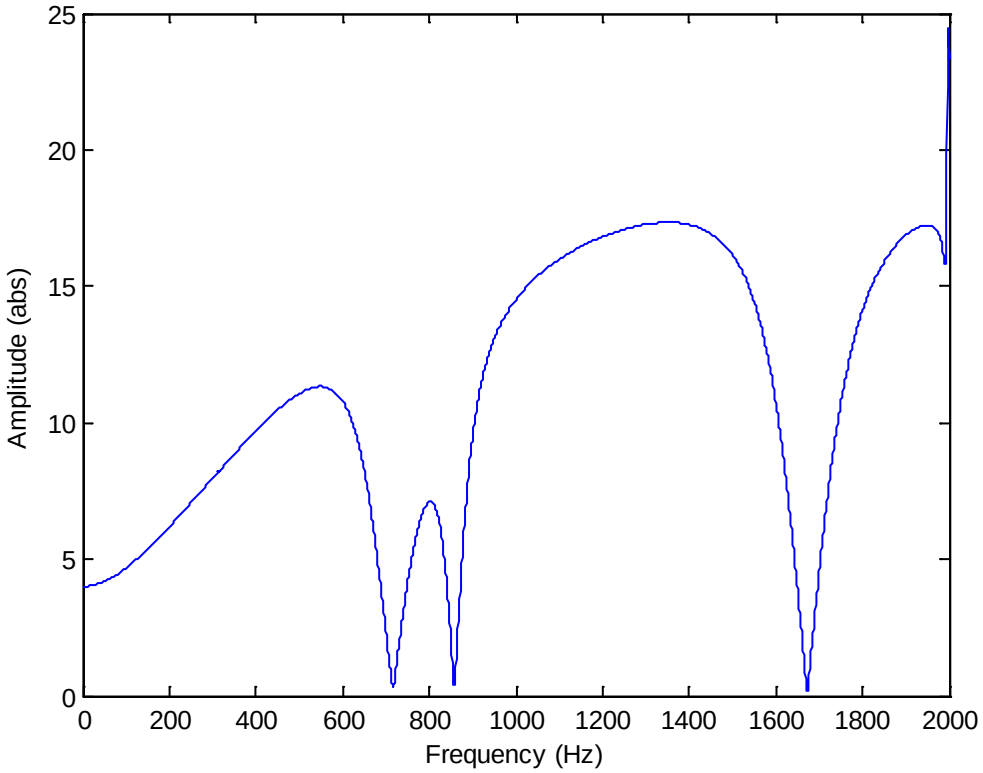


Figure 3-17 Magnitude plot of estimated transfer function for RBX2 channel

Table 3-5 Measured multimeter voltage for CBX1 channel

| **Bottom Radial Bearing – X direction** | | | | |
|---|---|---|---|---|
| Frequency (Hz) | Input Voltage (V) | Output Voltage (V) | Amplitude (Output/Input) | Expected (from plot) |
| 200 | 0.455 | 2.618 | 5.753 | 5.754 |
| 600 | 0.451 | 4.67 | 10.354 | 10.35 |
| 1200 | 0.41 | 6.14 | 14.975 | 14.98 |
| 1800 | 0.4 | 4.55 | 11.375 | 12.16 |

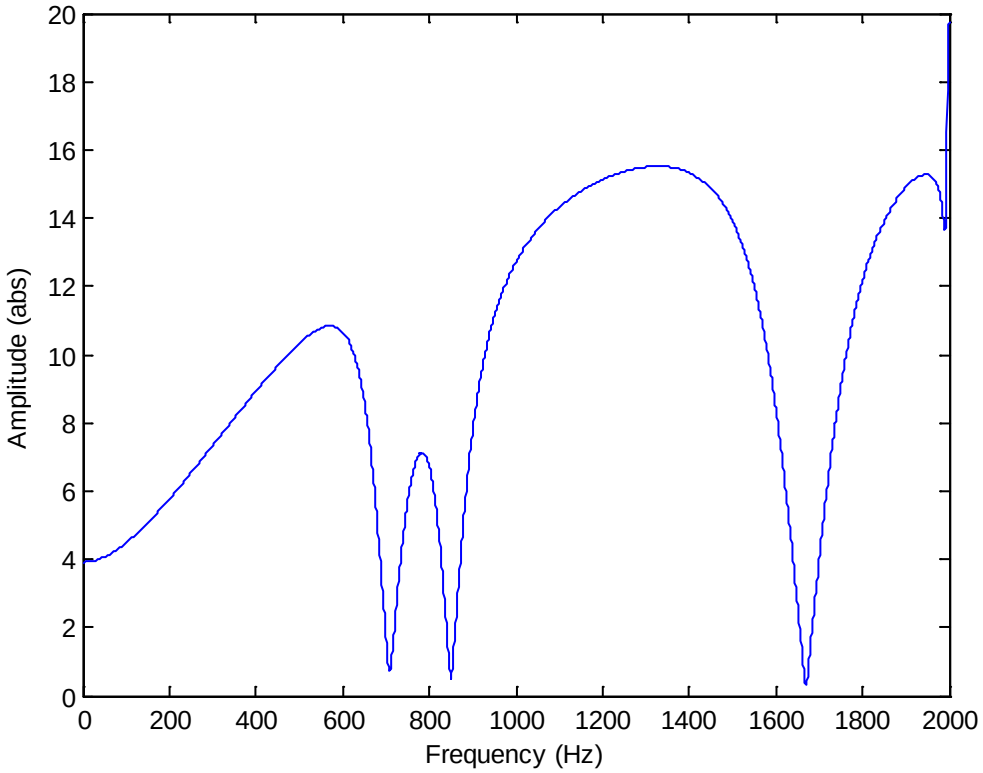


Figure 3-18 Magnitude plot of estimated transfer function for CBX1 channel

Table 3-6 Measured multimeter voltage for CBX2 channel

| **Bottom Radial Bearing – Y direction** | | | | |
|---|---|---|---|---|
| Frequency (Hz) | Input Voltage (V) | Output Voltage (V) | Amplitude (Output/Input) | Expected (from plot) |
| 400 | 0.45 | 4.41 | 9.8 | 9.946 |
| 1000 | 0.41 | 6.18 | 15.073 | 14.51 |
| 1600 | 0.41 | 3.65 | 8.902 | 8.902 |
| 1700 | 0.4 | 1.79 | 4.475 | 4.819 |
| 1800 | 0.4 | 5.94 | 14.85 | 13.91 |

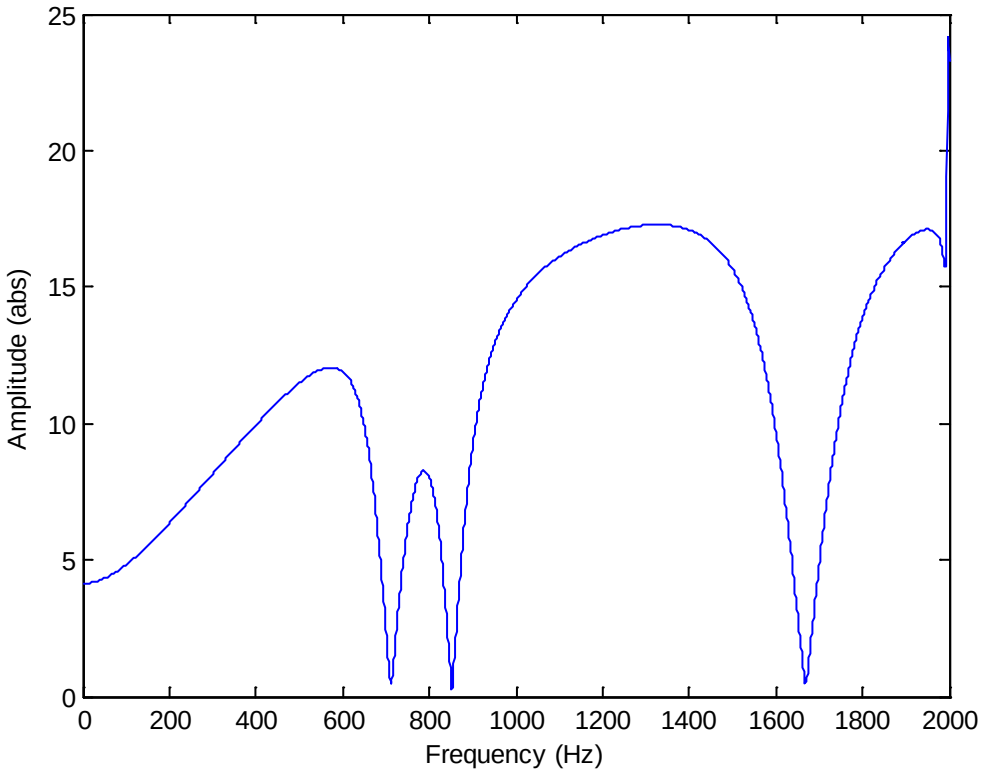


Figure 3-19 Magnitude plot of estimated transfer function for CBX2 channel

Table 3-7 Measured multimeter voltage for axial channel

| **Axial – Z direction** | | | | |
|---|---|---|---|---|
| Frequency (Hz) | Input Voltage (V) | Output Voltage (V) | Amplitude (Output/Input) | Expected (from plot) |
| 0 | 0.0005 | 0.001 | 2 | |
| 5 | 0.35 | 1.35 | 3.857 | 1.964 |
| 10 | 0.35 | 1.105 | 3.157 | 2.281 |
| 20 | 0.342 | 1.312 | 3.836 | 3.253 |
| 30 | 0.339 | 1.679 | 4.952 | 4.419 |
| 35 | 0.339 | 1.863 | 5.4955 | 5.032 |
| 50 | 0.338 | 2.23 | 6.597 | 6.925 |
| 100 | 0.336 | 2.8 | 8.333 | 13.32 |
| 150 | 0.334 | 6.24 | 18.682 | 19.48 |
| 200 | 0.333 | 7.92 | 23.791 | 25.22 |
| 800 | 0.329 | 16.04 | 48.752 | 47.97 |
| 1200 | 0.327 | 13.31 | 40.687 | 40.87 |

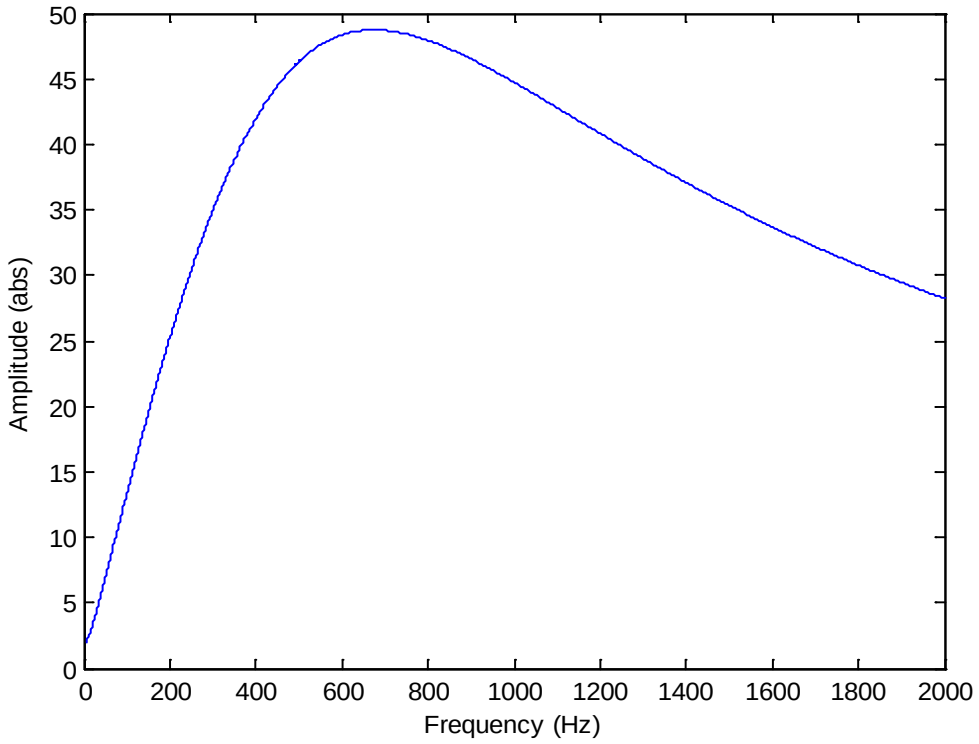


Figure 3-20 Magnitude plot of estimated transfer function for axial channel

### 3.4.1 *Design of lag compensator for axial channel*

From the obtained transfer function of the axial channel, it was observed to have a small gain at low frequencies. In order to comply with the requirements of the system i.e. high gain at low frequencies to take up the dead weight of the vertical rotor assembly and low phase lag for prompt response of the axial controller, a lag compensator stage was decided to be integrated in the axial channel. The requirement of high gain at low frequencies for the axial channel stems from the fact that the rotor is levitated first in the radial direction and then in the axial direction so that the rotor is now fully floating in its magnetic center both radially and axially following which the motor is started to spin the levitated rotor.

A very basic lag compensator [18] is chosen from literature as shown in Figure 3-21.

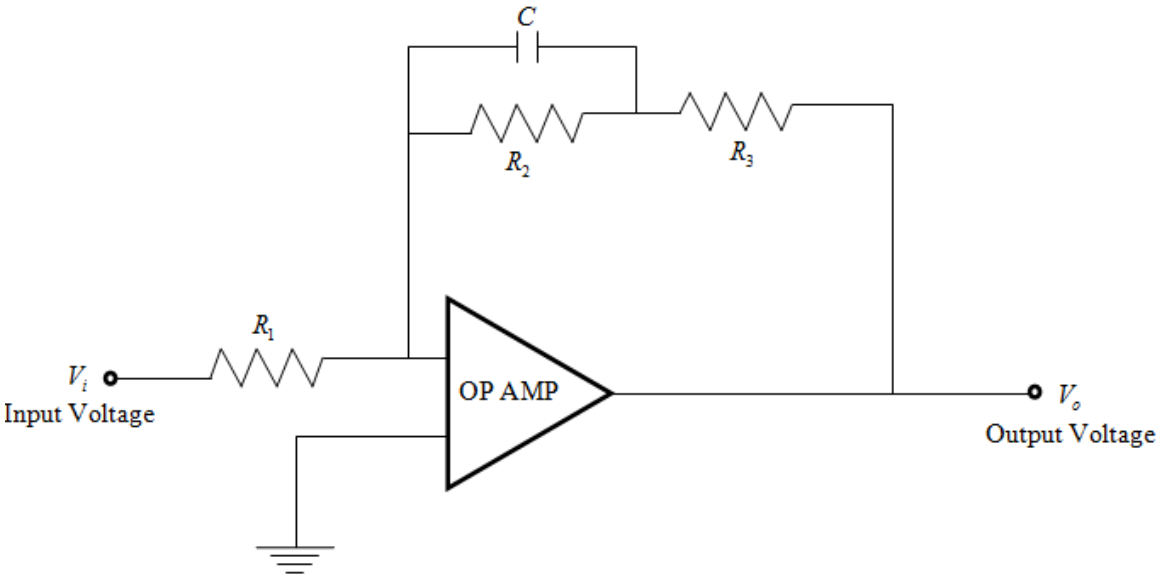


Figure 3-21 Circuit diagram illustration of a simple lag compensator

The transfer function of the above lag compensator can be written as:

$$\frac{V_o}{V_i} = -\frac{R_2 \square X_c + R_3}{R_1} \tag{3.1}$$

Where the resistance due to capacitance is $X_c = \frac{1}{sC}$

$$\frac{V_o}{V_i} = -\frac{\frac{R_2 X_c}{R_2 + X_c} + R_3}{R_1} \tag{3.2}$$

After expanding the above form, we get

$$\frac{V_o}{V_i} = -\frac{R_2 + R_2 R_3 Cs + R_3}{R_1 R_2 Cs + R_1} \tag{3.3}$$

Mathematically simplifying the above expression, we can write

$$T(s) = -a\frac{s+z}{s+p} \tag{3.4}$$

where,

$$a = \frac{R_3}{R_1}$$

$$z = \frac{R_2 + R_3}{R_2 R_3 C}$$

& $p = \frac{1}{R_2 C}$

The negative term is due to the fact that the input is given to the inverting terminal of the Op-amp. Hence an input sinewave is 180° out of phase with its output sinewave as shown in Figure 3-22.

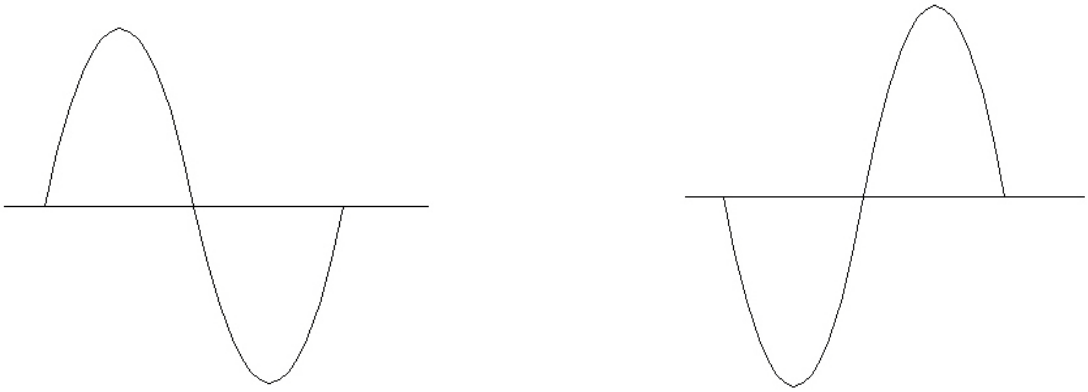

(a) Input sinewave (b) Output sinewave

Figure 3-22 Input sinewave 180° out of phase from its output sinewave

DC gain (s = 0) is obtained by

$$\left.\frac{V_o(s)}{V_i(s)}\right|_{s=0} = a\frac{z}{p} = \frac{R_2 + R_3}{R_3} \tag{3.5}$$

High frequency gain (s = inf) is obtained by

$$\left.\frac{V_o(s)}{V_i(s)}\right|_{s=\infty} = a = \frac{R_3}{R_1} \tag{3.6}$$

Since the lag compensator has to handle the dead weight of the rotor shaft at zero speed, it should have high gain at low frequencies and should not affect the functioning of the axial controller at high frequencies. Hence keeping a high frequency gain of unity we select:

$a = 1 \Rightarrow R_3 = R_1$

The low frequency or DC gain is given by Equation (3.5).

A widely used general OP37 op-amp is selected to implement the above lag compensator on a breadboard; similarly an arbitrary value for the resistors $R_2 = 50,000$ ohms and $R_1 = R_3 = 2000$ ohms is chosen. Selection of the capacitance value was done after an exhaustive analysis for different values keeping the minimum phase lag and unity DC gain in mind. Increasing the capacitance value minimizes the phase lag theoretically but experimentally (with LabVIEW) it was observed to affect the high frequency unity gain by settling at 0.6 to 0.7 instead of 1. Finally, a capacitance value of $C = 100$ microfarad was found to work best under the given constraints. Using the same LabVIEW method described in 3.4, the performance of the above lag compensator for a frequency of up to 50 Hz (arbitrarily selected) was recorded. In order to obtain the transfer function from this recorded performance, a curve fitting was done between the measured and estimated data by trying different orders of numerator and denominator. Figure 3-23 shows the obtained curve fitting between the measured and estimated data.

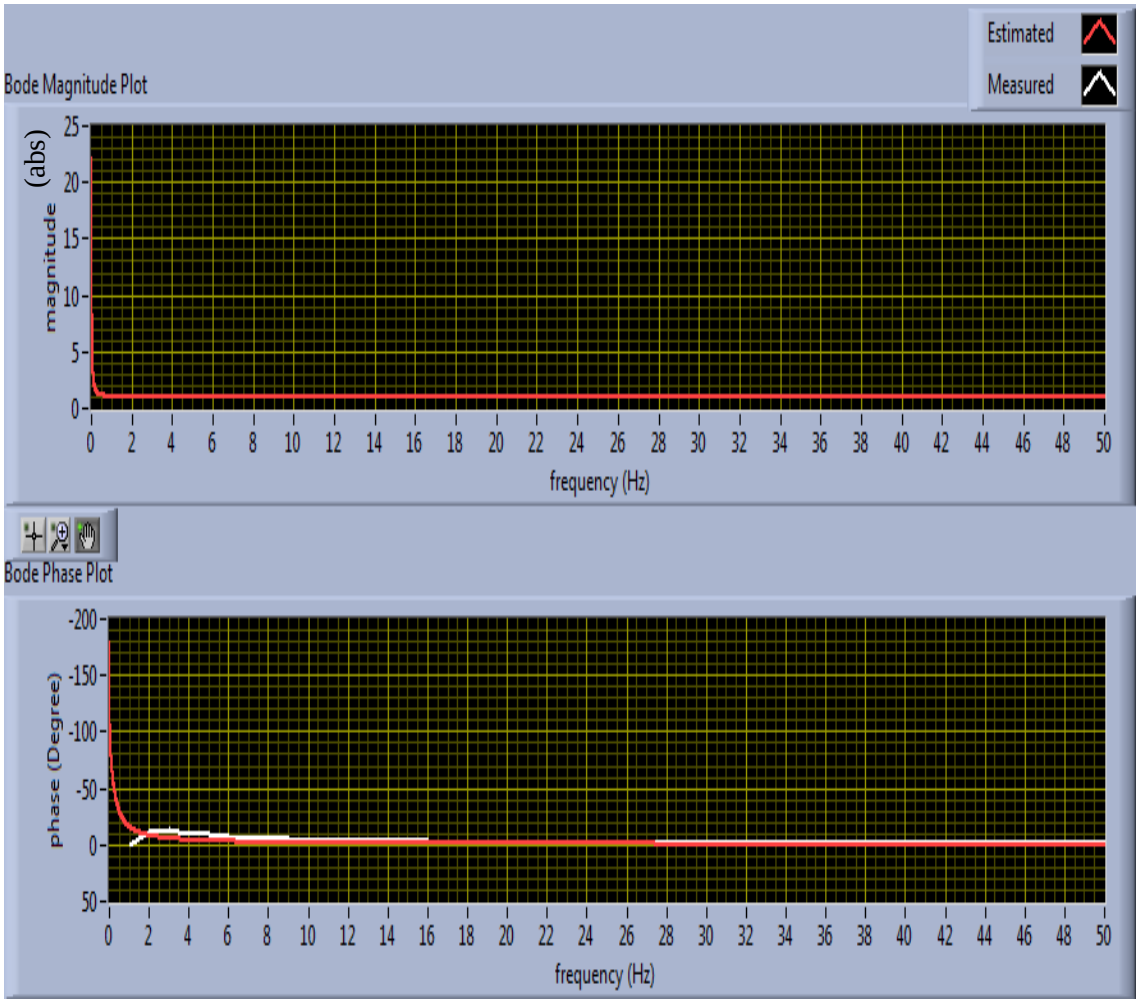


Figure 3-23 Front panel screenshot showing the curve fitting between the measured and curve fit bode plot data

Plotting the estimated and theoretical transfer function in Matlab, we get Figure 3-24:

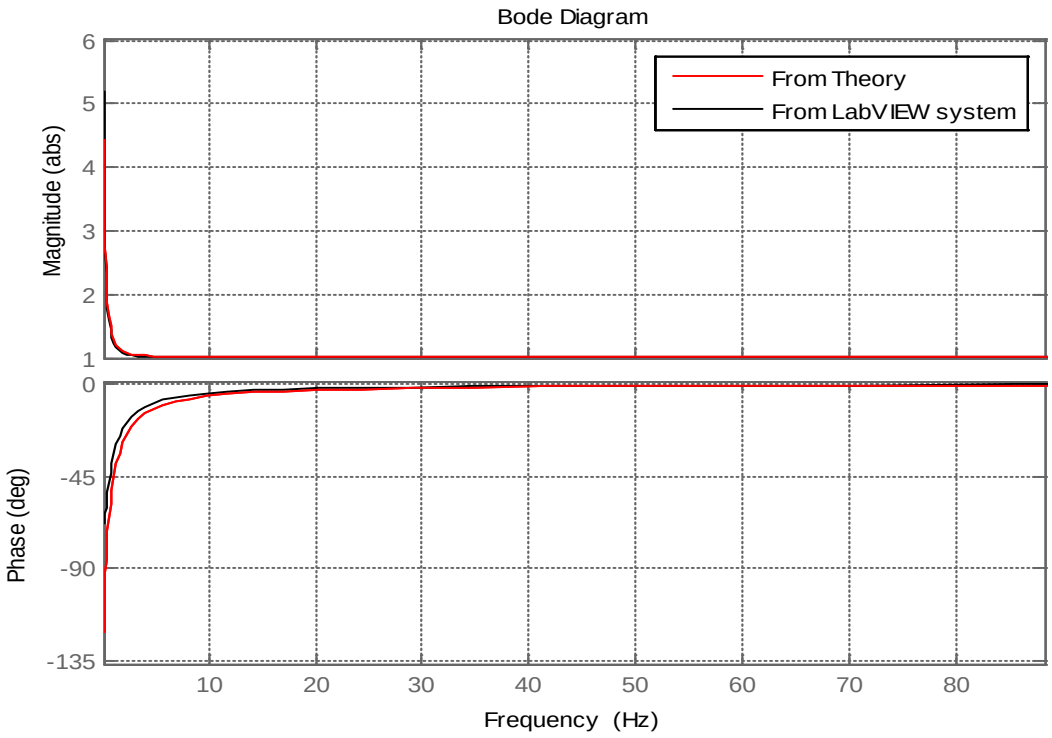


Figure 3-24 Superimposed bode plots of theoretical and estimated transfer function

The results, obtained after superimposing the plots in Matlab, show good correlation between the theoretical and experimentally realized compensator.

### 3.4.2 *Stability of the lag compensator integrated axial controller for the axial direction of the magnetic bearing system*

The transfer function of the axial controller (as recorded in section 3.4) is given by:

$$TF_{Axial} = \frac{-0.422678 - 0.00488613s}{0.228994 + 0.000100271s + 1.26651e-8s^2} \quad (3.7)$$

Plotting the bode plot of the above transfer function in Matlab, we get Figure 3-25:

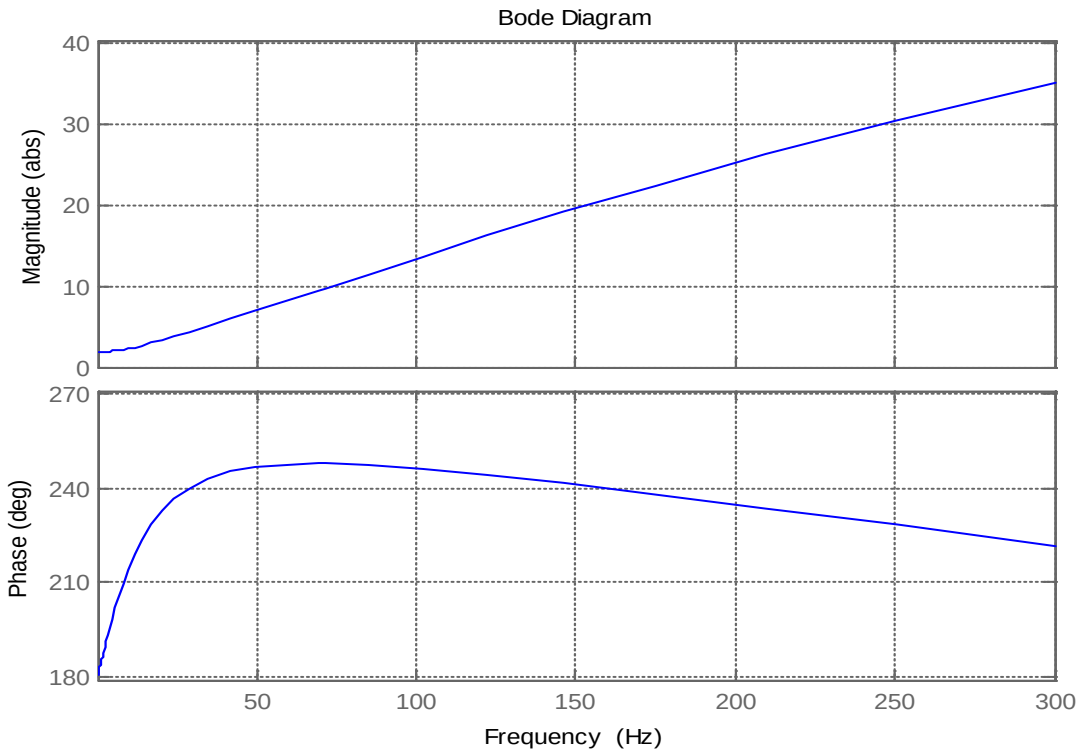


Figure 3-25 Bode plot of the axial controller channel

The transfer function of the realized lag compensator is given by:

$$TF_{LagCompensator} = -\frac{s+5.2}{s+0.2} \tag{3.8}$$

Plotting the transfer function (Equation (3.8)) in Matlab, we get Figure 3-26:

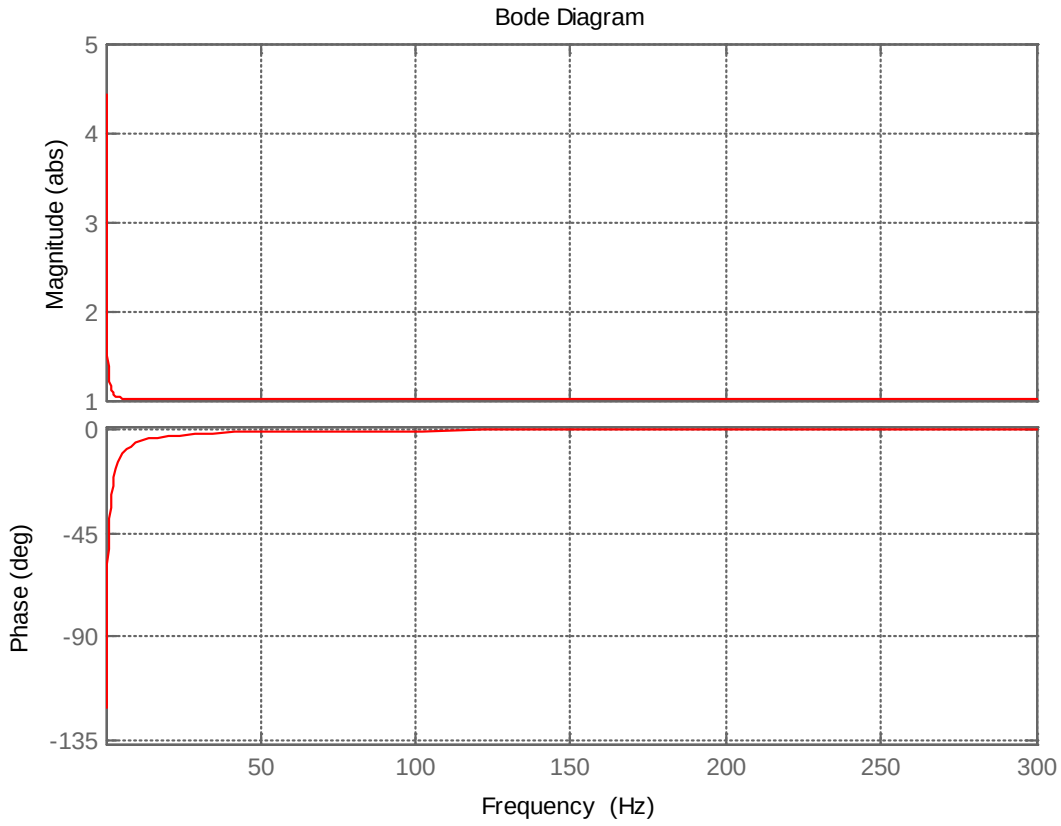


Figure 3-26 Bode plot of the realized lag compensator

Combining the two transfer functions (Equation (3.7) and (3.8)) since the lag compensator is integrated into the axial channel, we get

$$TF_{Controller} = \frac{0.01466s^2 + 1.344s + 6.594}{1.267e-008s^3 + 0.0001003s^2 + 0.229s + 0.0458} \quad (3.9)$$

Plotting the transfer function (Equation (3.9)) in Matlab, we get Figure 3-27:

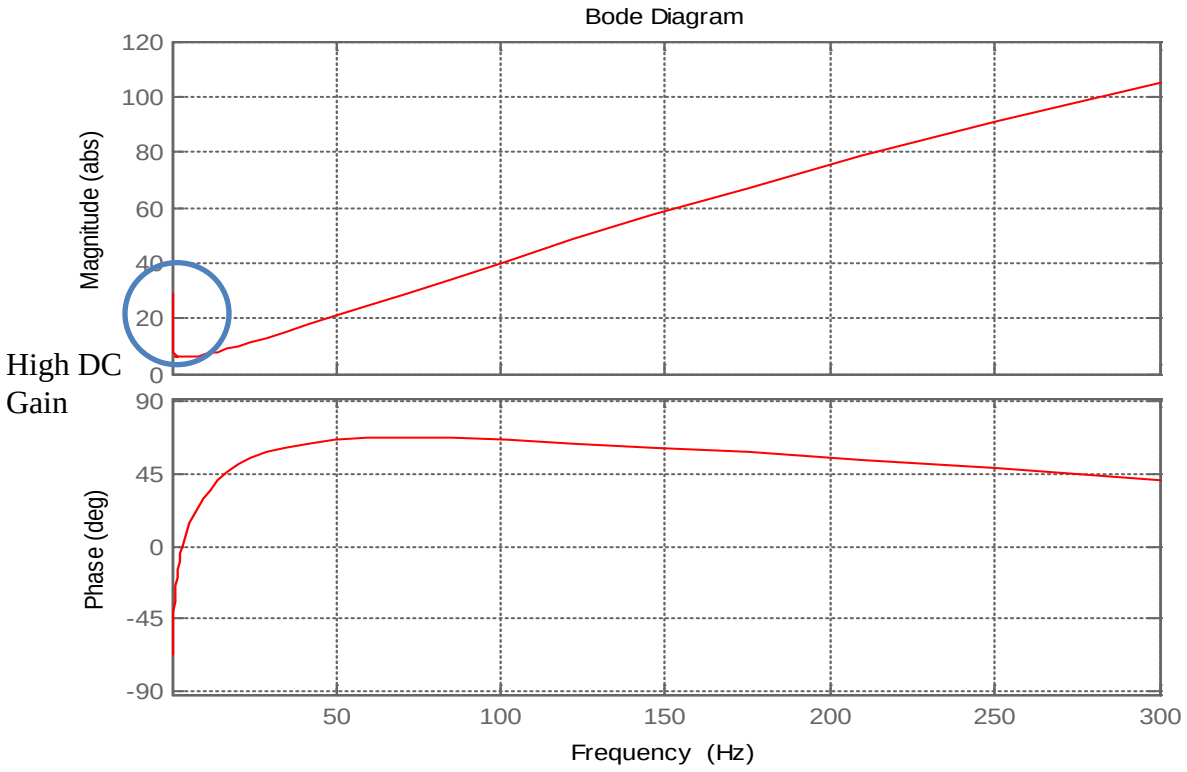


Figure 3-27 Bode plot of the axial channel integrated with the designed lag compensator

The increase in DC gain at zero frequency can be seen from Figure 3-27. To check for stability, we convert the above transfer function into state space form and integrate it into the system equations of motion to find the resulting eigenvalues.

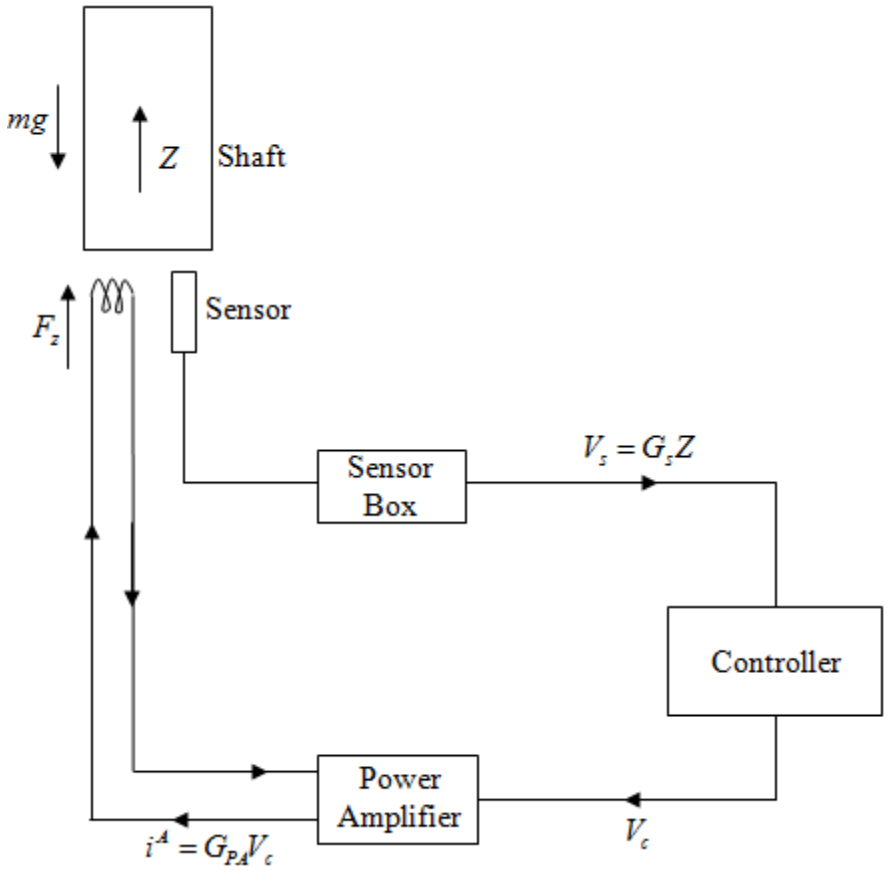


Figure 3-28 Simplified diagram of the axial control scheme

The transfer function for the axial controller can be written in the form:

$$TF_{Controller} = \frac{Output}{Input} = \frac{V_c(s)}{V_s(s)} \tag{3.10}$$

In a state space form, it can be written as:

$$\dot{\underline{W}}_c = \underline{A}_c \underline{W}_c + \underline{B}_c u \tag{3.11}$$

$$V_c = \underline{Y}_c = \underline{C}_c \underline{W}_c \tag{3.12}$$

where,

$V_c$ - Output controller voltage

$i^A$ - Power amplifier current in the axial direction

$G_{PA}$ - Gain of the power amplifier

$$i^A = G_{PA} V_C = G_{PA} \underline{C}_c \underline{W}_c \tag{3.13}$$

$V_s$ - Input sensor voltage

$G_s$ - Gain of the sensor

$N_s$ - Sensor noise

$z$ - Z coordinate

$$u = V_s = -G_s z + N_s(t) \tag{3.14}$$

Converting the transfer function (Equation 3.10) into state space form using 'tf2ss' command in Matlab & using the property values of the system, we get:

$$A_c = \begin{bmatrix} -0.0008e+007 & -1.8082e+007 & -0.3616e+007 \\ 1 & 0 & 0 \\ 0 & 1 & 0 \end{bmatrix} \tag{3.15}$$

$$B_c = \begin{bmatrix} 1 \\ 0 \\ 0 \end{bmatrix} \tag{3.16}$$

$$C_c = \begin{bmatrix} 0.0116e+008 & 1.0614e+008 & 5.2063e+008 \end{bmatrix} \tag{3.17}$$

Writing equations of motion from Figure 3-28, we get:

$$m\ddot{Z} = -mg + F_Z \tag{3.18}$$

where,

Magnetic bearing control force $F_Z = K_i i^A + K_p Z$

In first order form, we can write:

$$\dot{V}_Z = \ddot{Z} = -g + \frac{1}{m}\left\{K_i i^A + K_p Z\right\} \tag{3.19}$$

$$\dot{Z} = V_Z \tag{3.20}$$

Choosing X as a state variable of the form:

$$\underline{X} = (Z \quad V_Z \quad W_{c1} \quad W_{c2} \quad W_{c3}) \tag{3.21}$$

Hence writing Equation (3.19) in a state space form, we get

$$\dot{\underline{X}} = \underline{A}\underline{X} + \underline{B}u \tag{3.22}$$

Therefore using Equations (3.19), (3.20) (3.21) & (3.22), we get:

$$\underline{A} = \begin{bmatrix} 0 & 1 & 0 & 0 & 0 \\ 0.0002e+009 & 0 & 0.0058e+009 & 0.5327e+009 & 2.6130e+009 \\ -8000 & 0 & -7917.3 & -0.0181e+009 & -0.0036e+009 \\ 0 & 0 & 1 & 0 & 0 \\ 0 & 0 & 0 & 1 & 0 \end{bmatrix} \tag{3.23}$$

$$\underline{B} = \begin{bmatrix} 0 \\ -9.81 \\ N_s \\ 0 \\ 0 \end{bmatrix} \tag{3.24}$$

To check for the stability of this closed loop axial system, we can check the eigenvalues of the $\underline{A}$ matrix derived above since the eigenvalues of a linear dynamic system are always independent of its mathematical description [17].

Using the 'eig' command in Matlab to compute the eigenvalues of this A matrix, we get:

$$ans = \begin{bmatrix} -6.1967e+03 \\ -8.4522e+02+2.5483e+03i \\ -8.4522e+02-2.5483e+03i \\ -15.0921+15.0744i \\ -15.0921-15.0744i \end{bmatrix} \tag{3.25}$$

The above matrix shows all negative real parts and hence satisfying the criterion for stability. Thus the new axial channel controller closed loop system is stable.

To obtain the step response of this axial system, we can convert it back to transfer function form using 'ss2tf' command in Matlab and solve for the step response. The sensor noise $N_s$ is represented with the 'rand' command in Matlab which generates random numbers. Similarly the $\underline{C}$ matrix for the state space system can be chosen to be:

$$\underline{C} = \begin{bmatrix} 1 & 0 & 0 & 0 & 0 \end{bmatrix} \tag{3.26}$$

This choice of $\underline{C}$ is governed by the fact that we want to see the output displacement as a function of time. Figure 3-29 shows the step response of the output

displacement as a function of time.

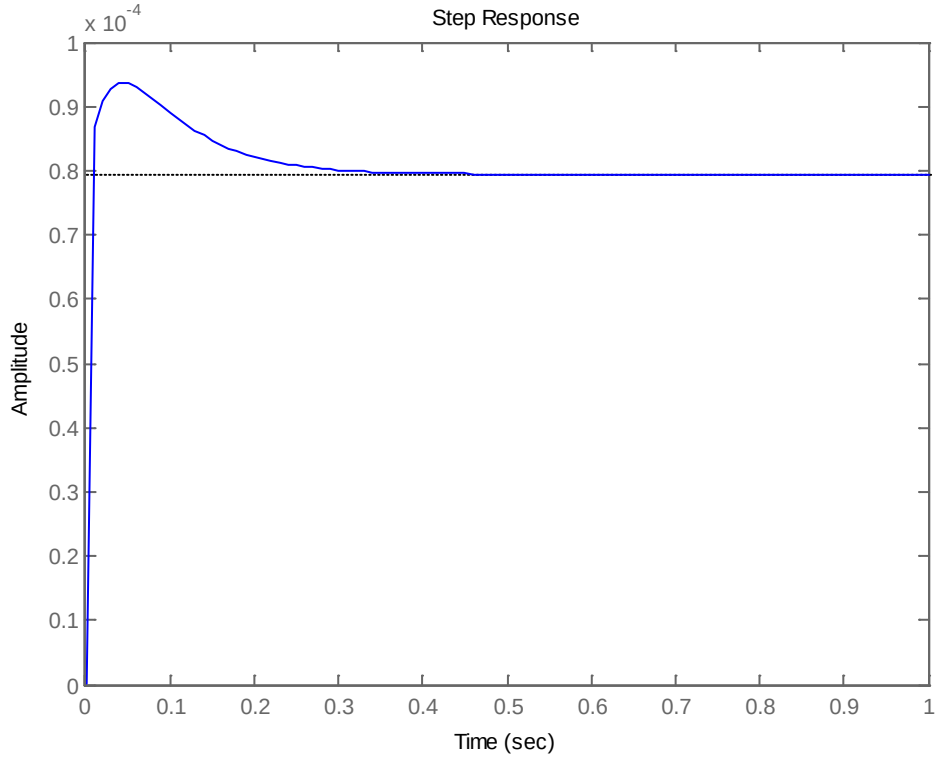


Figure 3-29 Step response of the axial transfer function

## 3.5 Gain amplifier

After simulating the complete system in Matlab, a need for amplification of the proportional and derivative gains by an integer value was needed to make the system stable i.e. for negative real parts of the eigenvalues of the complete closed loop system. This multiplication by an integer value of the controller output is achieved externally by

the gain amplifier (Figure 2-7) which multiplies the output of the controller by the gain value it is set at.

An experimental test was performed on the instrument to test its characteristics. Figure 3-30 shows the experimental setup and Table 3-8 shows the tabular data recorded.

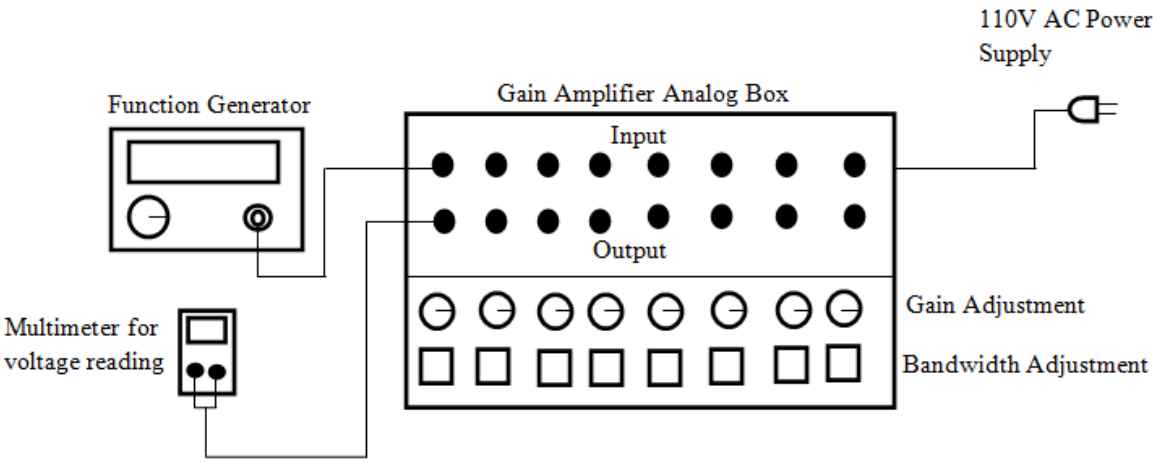


Figure 3-30 Experimental setup to test the external gain amplifier

Table 3-8 Tabular data recorded from the gain amplifier

| **Test Data for Gain Amplifier** | | | | | | | |
|---|---|---|---|---|---|---|---|
| INPUT | | | | | | | |
| Vin = 0.532 V AC<br>Fc = 1000 Hz<br>Bandwidth = 10,000 Hz | | | | | | | |
| | OUTPUT | | | | | | |
| INPUT DC | | Gain = 1 | | Gain = 2 | | Gain = 5 | |
| VOLTAGE | Channel | DC | AC | DC | AC | DC | AC |
| -0.0121 V | 1 | -0.012 V | 0.536 V | -0.022 V | 1.069 V | -0.054 V | 2.674 V |
| -0.009 V | 2 | -0.009 V | 0.531 V | -0.019 V | 1.065 V | -0.046 V | 2.670 V |
| -0.009 V | 3 | -0.009 V | 0.531 V | -0.018 V | 1.065 V | -0.044 V | 2.668 V |
| -0.008 V | 4 | -0.042 V | 0.536 V | -0.050 V | 1.071 V | -0.074 V | 2.681 V |
| -0.008 V | 5 | -0.015 V | 0.530 V | -0.022 V | 1.065 V | -0.044 V | 2.669 V |
| -0.007 V | 6 | -0.0075 V | 0.533 V | -0.013 V | 1.064 V | -0.031 V | 2.662 V |
| -0.007 V | 7 | -0.007 V | 0.530 V | -0.013 V | 1.064 V | -0.032 V | 2.664 V |
| -0.0062 V | 8 | -0.005 V | 0.532 V | -0.011 V | 1.064 V | -0.029 V | 2.664 V |

### 3.6 Current distribution matrix (CDM) box

The magnetic bearings used in this research are novel in nature in that they are Fault Tolerant (a feature improving the factor of reliability). This feature delivers desired magnetic control forces even after termination of coil currents to a subset of "failed poles" i.e. it provides stable continued operation of the magnetic bearing in case of sudden failure of a coil or a power amplifier [6]. High speeds of the rotating machinery using magnetic suspension make this feature an important desirable characteristic.

Fault Tolerant Control (FTC) is achieved using the concept of Flux coupling wherein the coil current of one pole can drive the flux through other poles. This is enabled by a CDM box which adjusts the currents and fluxes following a pole set failure. However, this approach causes a reduction in the load capacity due to the redistribution of fluxes to compensate for the failed poles [19].

Li [19] and Na [20] had performed generic work on Homopolar and Heteropolar magnetic bearing CDM models. Using the same approach, their work has been extended to the EEC universal magnetic bearing system and CDM matrix values have been determined for no-pole failed and six different one-pole failed cases. These matrix values show the ratios between the corresponding currents in the six coils which have to be in the same proportion corresponding to the 2 independent x and y controller output voltages (Figure 2-7). Figure 3-31 & Figure 3-32 show the CDM matrix values (no pole failure cases) for θ at 0° and 30° for 70F and 1000F.

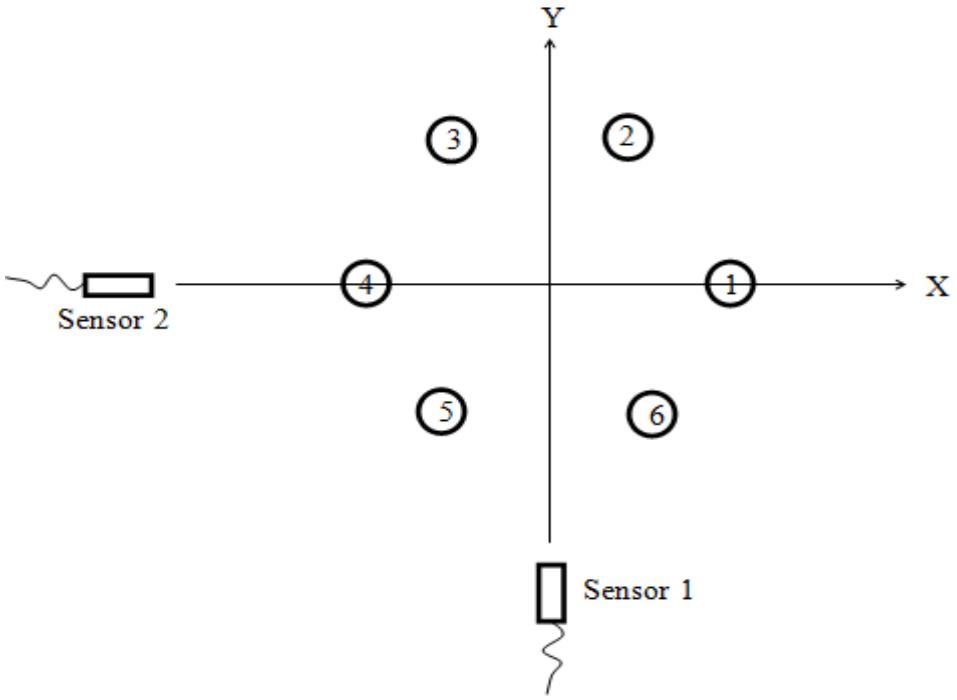


Figure 3-31 Pole orientation along the X-Y axis for θ = 0°

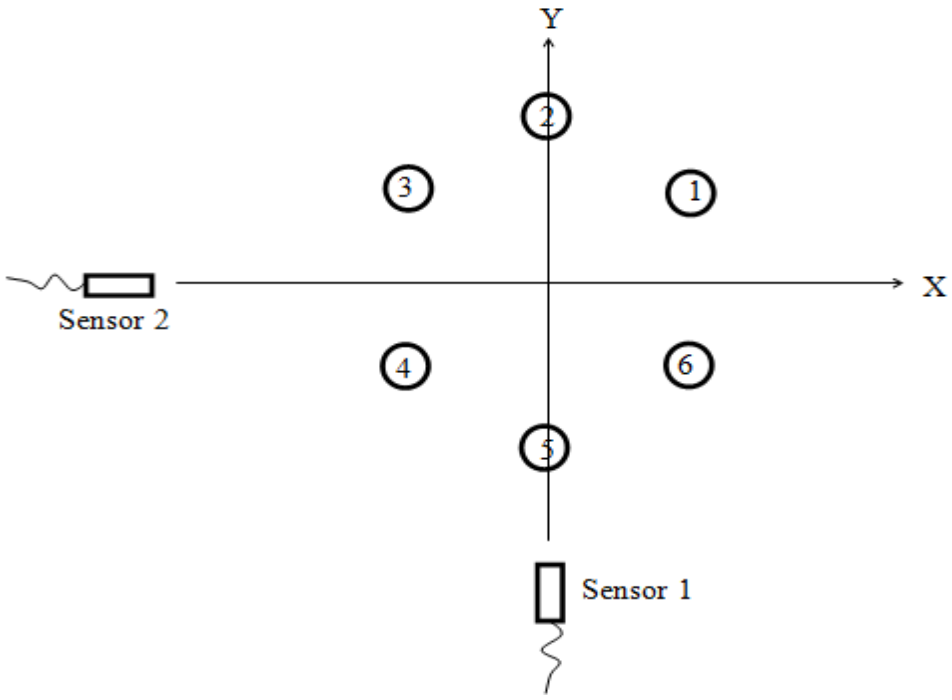


Figure 3-32 Pole orientation along the X-Y axis for θ = 30°

| X | Y | |
|---|---|---|
| 0.03149930336636 | –0.00000000006218 | 1 |
| 0.01571002981445 | 0.02737226267683 | 2 |
| –0.01571003004741 | 0.02737226270353 | 3 |
| –0.03149930358775 | –0.00000000009308 | 4 |
| –0.01571003004870 | –0.02737226283963 | 5 |
| 0.01571002981574 | –0.02737226287490 | 6 |

CDM matrix values for θ = 0° at 70F

| X | |
|---|---|
| 0.02737226277384 | 0.01571002995949 | 1 |
| –0.00000000000002 | 0.03149930344911 | 2 |
| –0.02737226277364 | 0.01571002995949 | 3 |
| –0.02737226277374 | –0.01571002995961 | 4 |
| 0.00000000000011 | –0.03149930344919 | 5 |
| 0.02737226277367 | –0.01571002995961 | 6 |

CDM matrix values for θ = 30° at 70F

| X | Y | |
|---|---|---|
| 0.05852513794303 | 0.00000000337477 | 1 |
| 0.02922834558135 | 0.05067567514935 | 2 |
| –0.02922834569820 | 0.05067567863220 | 3 |
| –0.05852513737949 | –0.00000000028666 | 4 |
| –0.02922834598693 | –0.05067567253640 | 5 |
| 0.02922834586993 | –0.05067567638454 | 6 |

CDM matrix values for θ = 0° at 1000F

| X | Y | |
|---|---|---|
| 0.05067567712496 | 0.02922833581427 | 1 |
| –0.00000000272113 | 0.05852513571960 | 2 |
| –0.05067567563926 | 0.02922833568004 | 3 |
| –0.05067567630542 | –0.02922834748790 | 4 |
| –0.00000000064739 | –0.05852514785735 | 5 |
| 0.05067567363477 | –0.02922834762020 | 6 |

CDM matrix values for θ = 30° at 1000F

For the EEC test rig, the CDM matrix values for θ = 0° at 1000F are taken into consideration due to the similar mounting state of the sensors on the actual system as shown in Figure 3-33. In order to check consistency with the derived model results, an experimental test (shown in Figure 3-34) was conducted on the two CDM boxes with a 3.01 V input and the data is tabulated in the Table 3-9. Results show good correlation between the obtained data and the derived model.

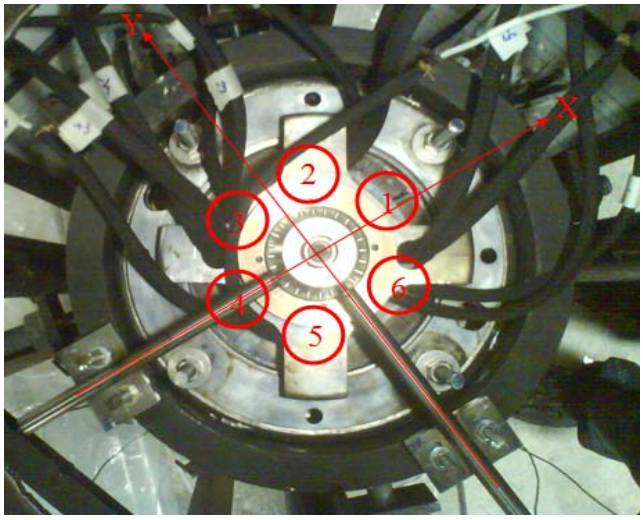


Figure 3-33 Sensor oreintation on the actual system (θ = 0°)

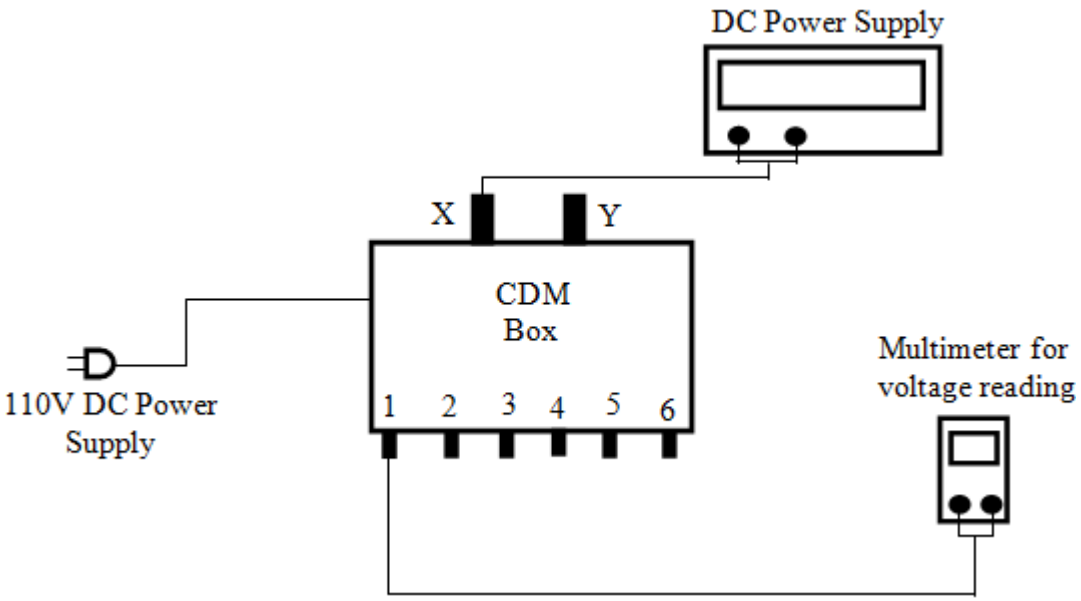


Figure 3-34 Experimental setup to test the current distribution matrix (CDM) boxes

Table 3-9 Tabular data recorded from the 2 CDM boxes for 3.01V input voltage

| | Top Radial Bearing | | Bottom Radial Bearing | |
|---|---|---|---|---|
| | X | Y | X | Y |
| 1 | 2.42 | 0 | 2.5 | 0 |
| 2 | 1.2 | 2.1 | 1.3 | 2.31 |
| 3 | -1.2 | 2.11 | -1.2 | 2.31 |
| 4 | -2.42 | 0.01 | -2.5 | 0 |
| 5 | -1.23 | -2.14 | -1.2 | -2.31 |
| 6 | 1.21 | -2.11 | 1.3 | -2.31 |

### 3.7 Power amplifier (servo amplifier)

The power amplifiers, used are from Copley Controls Ltd. (PST-075-10-F), act as servoamplifiers in making the output current to the bearing coils follow in phase with the input voltage from the controller output besides amplifying the current value. Figure 3-36 shows the bode plot of a single power amplifier obtained using the experimental setup shown in Figure 3-35.

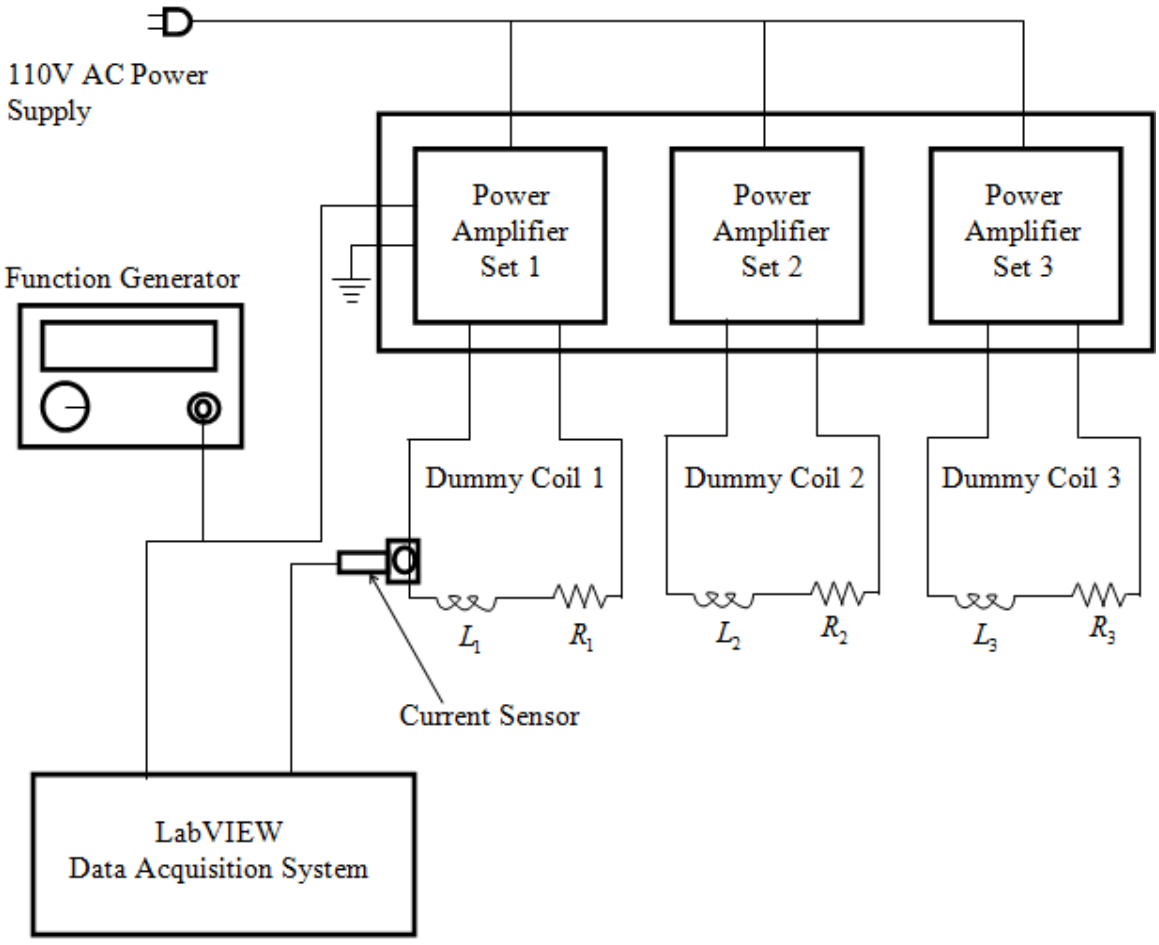


Figure 3-35 Experimental setup to measure the transfer function of the power amplifiers

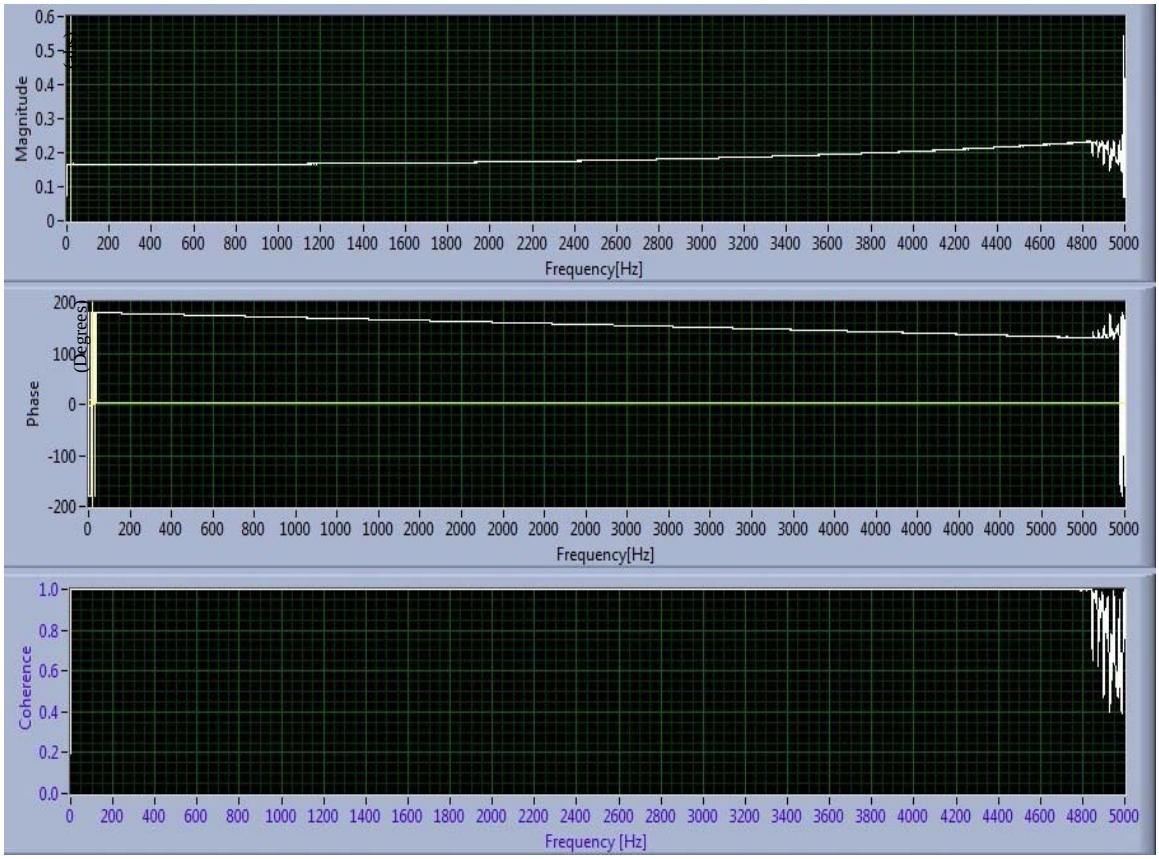


Figure 3-36 Screenshot of the front panel LabVIEW system showing the estimated bode plot of the power amplifier

From the bode plot, it can be seen that the bandwidth of the power amplifier is very high which is in lieu with its requirement i.e. the bandwidth of a power amplifier in a magnetic bearing system should be high enough to incorporate the entire dynamics of the complete closed loop plant model. A simplified diagram of the power amplifier control scheme is shown in Figure 3-37.

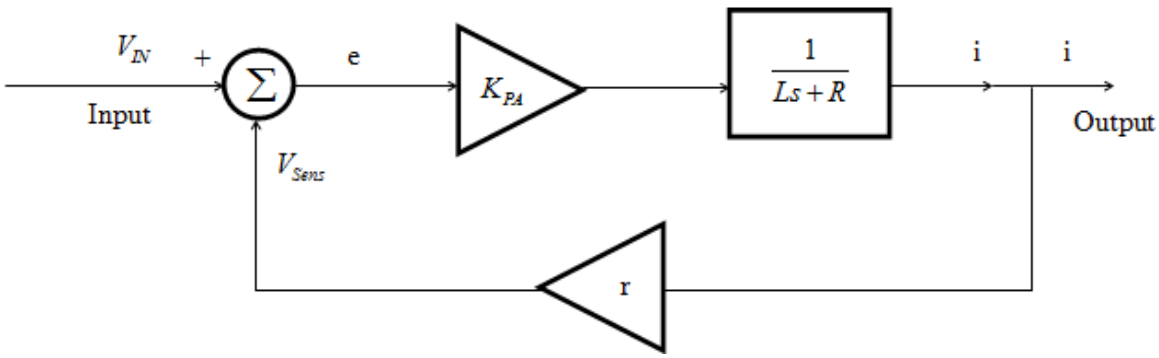


Figure 3-37 Simplified control scheme of the power amplifier

### 3.7.1 *Extra dummy inductance load*

The power amplifiers used for the EEC universal system require a target load inductance at its output of 400 µH to 40 mH. Due to the shortcoming of the wound magnetic bearing coils in providing this target load, additional dummy inductance coils of 200 µH inductance had to be added in series with the bearing coils just to increase their net inductance load. Figure 3-39 shows the arrangement employed.

## 3.8 Radial bearing flux testing

The control and bias flux values for each pole of the two radial bearings was determined using a power supply and a flux meter setup shown in Figure 3-38. These tests were reconducted at room temperature even though work was done on it in [6] and [16], to check for consistency. Results showed a reversed polarity in one of the poles of the bottom bearing. The data obtained is tabulated in Table 3-10. All the poles are numbered to enable proper alignment of poles between the top and bottom radial bearings during assembly of the complete system i.e. when the assembly is seen from the top view,

pole 1 on the top bearing should see pole 1 on the bottom bearing. This arrangement helps in making appropriate connections between the bearings and to the external connections from the power amplifiers.


Figure 3-38 Experimental setup showing the flux testing procedure [1]

Table 3-10 Voltage and Flux Data for top and bottom bearing poles

(a) Data for top radial bearing

| TOP BEARING | | | | |
|---|---|---|---|---|
| Pole | Top / Bottom Plane | Voltage | No Current Flux B (Tesla) | With Current Flux B (Tesla) |
| 1 | Top | -0.515 | -0.049 | -0.063 |
| 2 | Top | -0.515 | -0.023 | -0.027 |
| 3 | Top | -0.496 | -0.026 | -0.033 |
| 4 | Top | -0.465 | -0.052 | -0.065 |
| 5 | Top | -0.518 | -0.054 | -0.072 |
| 6 | Top | -0.491 | -0.12 | -0.155 |
| 1 | Bottom | -0.522 | 0.044 | 0.052 |
| 2 | Bottom | -0.541 | 0.021 | 0.022 |
| 3 | Bottom | -0.533 | 0.021 | 0.024 |
| 4 | Bottom | -0.533 | 0.035 | 0.043 |
| 5 | Bottom | -0.466 | 0.051 | 0.063 |
| 6 | Bottom | -0.558 | 0.057 | 0.072 |

(b) Data for bottom radial bearing

| BOTTOM BEARING | | | | | |
|---|---|---|---|---|---|
| Pole | Top / Bottom Plane | Voltage | No Current Flux B (Tesla) | With Current Flux B (Tesla) | |
| 1 | Top | -0.459 | -0.019 | -0.022 | |
| 2 | Top | -0.464 | -0.018 | -0.015 | |
| 2 | Top | 0.435 | -0.021 | -0.023 | Repeat |
| 2 | Top | 0.44 | -0.019 | -0.022 | Repeat |
| 2 | Top | 0.45 | -0.021 | -0.023 | Repeat |
| 2 | Top | 0.38 | -0.022 | -0.025 | Repeat |
| 2 | Top | 0.435 | -0.021 | -0.017 | Repeat |
| 3 | Top | -0.42 | -0.037 | -0.041 | |
| 4 | Top | -0.508 | -0.155 | -0.178 | |
| 5 | Top | -0.489 | -0.036 | -0.041 | |
| 6 | Top | -0.489 | -0.04 | -0.048 | |
| 1 | Bottom | -0.503 | 0.022 | 0.025 | |
| 2 | Bottom | -0.492 | 0.014 | 0.017 | |
| 3 | Bottom | -0.473 | 0.033 | 0.04 | |
| 4 | Bottom | -0.454 | 0.043 | 0.055 | |
| 5 | Bottom | -0.512 | 0.064 | 0.078 | |
| 6 | Bottom | -0.487 | 0.028 | 0.032 | |

Note – The magnetic bearings have a double plane pole construction hence each bearing has 6 poles in two planes. Top and bottom configurations are assigned according to their corresponding plane location in the complete vertical assembly.

### 3.9 Wiring scheme

A well-organized wiring scheme is employed to make intermediate connections between the bearings and to the external power amplifier leads. Figure 3-39 shows the arrangement employed.

For each pole of the magnetic bearings, the negative terminal from the pole in the top plane is connected to the positive terminal of the corresponding pole in the bottom plane i.e. the negative terminal of 4- from the top plane in a bearing is connected to the 4+ in the bottom plane of the same bearing to form one complete loop. Table 3-11 summarizes the pole - power amplifier – choke box connections on the actual test rig.

Table 3-11 External wire connections between the bearings, power amplifier and decoupling choke box as per Figure 3-39

| **Top Radial Bearing** | | | |
|---|---|---|---|
| Top Plane (+) | Bottom Plane (-) | Power Amplifier (+) | Decoupling Choke (+) |
| Pole --> Wire No. | Pole --> Wire No. | Wire No. | Wire No. |
| +1 --> 20 | -1 --> 15 | 20 | 15 |
| +2 --> 6 | -2 --> 4 | 6 | 4 |
| +3 --> 7 | -3 --> 3 | 7 | 3 |
| +4 --> 17 | -4 --> 5 | 17 | 5 |
| +5 --> 13 | -5 --> 8 | 13 | 8 |
| +6 --> 12 | -6 --> 23 | 12 | 23 |
| **Bottom Radial Bearing** | | | |
| +1 --> 1 | -1 --> 22 | 1 | 22 |
| +2 --> 10 | -2 --> 19 | 19 | 10 |
| +3 --> 9 | -3 --> 2 | 9 | 2 |
| +4 --> 24 | -4 --> 11 | 24 | 11 |
| +5 --> 21 | -5 --> 16 | 21 | 16 |
| +6 --> 18 | -6 --> 14 | 18 | 14 |

Reversed Polarity

Note – The numeric values from 1 to 24 represent the external 16 gauge wires used for making the external connections between the bearing coils and its electronics. The wires are numbered arbitrarily.

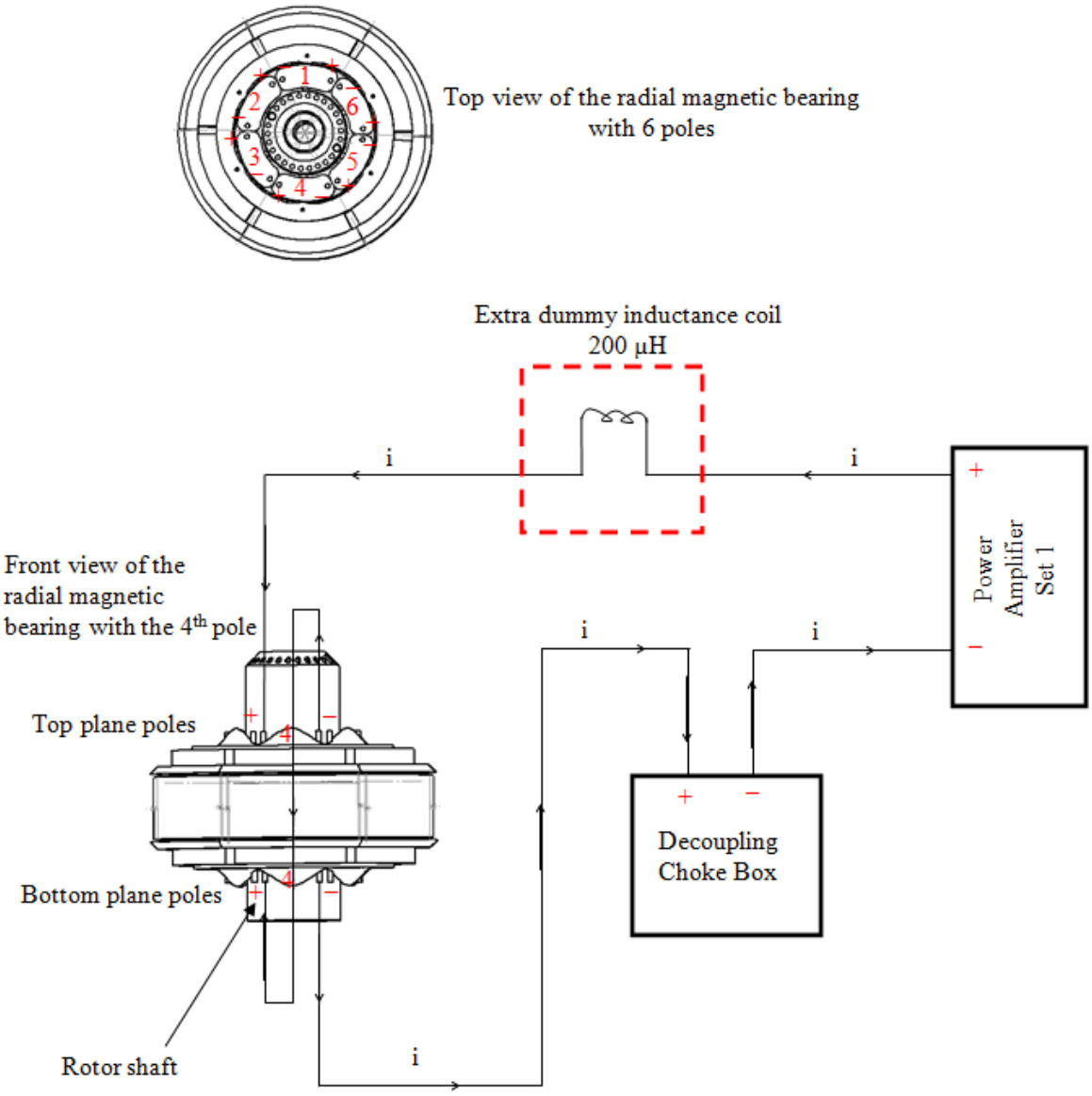


Figure 3-39 Wiring scheme employed to make the interconnections and external wire connections of the radial magnetic bearings

## 3.10 Grounding

The complete test rig assembly and the chassis holding the different electronic components have been grounded to increase the factor of safety. The shorting of any

bearing coil with the metal rig or leakage of current from any electrical component would cause the resulting current to flow to ground thus preventing any electrical hazard.

# 4. ASSEMBLY OF THE COMPLETE MAGNETIC BEARING SYSTEM

The solid model diagram of the complete system is shown in Figure 4-1.

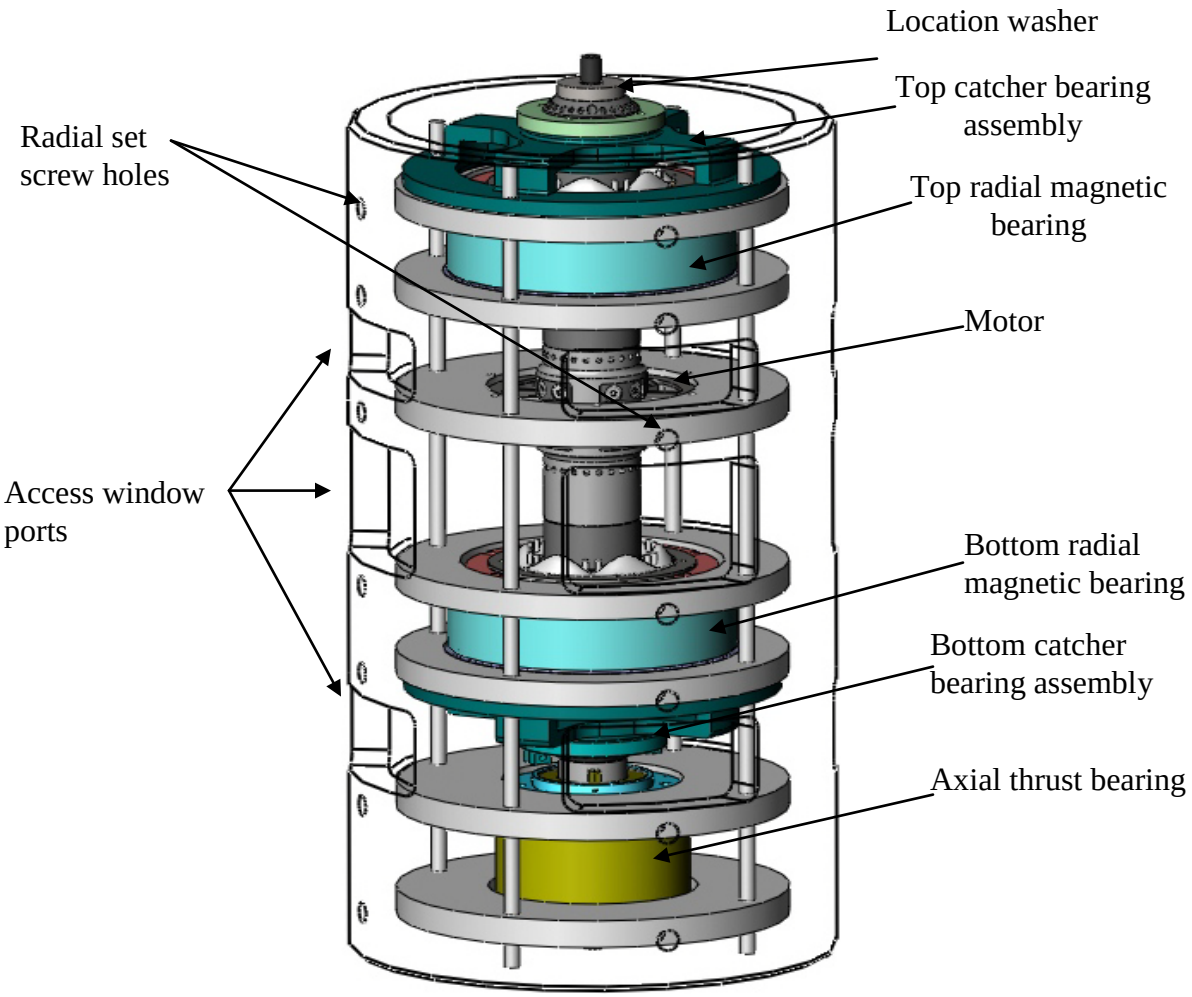


Figure 4-1 Complete assembled universal magnetic bearing system

All the individual components (axial thrust bearing, bottom radial bearing, motor and top radial bearing) were assembled to form the complete system. The complete assembly of all the components was done with a cross sectional view (Figure 4-2) in mind. The assembly of all the components had to be visualized beforehand and foresee any problems due to the delicacy of the wires and prevent disassembly of the assembled parts. The following sections summarize the approach and also the fixtures which were designed to enable the assembly process are shown.

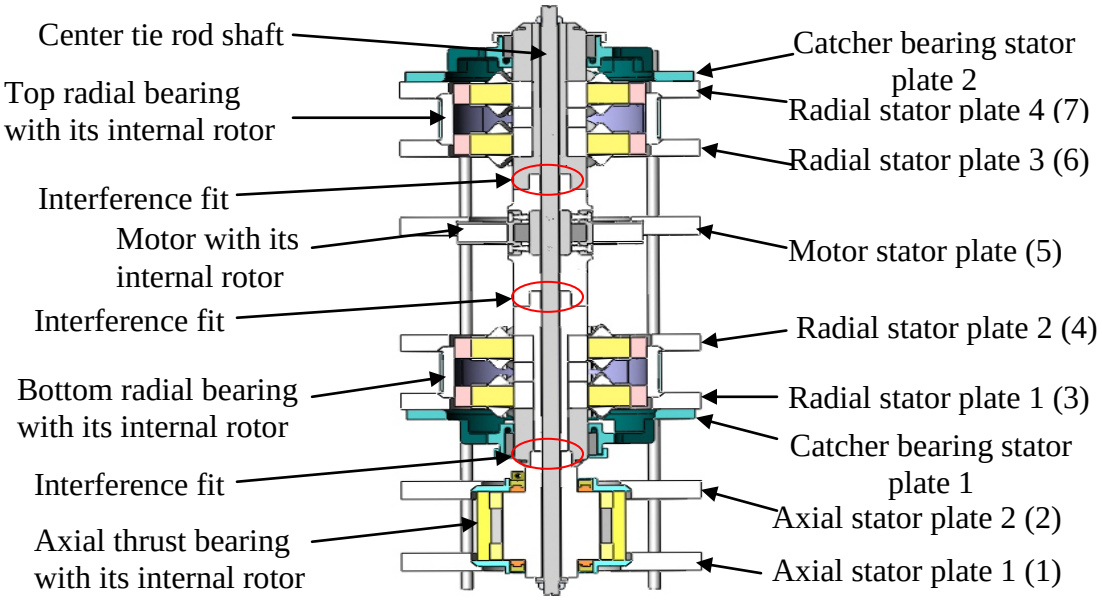


Figure 4-2 Sectional view of the complete system

## 4.1 Axial thrust bearing

The axial thrust bearing was inserted into the cylinder housing as per the mock practice steps which were done using the crane without the actual bearing to simulate any

difficulties. Figure 4-3, Figure 4-4 and Figure 4-5 show the actual axial thrust bearing insertion task.

Figure 4-3 Specially designed and fabricated fixture for handling the thrust bearing

(a) (b)

Figure 4-4 Axial thrust bearing being lifted and inserted within the big cylinder

(c)

(d)

(e)

Figure 4-4 Continued

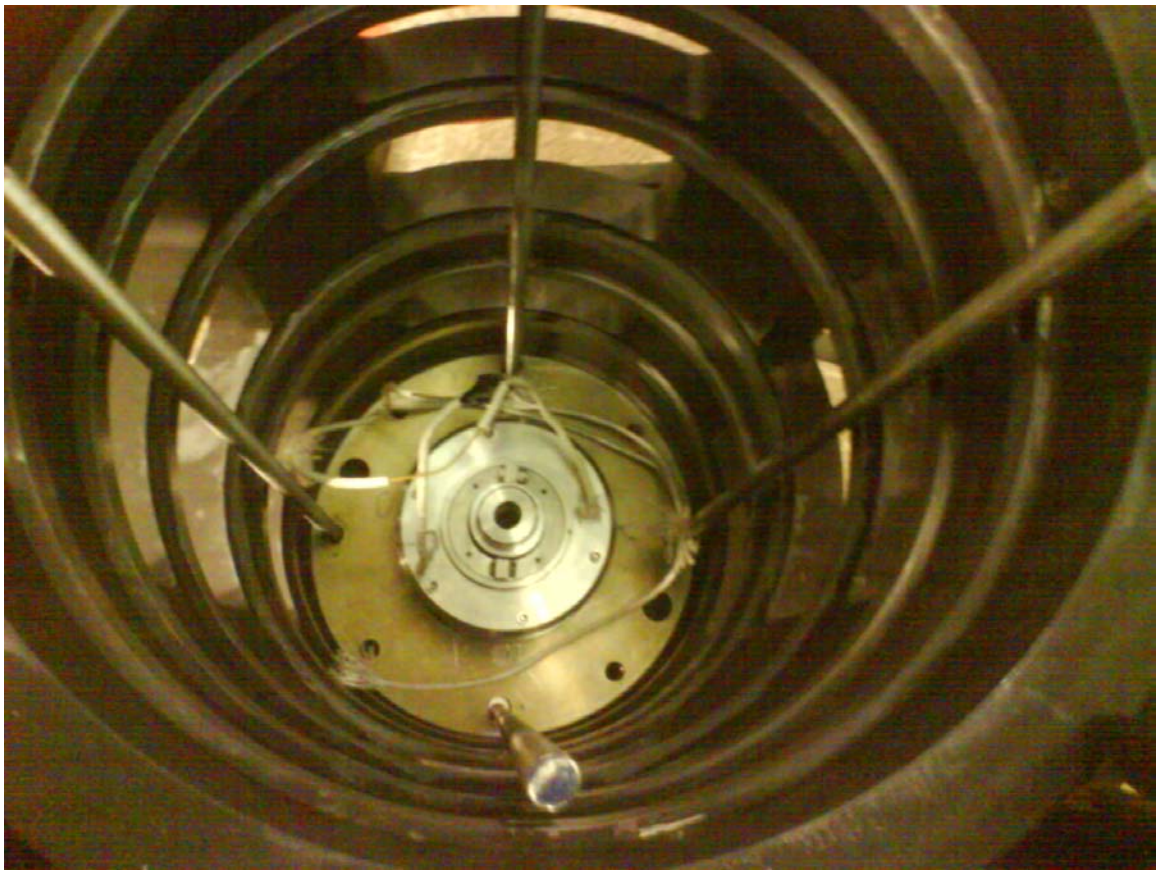

Figure 4-5 Top view of the assembled axial thrust bearing within the big cylinder

## 4.2 Catcher bearing

Catcher Bearings are often co-aligned with the magnetic bearings to assist under startup conditions or as a backup under electrical failure or severe disturbance conditions. During the normal operation of a rotor/magnetic bearing systems, contacts with auxiliary bearings or bushes are avoided. However, auxiliary bearings are required under abnormal conditions and in malfunction situations to prevent contact between the rotor and stator laminations. The backup bearings, for the present research, are made of graphalloy (a solid lubricant suitable for high temperature applications). This choice of bearing material

is made due to the high temperatures which the system will be run at. Figure 4-6 shows the solid assembly of the graphalloy piece and the exploded view of the complete catcher bearing assembly is shown in Figure 4-7. The two female part shells are tapered on the inside to compensate for the wear of the graphalloy i.e. with use as the graphalloy wears out, it will be pushed in more to decrease the increased clearance. The female part washer is provided to enable easy disassembly of the complete catcher bearing since the holes in the stator plate see this washer and push on it to force out the graphalloy piece. The graphalloy single piece is designed to have interference fit at room temperature facilitating its assembly into the catcher bearing stator plate only at high temperatures. Figure 4-8 shows the assembled catcher bearing housing ready to be used on the actual test rig. Detailed drawings for manufacturing can be found in the appendix.

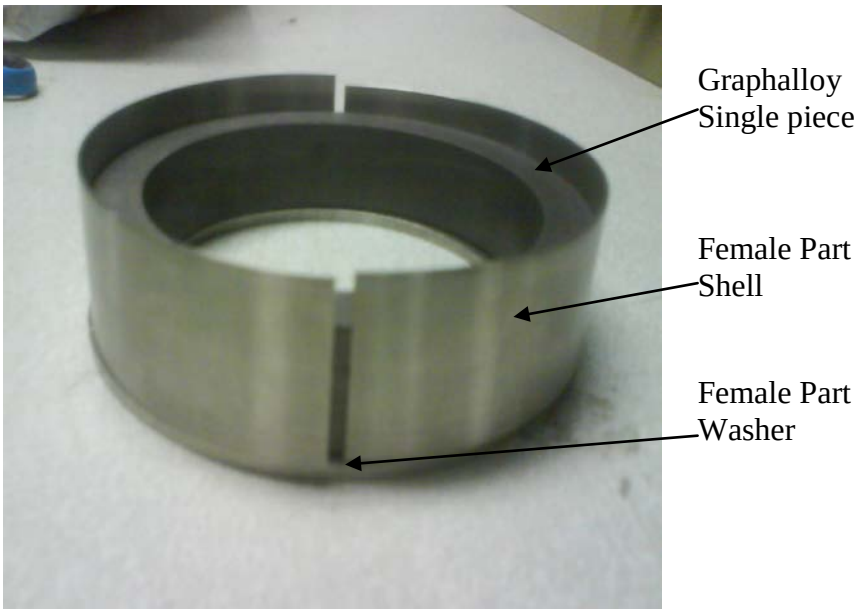


Figure 4-6 Graphalloy catcher bearing assembly

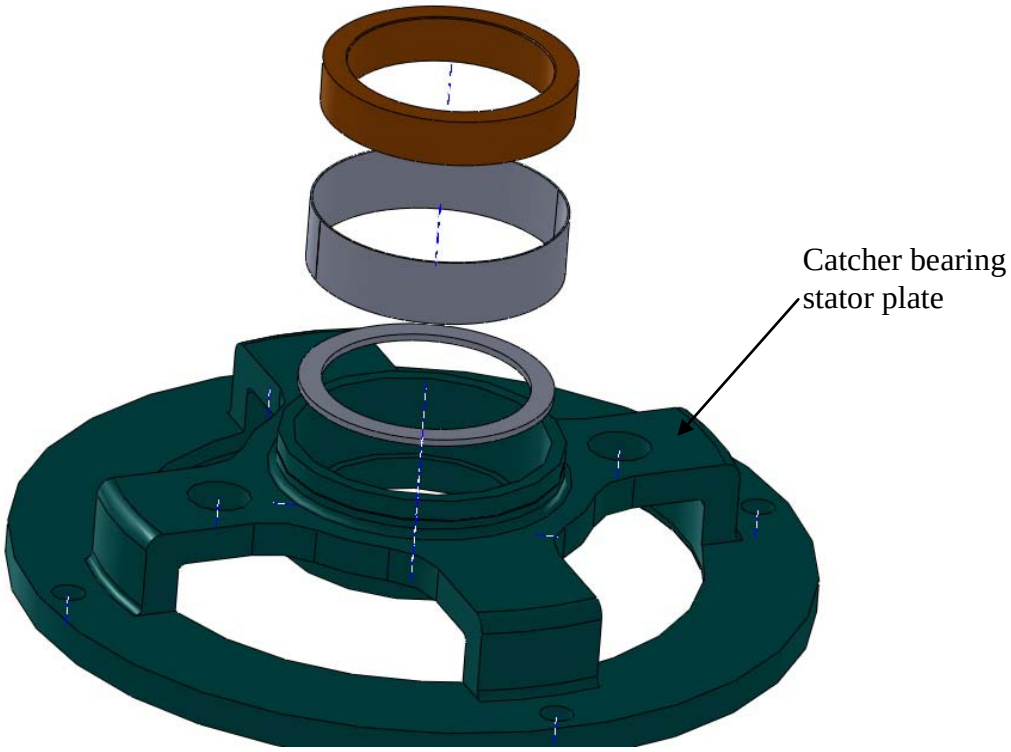


Figure 4-7 Exploded view of the complete catcher bearing assembly

Figure 4-8 Graphalloy shrink-fitted within the catcher bearing stator plate

### 4.2.1 *Evaluation of properties of Graphalloy at room and high temperature*

Due to the unavailability of the Graphalloy properties at room and high temperatures, an experimental procedure had to be devised for evaluation of the Coefficient of Friction and Young's Modulus at room and high temperatures (1000F in our case). These material properties are required for simulation of the entire system in Matlab to test for its stability. Figure 4-9 & Figure 4-10 summarize the experimental procedure. A detailed report on the same can be found in [21].


(a) (b)

Figure 4-9 Experimental setup to measure the coefficient of friction at room temperature and high temperature


(a) (b)

Figure 4-10 Experimental setup to measure Young's Modulus at room and high temperature

## 4.3 Bottom radial bearing

The bottom radial bearing was picked up using the practiced method (which was done without the actual bearing). The bottom radial bearing was picked up and placed onto the bottom plate; then the bottom plate with bearing was lifted and assembled in the rig. The "pick and place" process was enabled by a cross type holder to which all thread rods were screwed into. The all threads have bent washers (so that they could fasten against the outside surface of the bearing). Further the all threads were secured tightly using hose clamps which hold/secure the all threads together against the bearing outside surface. Two hose clamps were used (in case one of them failed, the other could be relied upon). The cross has an eye so that it could be lifted using the hook fastened to the

hydraulic lift. Figure 4-11, Figure 4-12 & Figure 4-13 make the above description more clear.

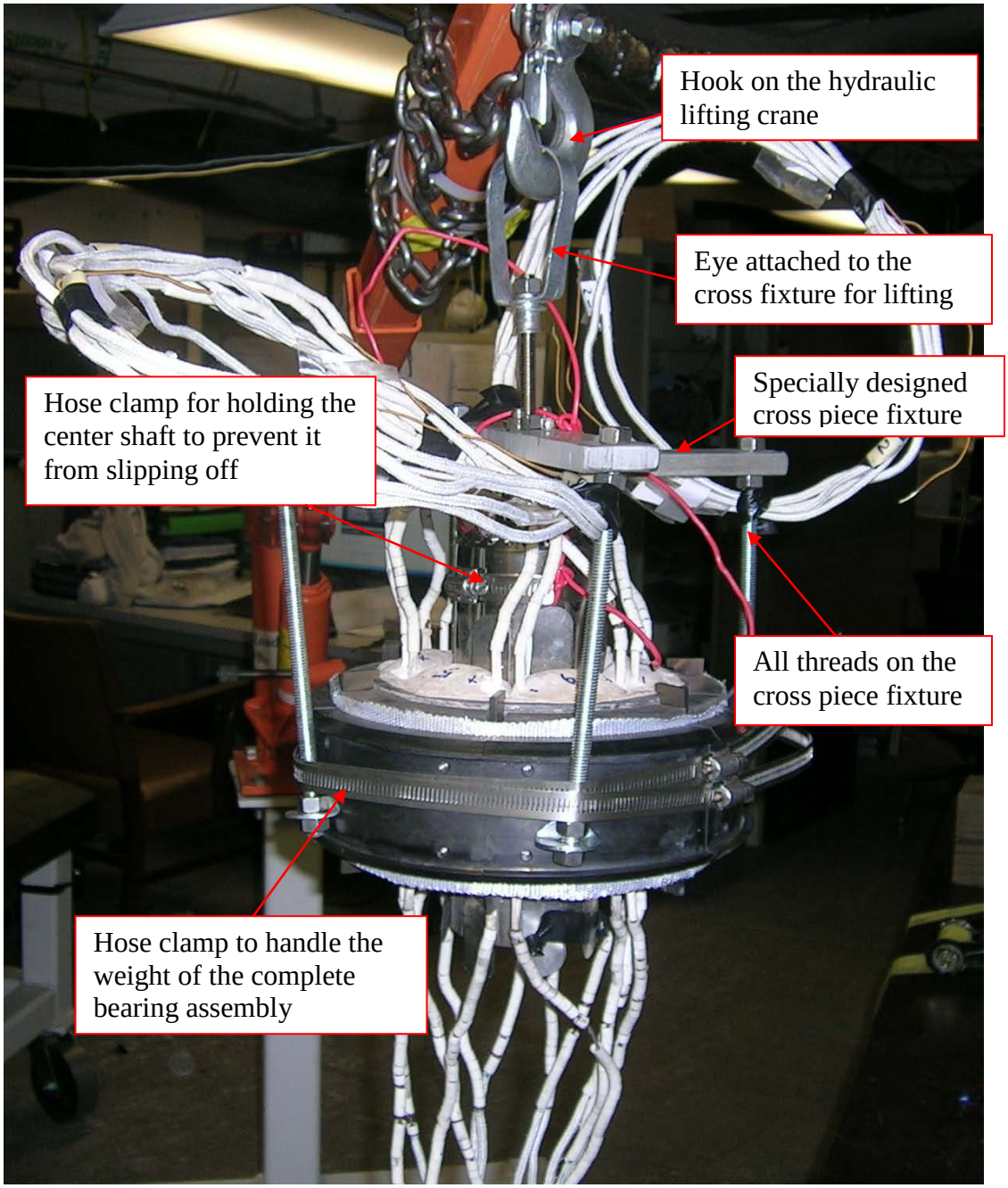


Figure 4-11 Bottom radial bearing lifted and hauled by a specially designed fixture for easy handling

Figure 4-12 Bottom radial bearing being guided on the corresponding stator plate (with the bottom catcher bearing stator plate attached).

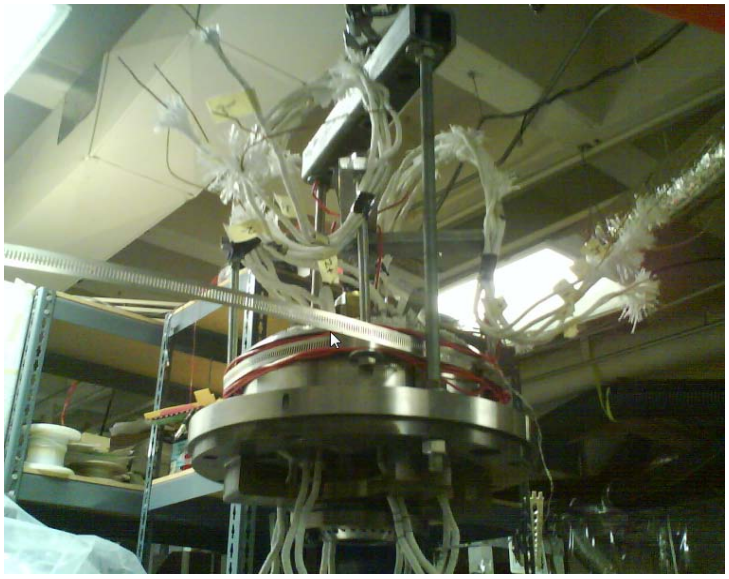

Figure 4-13 Bottom stator plate being lifted (after the bottom radial bearing was “picked and placed” on the bottom catcher bearing)

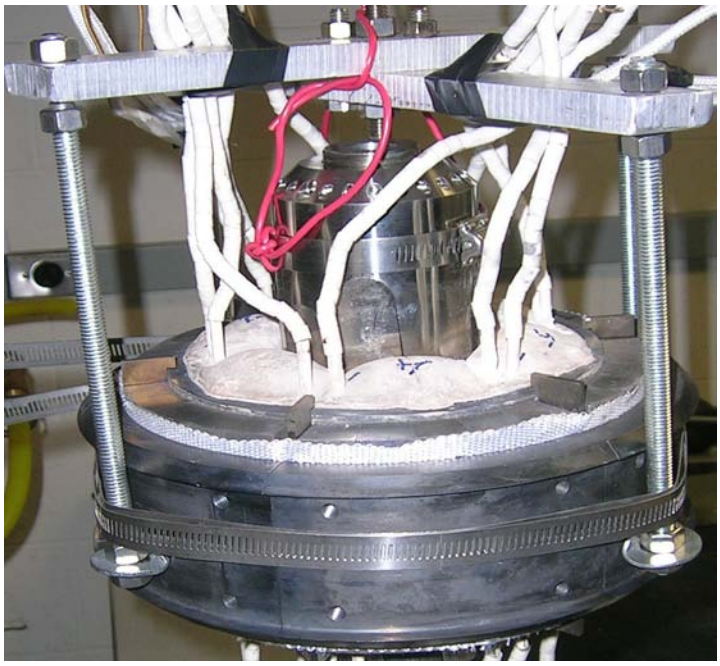

Figure 4-14 Cross piece fixture designed and fabricated for easy handling of the bearing assembly

Moreover the shaft piece inside the bearing was fastened to the cross using the red insulated wire so that the shaft will not slip off in worst case (shown in Figure 4-14). Figure 4-15 shows the top view of the assembled system.

Figure 4-15 Top view of the assembled bottom radial bearing within the cylinder

## 4.4 Motor

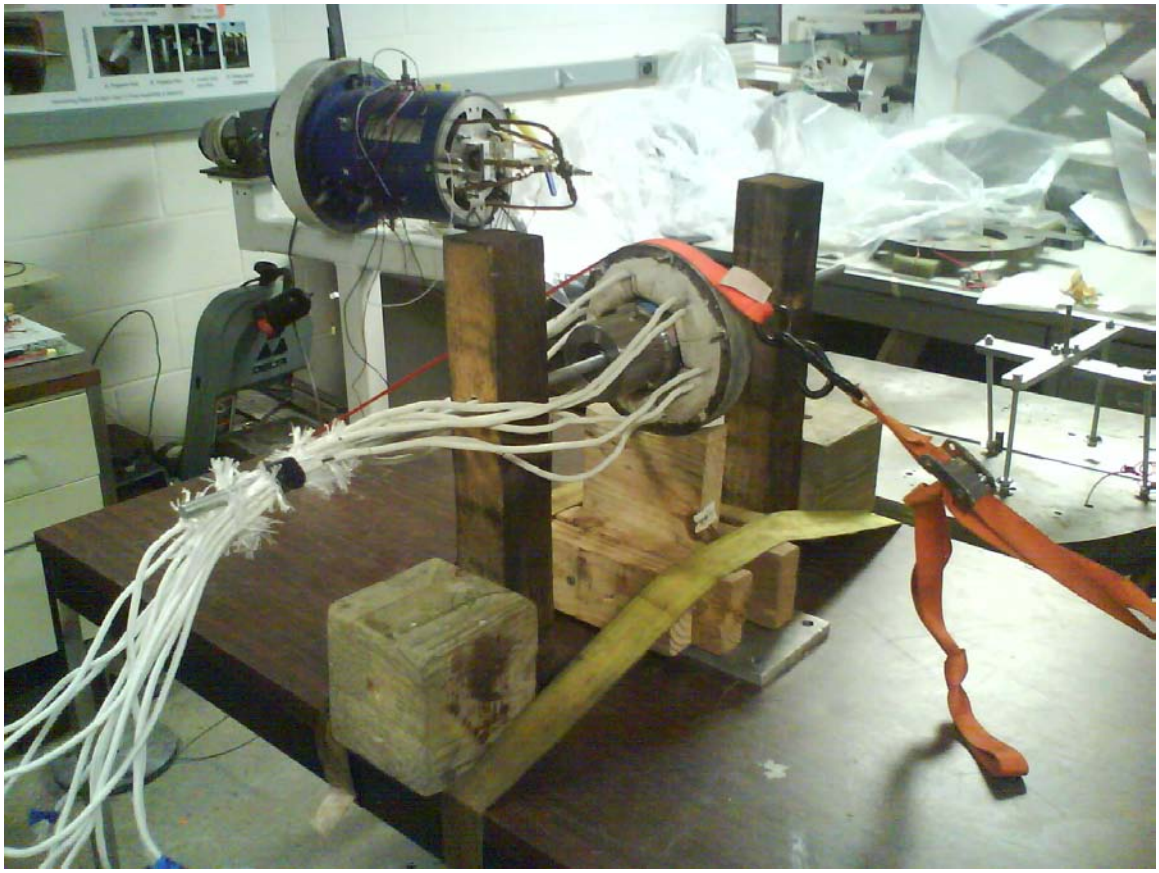

Figure 4-16 EEC motor sans the stator plate held rigidly on a specially designed fixture with the help of straps

The motor has only one plate to be attached as can be seen from the solid model shown in Figure 4-2. The plate was screwed in by using the above setup. The motor with the plate screwed in using double nuts and screw is as shown in Figure 4-16. Figure 4-17, Figure 4-18 & Figure 4-19 show the assembly steps.

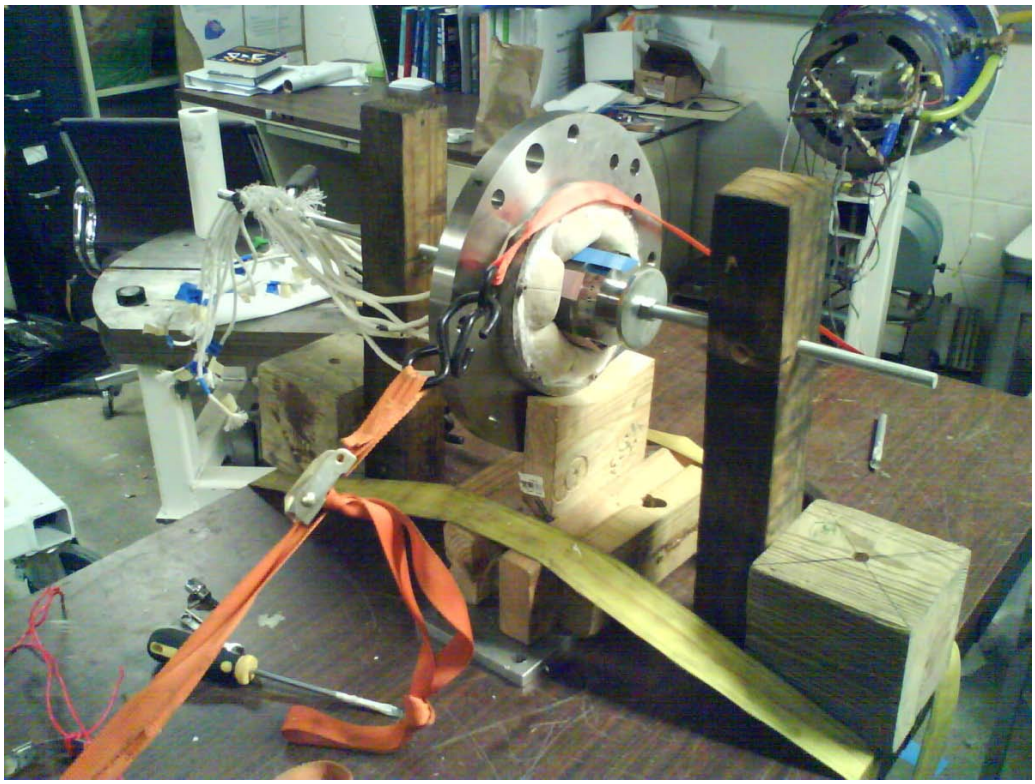

Figure 4-17 EEC motor with its stator plate and rotor shaft

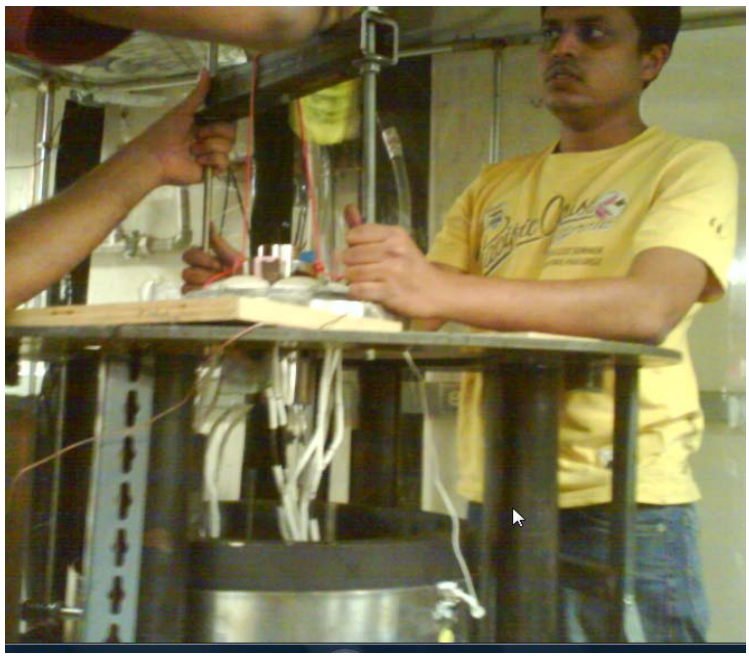

Figure 4-18 EEC motor being guided within the test rig

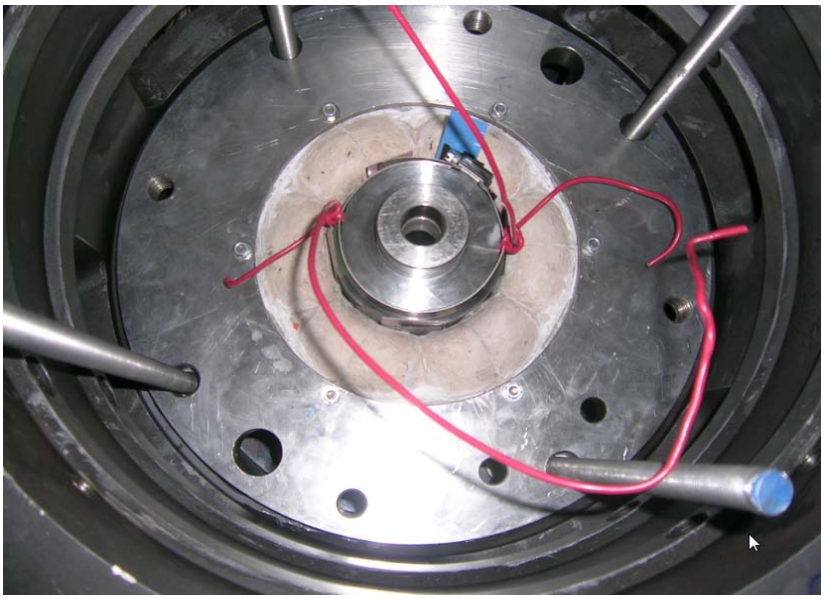

Figure 4-19 Top view of the assembled EEC motor

## 4.5 Top Radial Bearing

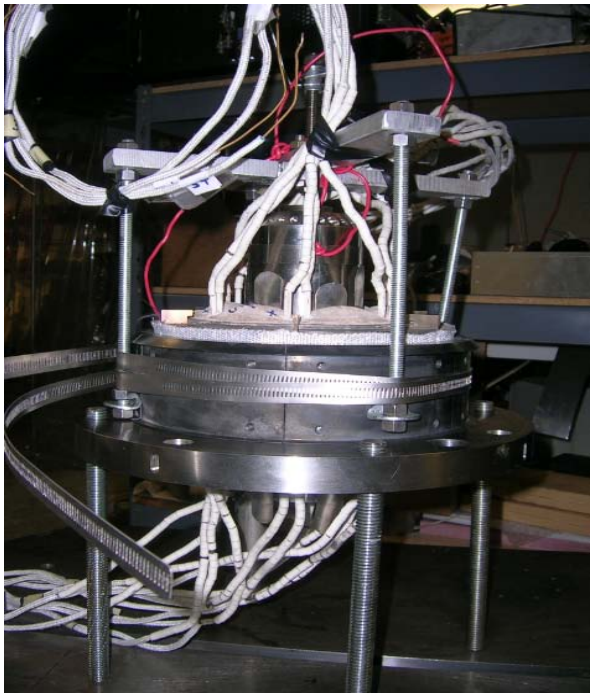

Figure 4-20 Top radial bearing fixture fabricated to withstand its weight and facilitate easy handling

The same assembly process (using cross-all threads-hose clamp) was used to assemble both the motor and top radial bearing. Extreme care was taken in protecting the wires during assembly. Figure 4-20, Figure 4-21 & Figure 4-22 show the assembly procedure.

Figure 4-21 Top radial bearing assembly being lifted and guided with the cross piece fixture

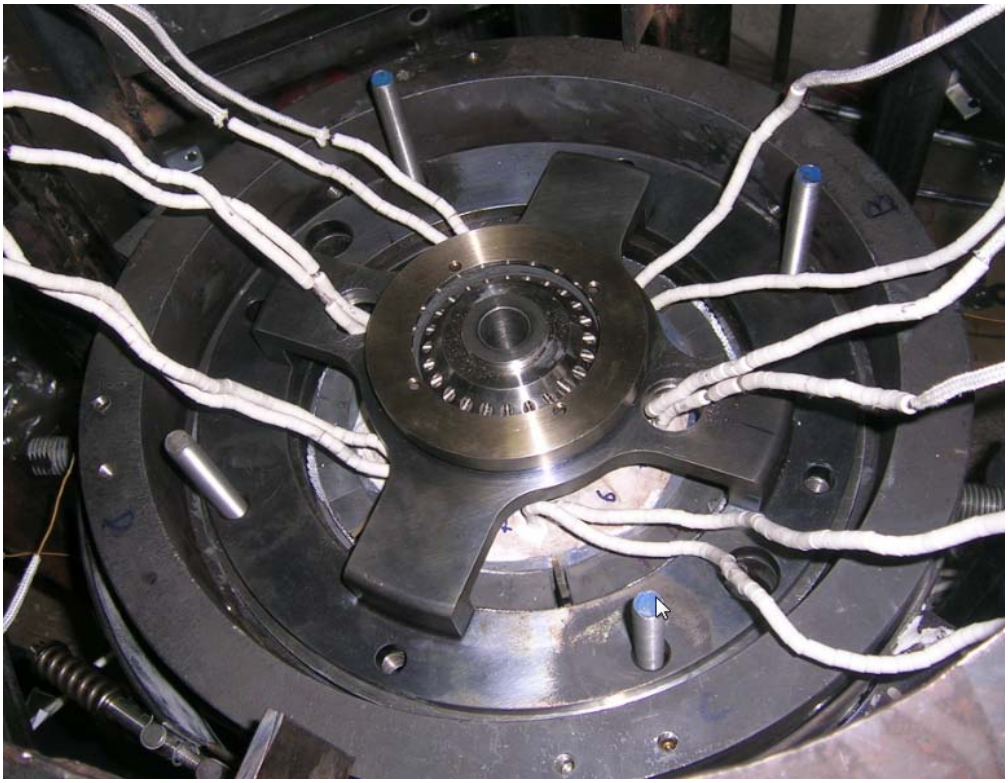

Figure 4-22 Top view of the complete assembled magnetic bearing system

## 4.6 Modifications to the original design

Some modifications were incorporated in the final stages of the assembly to account for the design improvements which were thought during the process. The following changes were made to enable easy assembly, disassembly and improvement of the complete system.

### 4.6.1 *Stator plates*

The seven stator plates which hold the individual components (namely the axial bearing, motor and the two radial bearings) have been reduced on their outside diameter by 40 mils as shown in Figure 4-23. During the earlier run up heating test with only the stator plates conducted by Zhengxin in [16], it was observed the plates expanded and were difficult to take out during their disassembly.

A fixture was designed to measure its radial movement at room temperature (Figure 4-24). The average displacement observed on each plate was around 5 mils. This was increased by 40 mils to provide for greater degree of movement in the radial direction. Table 4-1 shows the readings taken for radial movement of old plates (before reduction) using the arrangement shown in Figure 4-24.

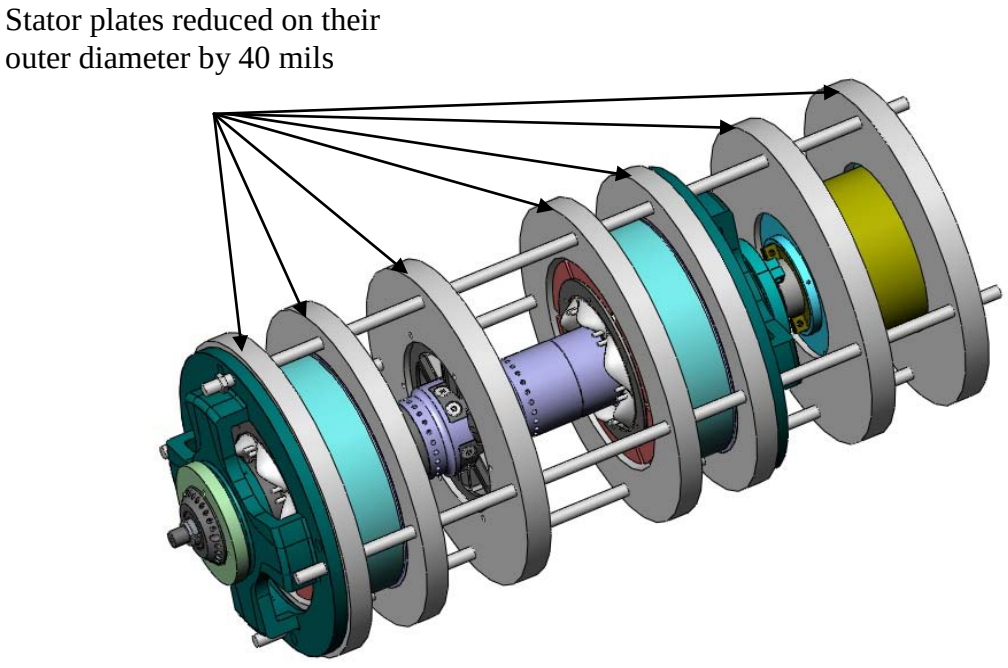


Figure 4-23 Seven stator plates of the EEC magnetic bearing system

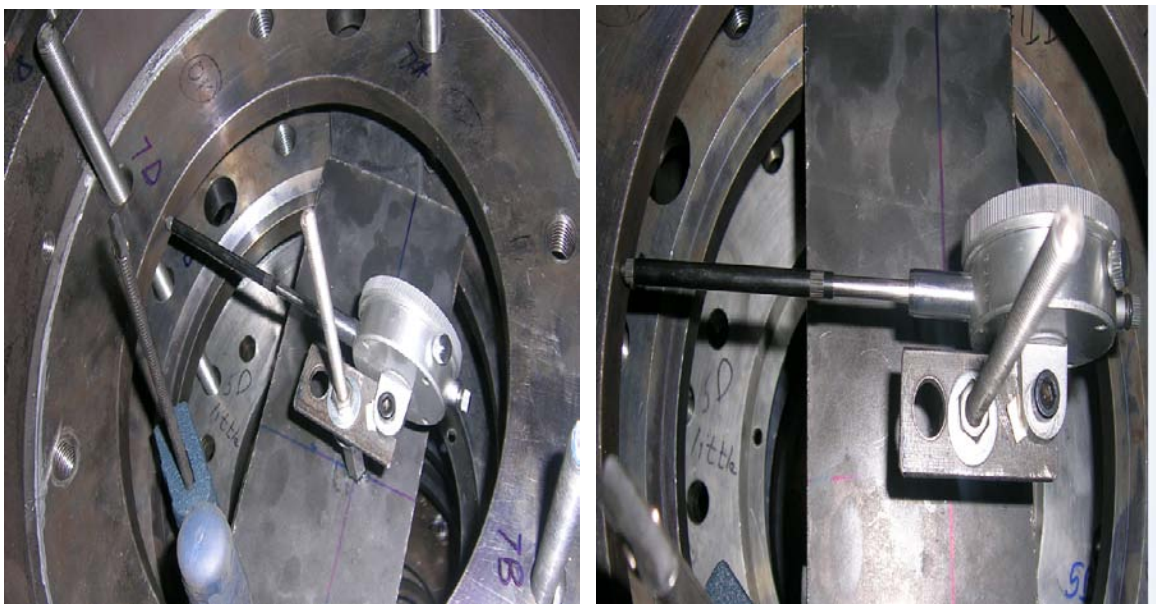

(a) (b)

Figure 4-24 Experimental setup to measure the stator radial displacements

Table 4-1 Maximum recorded radial displacement of the old stator plates

| **Plate No.** | **Max translation in X axis** | **Max translation in Y axis** |
|---|---|---|
| | **mils (0.001 in)** | **mils (0.001 in)** |
| 7 | 5 | 6.5 |
| 6 | 6.5 | 4.5 |
| 5 | 7 | 6.5 |
| 4 | 5.5 | 5 |
| 3 | 11 | 7.5 |
| 2 | 3 | 5 |
| 1 | 3.5 | 5 |
| The 7th plate is the radial stator plate 4 (see Figure 4-2) | | |

### 4.6.2 *Locator plate*

In order to provide more sturdiness to the all threads (which support the stator plates) from the original design, a new locator plate is provided at the very bottom of the cylinder and attached to the cylinder stand. This locator plate, with the 4 holes for the 4 all threads, locates the all threads and maintains their respective position while the complete system is assembled and run as shown in Figure 4-25 & Figure 4-26.

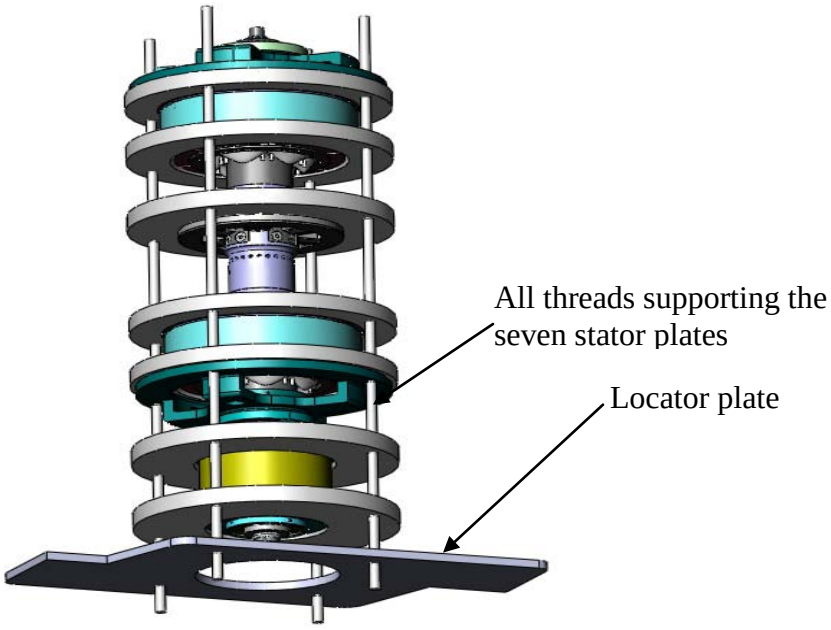


Figure 4-25 EEC test rig with the location of locator plate

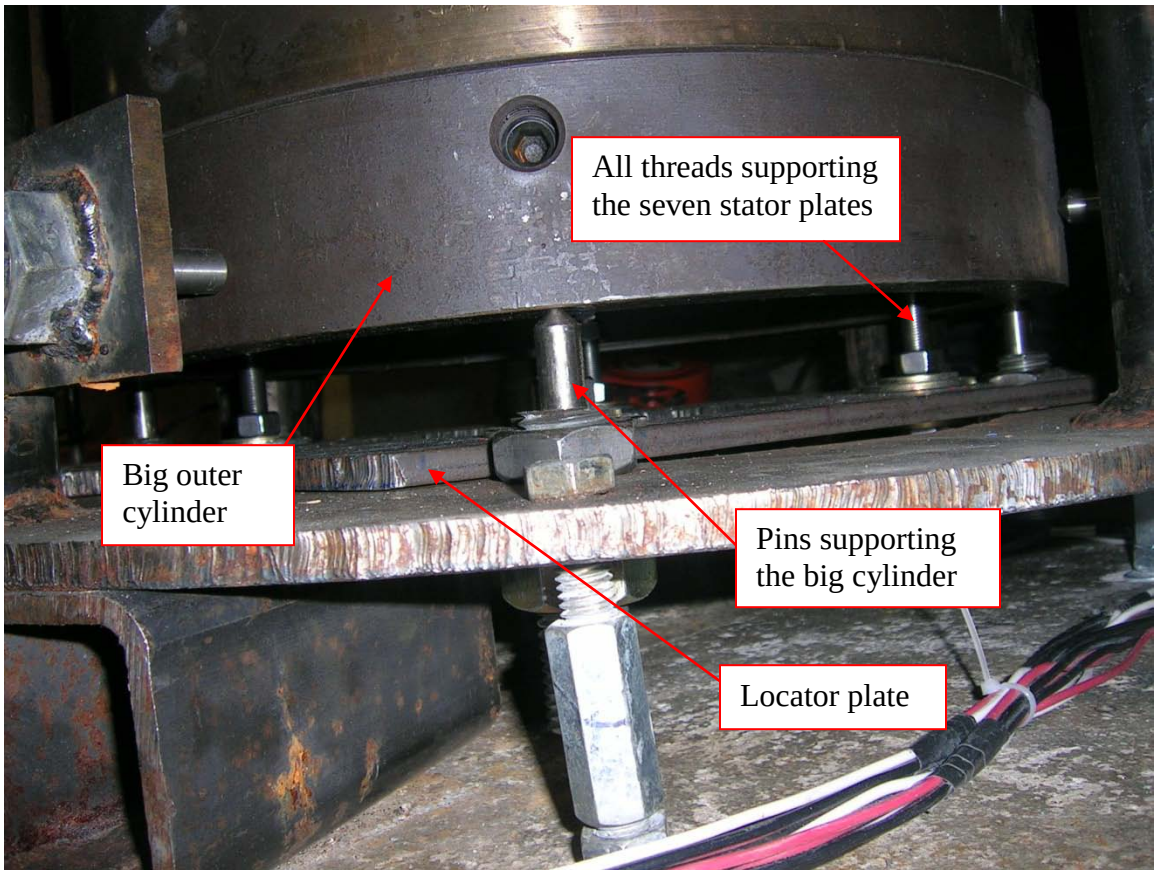


Figure 4-26 Locator plate placed at the bottom of the cylinder

### 4.6.3 *Sensor holder*

The high temperature Kaman sensors, which sense the position of the rotor in the 5 directions of interest, have to be guided to the accessible locations of interest. Also, these sensors require a non-magnetic target for sensing the position and providing an appropriate feedback voltage. For this, 5 sensor holders had to be designed (4 for the radial directions and 1 for the axial direction). The 4 radial sensor holders sense the position of the rotor in the X and Y directions (arbitrarily chosen as per accessibility) at

two locations as shown in the Figure 4-27 & Figure 4-28. Figure 4-29 shows the actual sensor mounting locations on the assembled test rig.

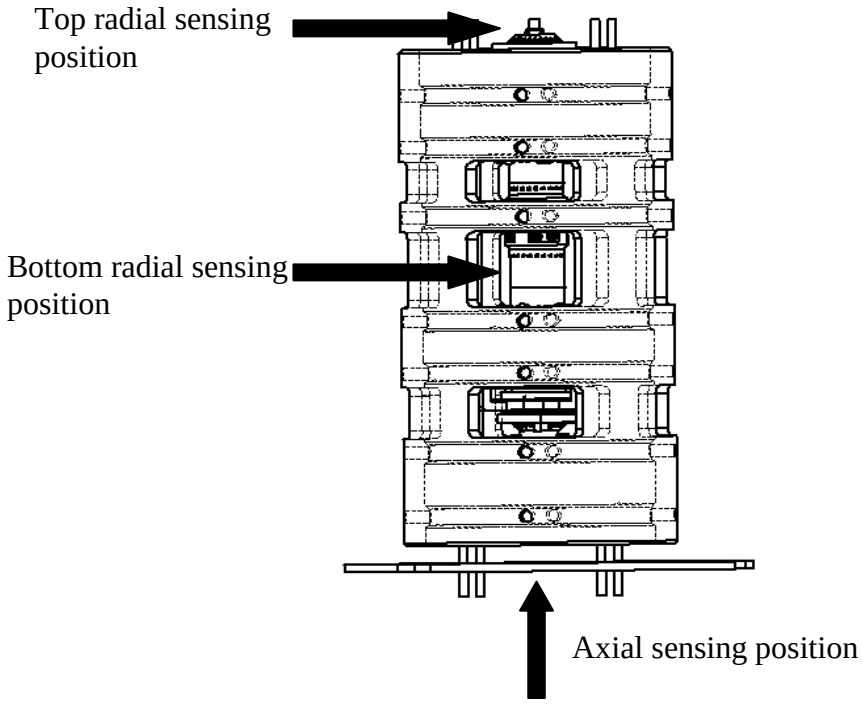


Figure 4-27 Model front view with the actual sensor locations

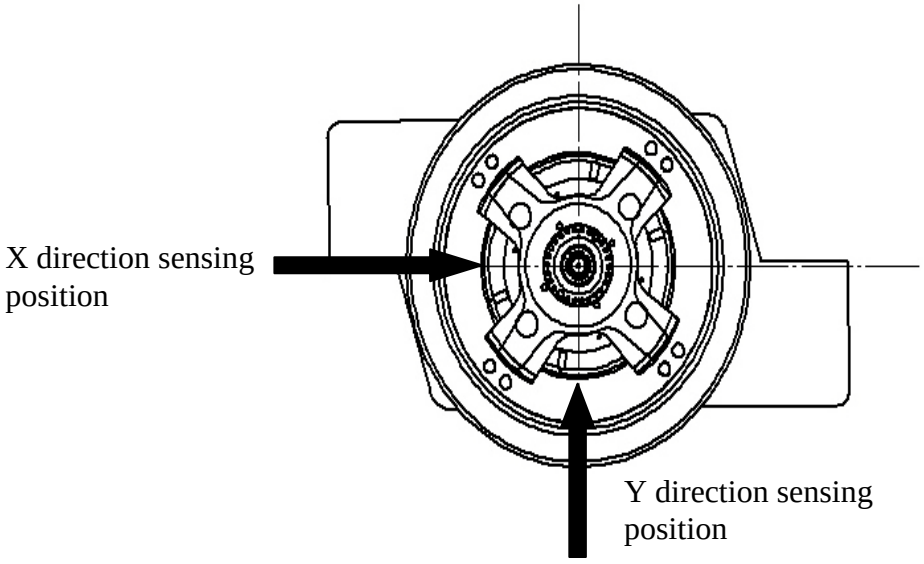


Figure 4-28 Model top view with the sensor locations in the two directions at 90°

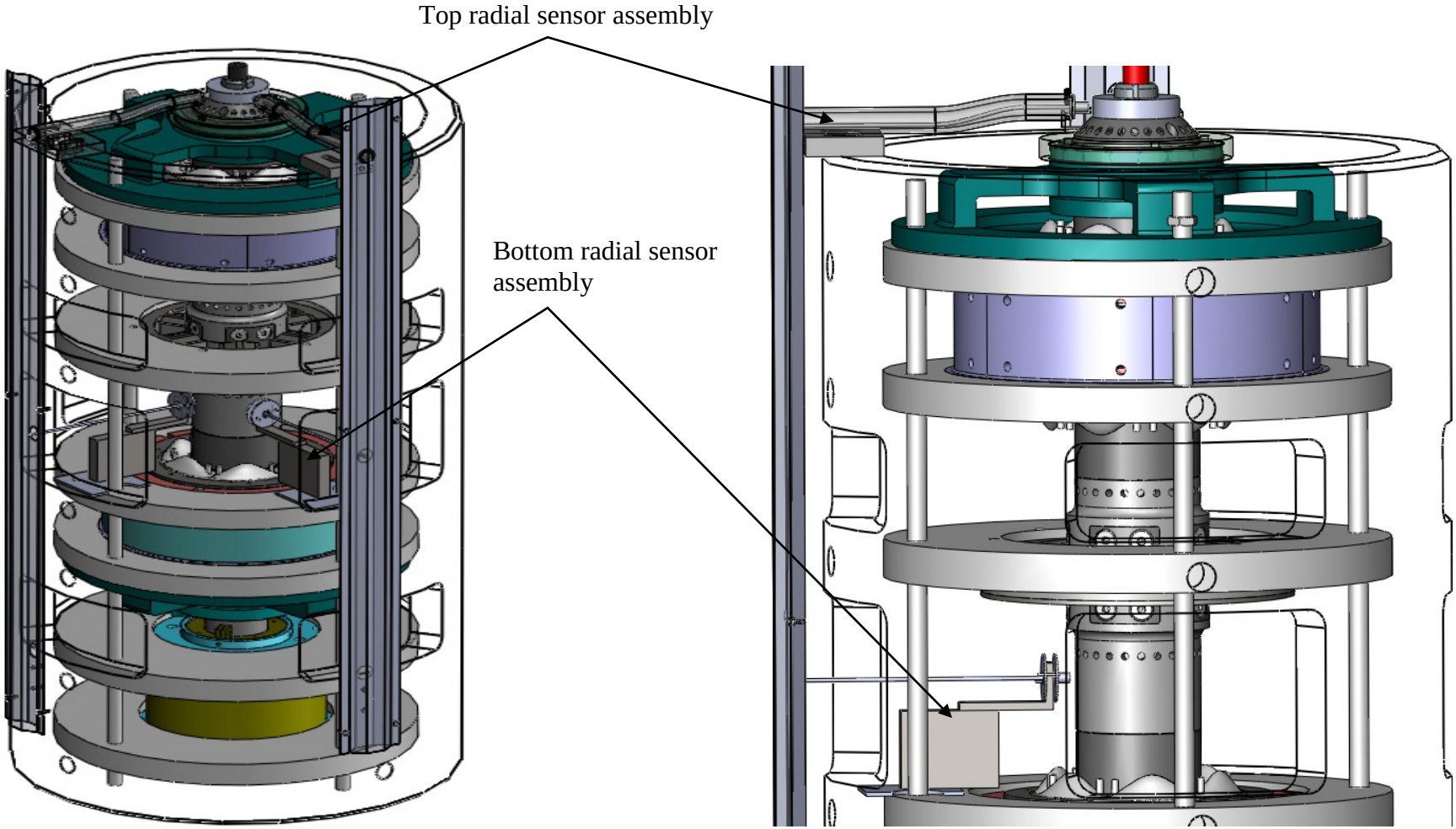


Figure 4-29 Radial sensor holders mounted on the EEC universal test rig system

1) Radial sensor holder

The radial sensor holders are 4 in number and sense the position of the rotor in X and Y direction at two locations. It is primarily a stainless steel tube welded to a square plate with slots for adjustment on the cylinder. These sensor holders guide the Kaman sensors to the accessible locations of interest and provide feedback of the rotor position to the sensor box. The radial sensor holders see part 3 (made of non-magnetic material Inconel 718 (Figure 2-6) and the location washer at the top (made of non-magnetic Stainless Steel). Figure 4-30 & Figure 4-31 show the top radial sensor assembly and bottom radial sensor assembly respectively.

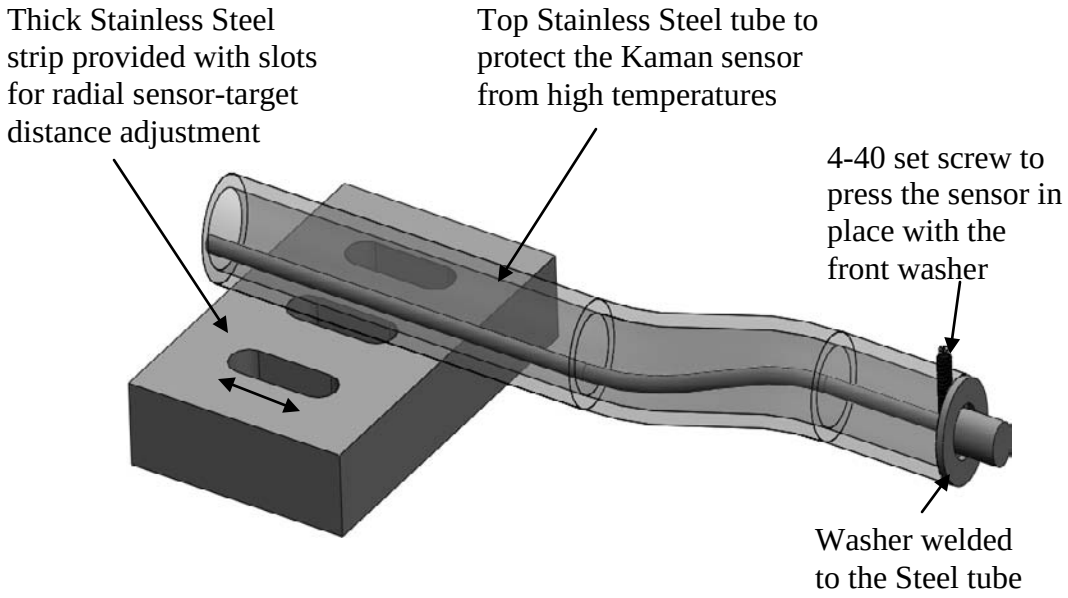


Figure 4-30 Top radial sensor assembly

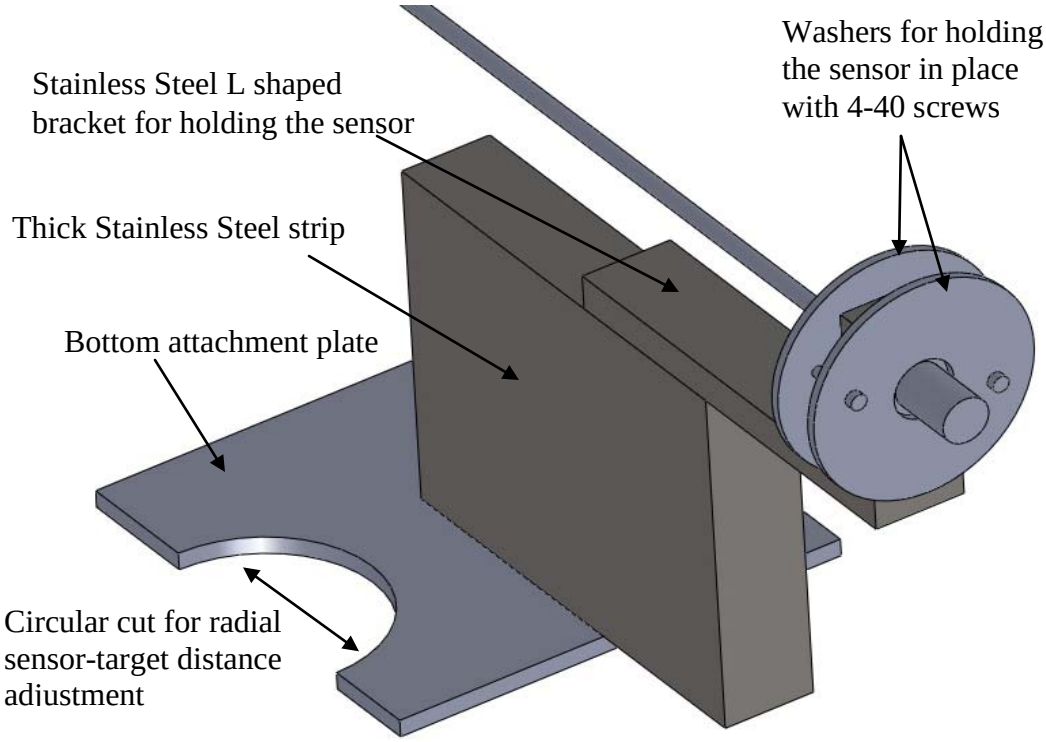


Figure 4-31 Bottom radial sensor assembly

2) Axial sensor holder

The axial sensor holder is 1 in number and senses the position of the rotor in the Z direction. It is primarily two U shaped stainless steel strips with provisions for holding the sensor and permits its movement in the Z direction towards or away from the rotor shaft as shown in Figure 4-32. The axial sensor sees the center tie rod (made of non-magnetic material Inconel 718) at the bottom for sensing the position as shown in Figure 4-33.

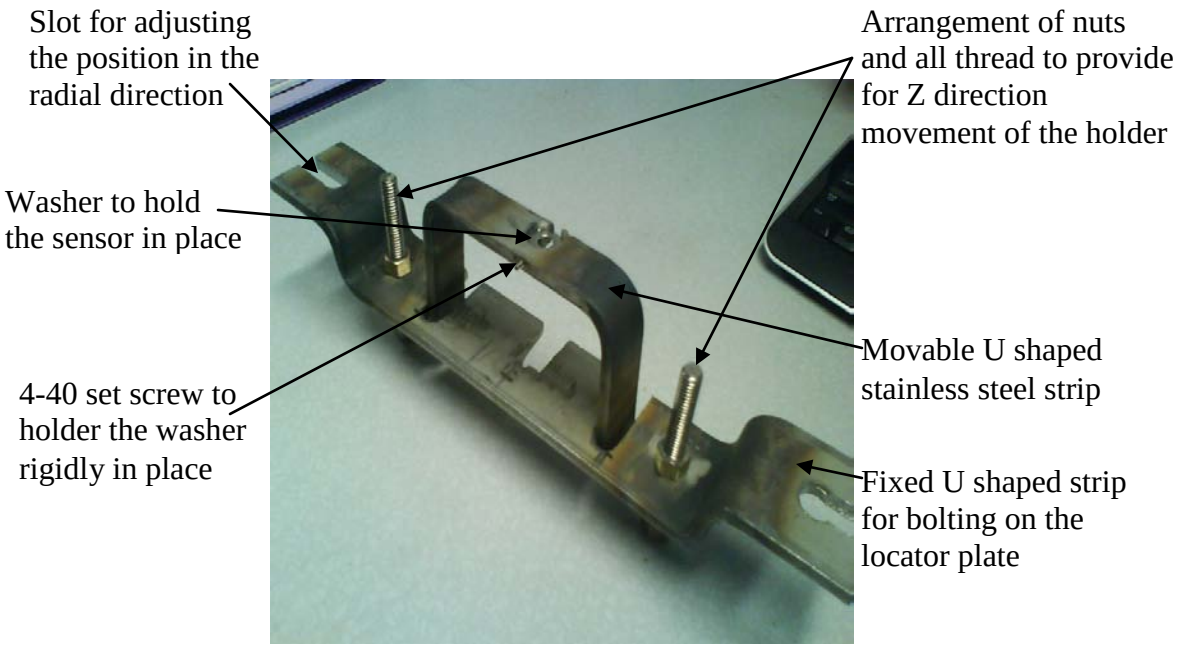


Figure 4-32 Axial sensor holder assembly

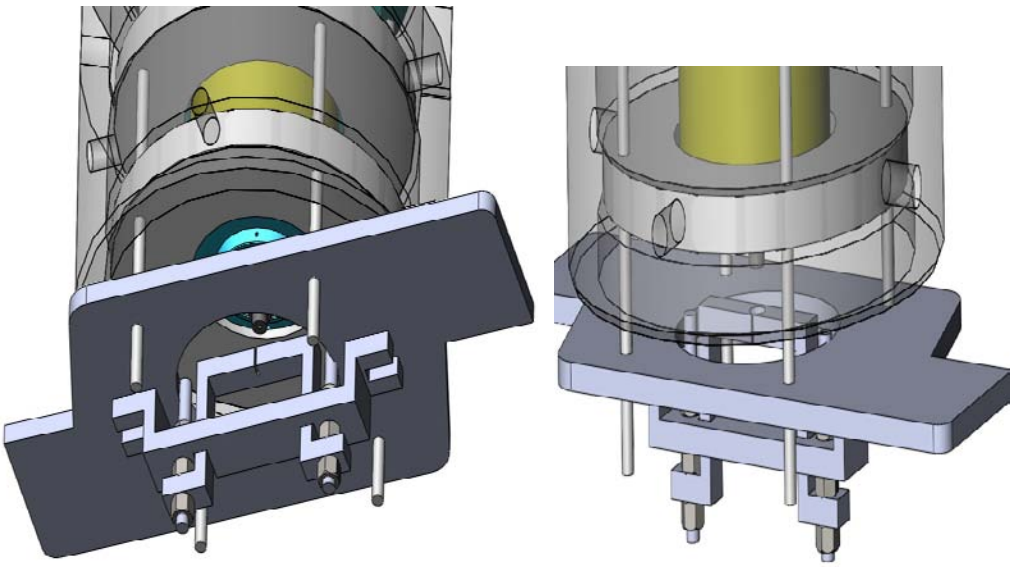

(a) (b)

Figure 4-33 Axial sensor holder mounted on the locator plate beneath the cylinder assembly

### 4.6.4 *Location washers*

After the radial sensor holders were designed, a need for a target washer was felt which the top radial sensor holder could see in order to detect shaft movement at the top. In addition to the target, a part had also to be designed to locate the tie rod (which holds all the shaft pieces together) in the geometric center of the cylindrical shaft since any eccentricity in its location would cause the sensors to feedback wrong information on the shaft position. Keeping the above needs in mind, two identical washers were designed (one for top which would also act as the sensor target and one for the bottom as shown in Figure 4-35). Figure 4-34 shows the designed and fabricated part made of stainless steel (non-magnetic). Detailed drawings for manufacturing can be found in the appendix.

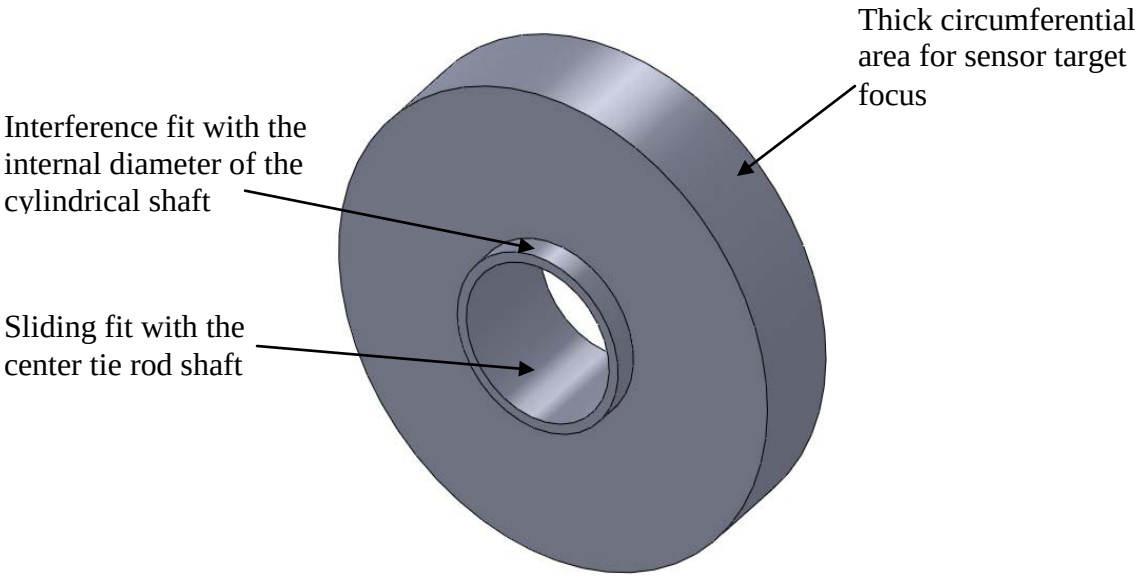


Figure 4-34 Location washer

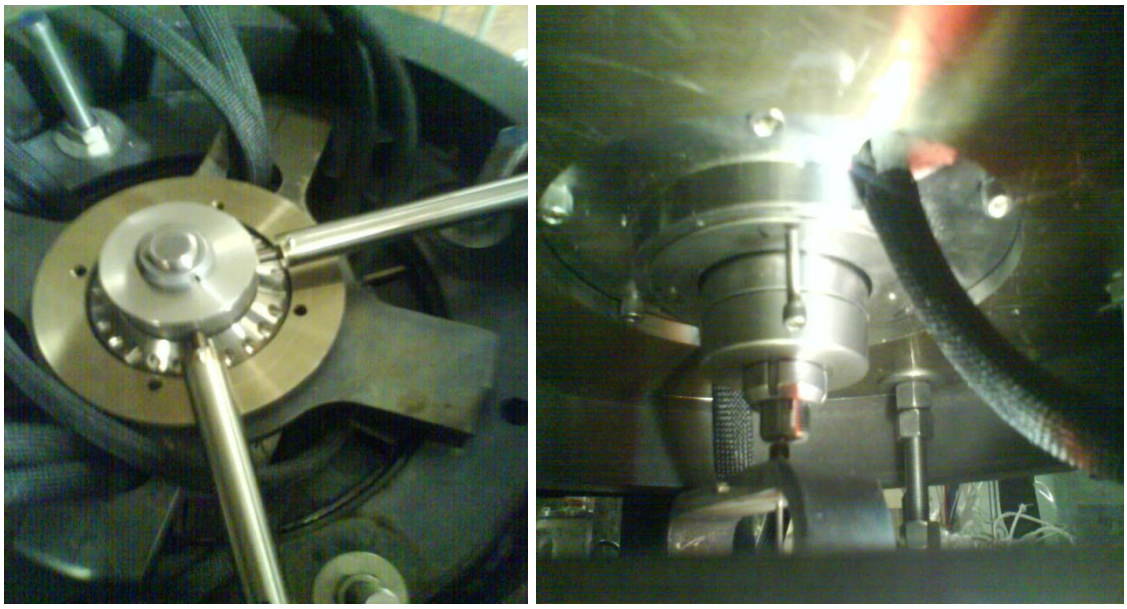

(a) Top location washer (b) Bottom location washer

Figure 4-35 Top and bottom location washers

### 4.6.5 *Holes on catcher bearing stator plates*

In order to prevent the contact of the wires coming out from the poles of the magnetic bearing with the catcher bearing stator plate and result in an electrical hazard, there were some additional holes of 2 inches diameter drilled on both (top and bottom) stator plates to guide them out safely towards external connections and hence prevent any metal contact as shown in Figure 4-36. This diameter value was arbitrarily chosen, keeping the minimization of lost material and just enough space for wires in mind.

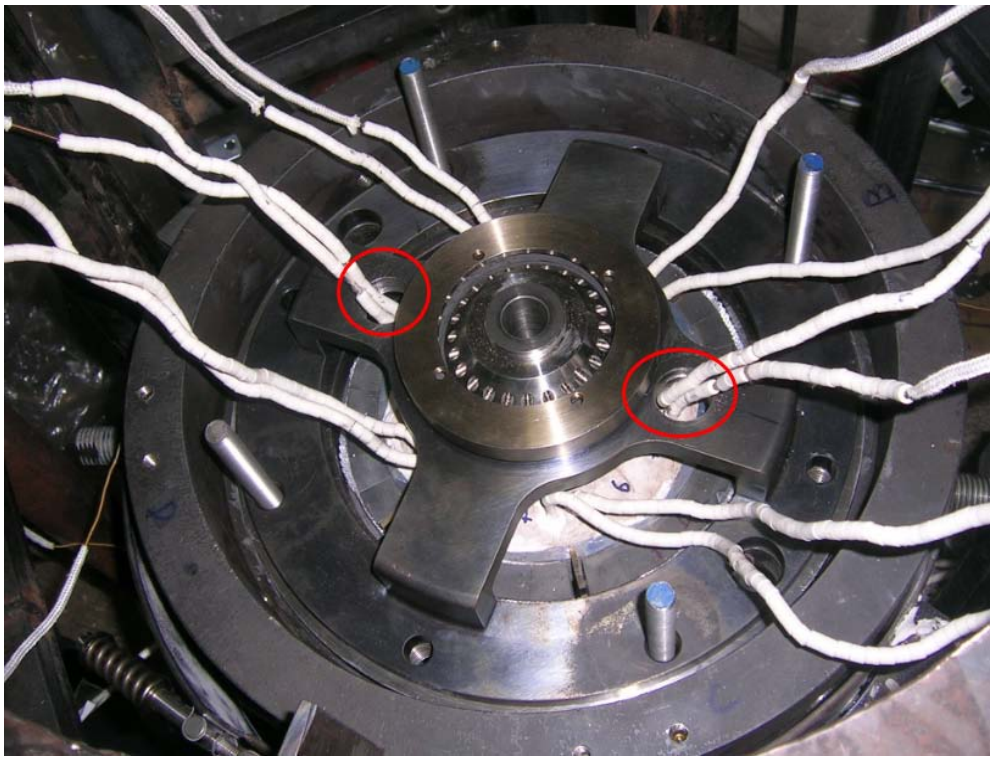

Figure 4-36 Holes on the catcher bearing stator plate for passage of bearing wires

### 4.6.6 *Additional sheathing, external connections and conduits*

The high temperature beads which were provided on the magnetic bearing wires earlier exposed some wire after assembly and thus resulting in an electrical hazard of coming in contact with each other or with any metal surface. Thus to prevent any accident and increase the safety, an additional high temperature fiber glass sheath was provided for the same on each of the 64 wires as shown in Figure 4-37.

(a)

(b) (c)

Figure 4-37 High temperature sheathing provided on each wire to increase electrical safety

An organized system of connection is provided for external connections towards the power amplifiers. High temperature terminal blocks are used as intermediate connections between the magnetic bearing wires and the power amplifiers. The Zircar insulating pads are used for mounting all these external connections as shown in Figure 4-38.

Figure 4-38 High temperature terminal blocks mounted on Zircar insulation pads

These wires from the magnetic bearings are enclosed in stainless steel conduits in order to increase the level of safety and protect them against high surrounding test rig temperatures of the order of 1000F as shown in Figure 4-39.

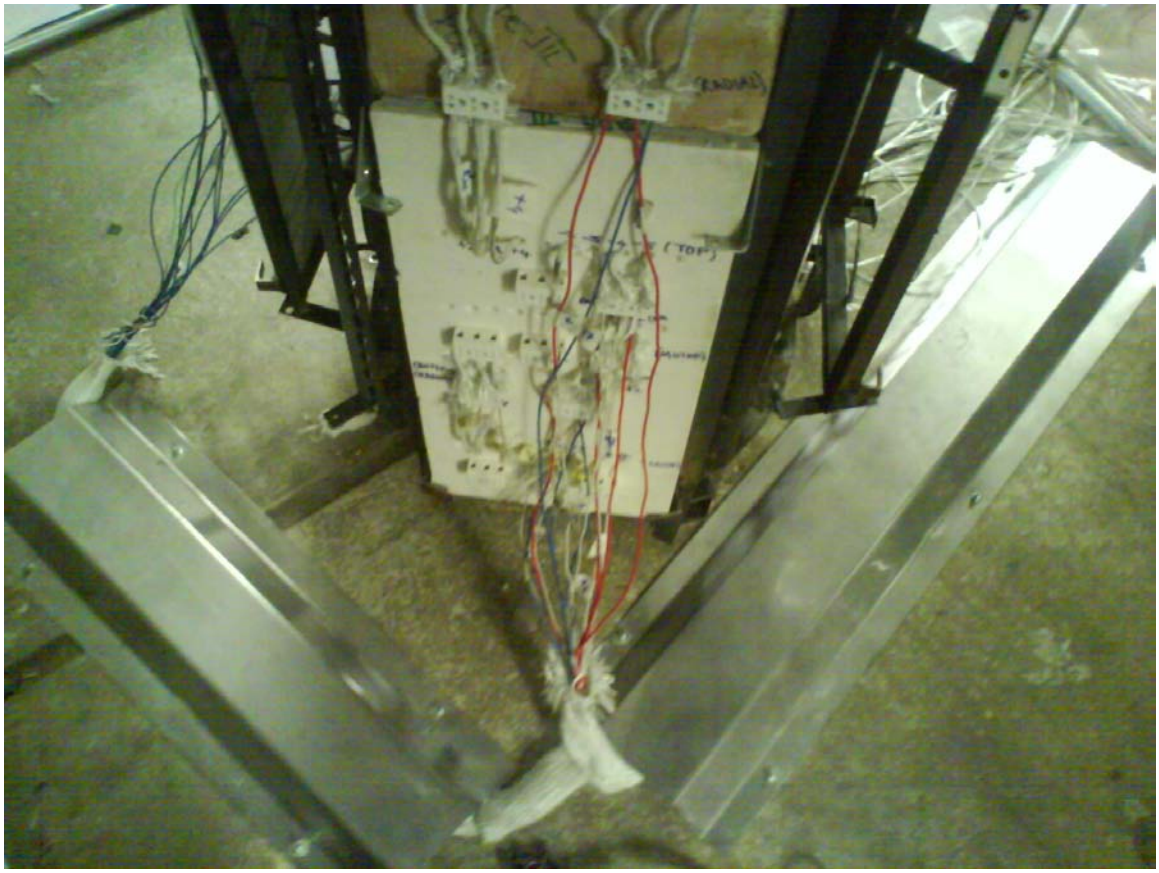

Figure 4-39 External wire connections to the controller enclosed in Stainless Steel conduits to protect against high temperature surroundings

# 5. SIMULATION

## 5.1 Modeling of the EEC test rig system

### 5.1.1 *Finite element formulation*

A 3-D beam-type element, shown in Figure 5-1, is used to construct the finite element shaft model.

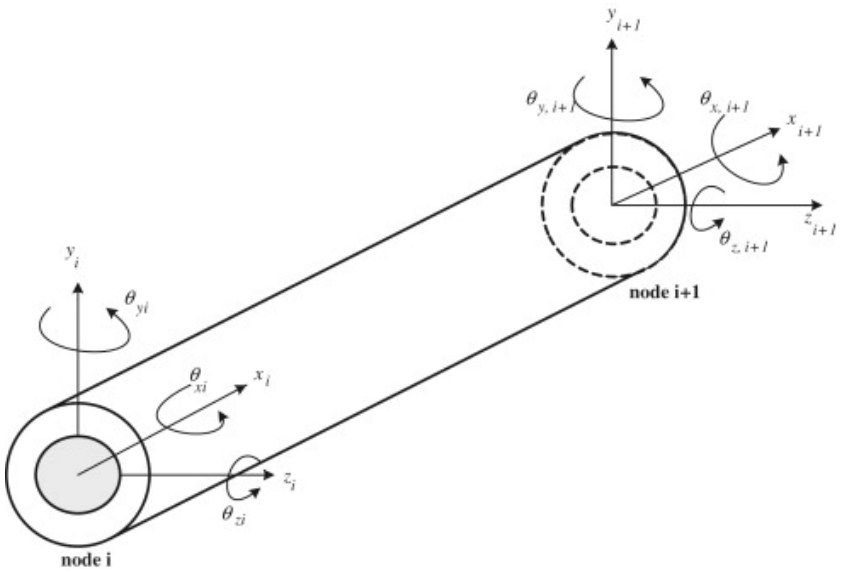


Figure 5-1 3-Dimensional beam element [22]

Each node has six degrees of freedom. With the usual linear elastic assumptions, the element vector of displacement and rotation is arranged according to the following convention.

$$X_e = \begin{bmatrix} x_i & y_i & z_i & \theta_{x,i} & \theta_{y,i} & \theta_{z,i} & x_{i+1} & y_{i+1} & z_{i+1} & \theta_{x,i+1} & \theta_{y,i+1} & \theta_{z,i+1} \end{bmatrix} \quad (5.1)$$

For formulating the mass and stiffness matrix, lumped mass method approach is used from the two methods available: consistent mass and lumped mass approach. The coded finite element algorithms for assembling the global matrices work equally well with both the approaches. The coded FEM algorithm methodology and the approach to simulate the complete system is the same as that described in [22].

To form the damping matrix, the damping coefficients $C_{x,i}$, $C_{y,i}$ and $C_{z,i}$ are directly added to the related node in their corresponding $x_i$, $y_i$ and $z_i$ directions of the C matrix.

To obtain the gyroscopic matrix of each element, the angular momentum $H = I_p \omega$ needs to be considered (shown in Figure 5-2).

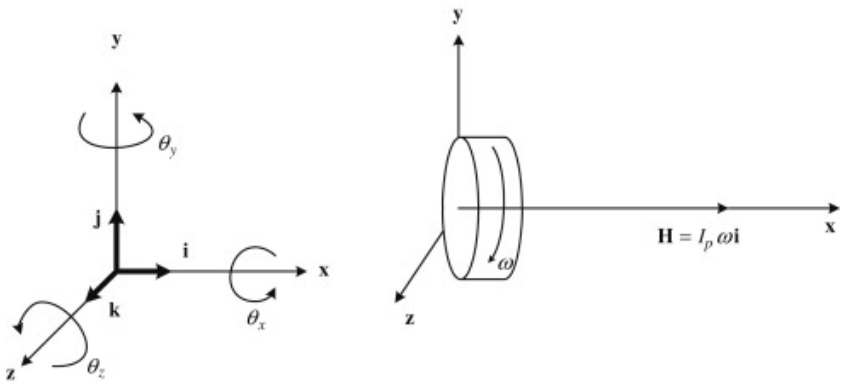


Figure 5-2 Coordinate convention and angular momentum [22]

According to Newton's Law, a torque T applied to the element results in

$$T = \frac{dH}{dt} = I_p \Omega \times \omega \tag{5.2}$$

where,

$I_p$ - Element polar moment of inertia

$\omega$ - Constant angular velocity of the shaft

$\Omega$ - Angular velocity of the element coordinate system

$\Omega = \dot{\theta}_x i + \dot{\theta}_y j + \dot{\theta}_z k$

Simplifying further, we get:

$$T = I_p \omega \dot{\theta}_z j - I_p \omega \dot{\theta}_y k \tag{5.3}$$

Thus the resulting gyroscopic matrix is given by:

$$\begin{matrix} & x_i & y_i & z_i & \theta_{x,i} & \theta_{y,i} & \theta_{z,i} & \\ G_i = & \begin{bmatrix} 0 & 0 & 0 & 0 & 0 & 0 \\ 0 & 0 & 0 & 0 & 0 & 0 \\ 0 & 0 & 0 & 0 & 0 & 0 \\ 0 & 0 & 0 & 0 & 0 & 0 \\ 0 & 0 & 0 & 0 & 0 & I_{p,i}\omega \\ 0 & 0 & 0 & 0 & -I_{p,i}\omega & 0 \end{bmatrix} & \begin{matrix} x_i \\ y_i \\ z_i \\ \theta_{x,i} \\ \theta_{y,i} \\ \theta_{z,i} \end{matrix} \end{matrix} \tag{5.4}$$

The assembly of all the element matrices (Mass M, Stiffness K, Gyroscopic G and Damping C) result in global matrices of dimension $6N \times 6N$, where $N$ is the total number of nodes.

### 5.1.2 EEC test rig model

The complete test rig rotor model is discretized into a number of small elements and nodes are assigned at various intermediate locations resulting in a total of 29 nodes. Figure 5-3 shows the locations of different nodes on the actual rotor shaft.

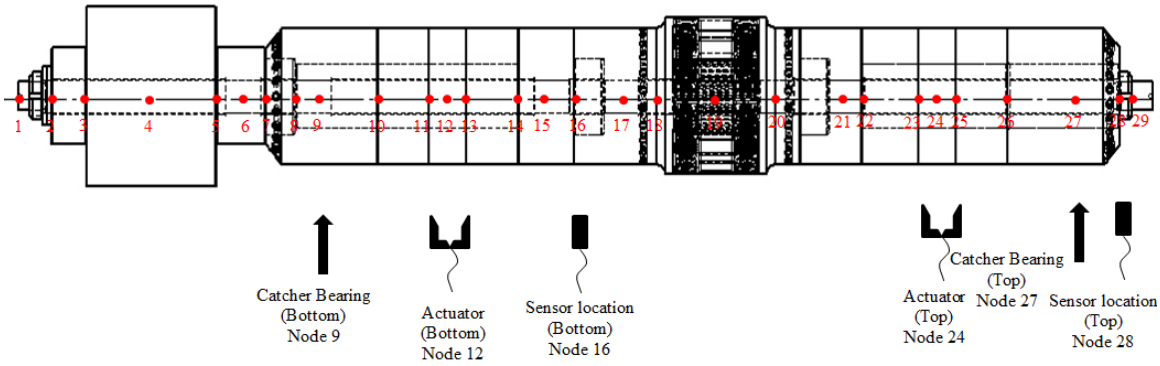


Figure 5-3 Finite element discretization of the EEC rotor shaft

Due to the different material properties of the individual parts of the rotor (Figure 2-6), only certain sections of the shaft contribute towards stiffness offered by the complete shaft. From the machine drawings of the individual shaft parts, these values were input to the Matlab code and it was programmed to output the mass and rotor profile (shown in Figure 5-4).

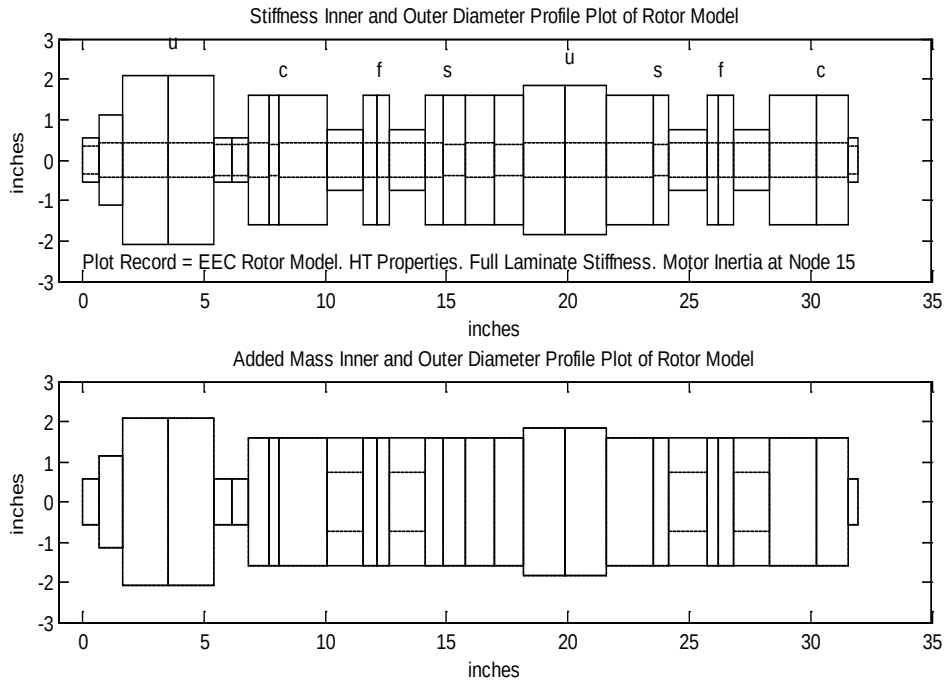


Figure 5-4 Mass and stiffness rotor profile of the EEC model

The system stiffness matrix, mass matrix, and gyroscopic matrix are of the dimension 396 x 396. The main system parameters are as follows:

a) Material properties of Inconel at 1000F are considered for the entire model:

   i) Young's Modulus E = 25.5e6 lbf./in²

   ii) Poisson's ratio nu = 0.284

   iii) Mass density ρ = 0.296 lb./in³

b) Following nodal locations are considered for the magnetic suspension system:

   i) Top bearing sensor node (Node 28), Top catcher bearing node (Node 27) and Top bearing actuator node (Node 24)

   ii) Bottom bearing sensor node (Node 16), Bottom catcher bearing node (Node 9) and Bottom bearing actuator node (Node 12)

c) A voltage stiffness value of 216 lbs./volt and position stiffness value of 70000 lbs./in is considered for both the bearings. (These values were determined experimentally in [1]).

The complete system equation, to solve for obtaining the system performance, can then be written as:

$$\dot{W}_{sys} = A_{sys} W_{sys} + B_{sys} u_{sys} \tag{5.5}$$

where,

$W_{sys}$ - Vector that is formulated from the structural variables plus the controller state variables

$A_{sys}$ - System matrix that includes the structural stiffness matrix, mass matrix, gyroscopic matrix, damping matrix, and the controller dynamic parameters

$B_{sys}$ - Input matrix

## 5.2 Rotordynamic synthesis

The mass-spring-damper equation of motion which describes the mechanical system of a spinning shaft is given by:

$$M\ddot{X} + C\dot{X} + KX = F \tag{5.6}$$

where,

M – Mass Matrix

K – Stiffness Matrix

C – Damping Matrix

F – External exciting force

X – Displacement vector

$$X = [x_1 y_1 z_1 \theta_{x1} \theta_{y1} \theta_{z1} .... x_N y_N z_N \theta_{xN} \theta_{yN} \theta_{zN}]^T \tag{5.7}$$

In any rotordynamic analysis, the equations of motion are expressed in first-order ODE expression. Therefore, Equation 5.5 can be written as:

$$\begin{bmatrix} M & 0 \\ 0 & I \end{bmatrix} \begin{bmatrix} \ddot{X} \\ \dot{X} \end{bmatrix} + \begin{bmatrix} C & K \\ -I & 0 \end{bmatrix} \begin{bmatrix} \dot{X} \\ X \end{bmatrix} = \begin{bmatrix} F \\ 0 \end{bmatrix} \tag{5.8}$$

Simplifying further, we get:

$$\begin{bmatrix} \ddot{X} \\ \dot{X} \end{bmatrix} = \begin{bmatrix} -M^{-1}C & -M^{-1}K \\ I & 0 \end{bmatrix} \begin{bmatrix} \dot{X} \\ X \end{bmatrix} + \begin{bmatrix} M^{-1}F \\ 0 \end{bmatrix} \tag{5.9}$$

Let $Z = [\dot{X} \quad X]^T$, therefore in the first order form we get:

$$\dot{Z} = A_{mat} Z + F \tag{5.10}$$

To reduce computing time, modal analysis is used in this multidimensional rotordynamic system study. Therefore we perform the following transformations: $Z = T\eta$ and $F = bu$. Equation (5.9) can then be written as:

$$T\dot{\eta} = A_{mat} T\eta + bu \tag{5.11}$$

Pre-multiplying by $T^{-1}$ on both sides, we get:

$$\dot{\eta} = T^{-1} A_{mat} T\eta + T^{-1} bu \tag{5.12}$$

Selecting $T$ such that it is the eigenvector of the $A_{mat}$ matrix, Equation (5.11) diagonalizes to

$$\dot{\eta} = \Lambda\eta + T^{-1}bu \tag{5.13}$$

where,

$\Lambda$ - Eigenvalue matrix

$\lambda_i$ - $i^{th}$ Eigenvalue

$\Lambda = T^{-1}A_{mat}T = diag(\lambda_1, \lambda_2, ....., \lambda_N)$

For a zero input response, the solution to Equation (5.12) is:

$$\eta(t) = e^{\Lambda t}\eta(0) \tag{5.14}$$

where,

Initial condition - $\eta(0) = T^{-1}Z(0)$

and $e^{\Lambda t} = diag([e^{\lambda_1 t}e^{\lambda_2 t}....e^{\lambda_N t}])$

Since $\eta(t) = T^{-1}Z(t)$, we have

$$T^{-1}Z(t) = e^{\Lambda t}\eta(0) = e^{\Lambda t}T^{-1}Z(0) \tag{5.15}$$

This leads to

$$Z(t) = Te^{\Lambda t}T^{-1}Z(0) \tag{5.16}$$

Since $T$ is an eigenvector of the $A_{mat}$ matrix, we can write:

$$Z(t) = e^{A_{mat}t}Z(0) \tag{5.17}$$

The system output $Z(t)$ can also be expressed as a summation of eigenvectors with appropriate vibration mode factors. Therefore,

$$Z(t) = T_1 e^{\lambda_1 t}\eta_1(0) + T_2 e^{\lambda_2 t}\eta_2(0) + \ldots + T_N e^{\lambda_N t}\eta_N(0) \qquad (5.18)$$

where,

$T_i$ - $i^{th}$ Eigenvector

$e^{\lambda_i t}$ - Appropriate vibration mode factor

$\varsigma$ - Damping ratio

$\omega_n$ - Natural frequency

$\omega_d$ - Damped natural frequency

$\omega_d = \omega_n\sqrt{1-\varsigma^2}$

$\lambda = -\varsigma\omega_n + i\omega_n\sqrt{1-\varsigma^2} = -\varsigma\omega_n + i\omega_d$

## 5.3 Magnetic suspension control synthesis

After obtaining the condensed system output vector, the PD controller is synthesized in the state variables using the state space method (same technique described in section 3.4.2) to do a complete closed loop system analysis. The proportional-derivative controller and compensators used in the closed loop analysis and simulation are given as follows:

Proportional control:

$$P_s(s) = \frac{K_p}{\tau s + 1} \qquad (5.19)$$

where,

$K_p$ - Proportional gain

Derivative control:

$$D_s(s) = \frac{K_d s}{(\tau s + 1)^2} = \frac{K_d s}{\tau^2 s^2 + 2\tau s + 1} \tag{5.20}$$

where,

$K_d$ - Derivative gain

Lead Compensator:

$$L_s(s) = K_{1d} \frac{s + z_0}{s + p_0} \tag{5.21}$$

where,

$K_{1d}$ - Gain of the lead compensator

Notch Filter:

$$\frac{y(s)}{x(s)} = \frac{s^2 + \omega_0^2}{s^2 + \left(\frac{\omega_0}{Q}\right)s + \omega_0^2} \tag{5.22}$$

where,

$\omega_0$ - Notch center frequency

$Q$ - Parameter which determines width of the notch in the frequency response.

Larger this value, smaller is the width and less effect on phase lag.

There are 3 notches placed at center frequencies of 700 Hz, 850 Hz and 1650 Hz in this controller design. These values have been determined after an exhaustive eigenvalue

analysis since the notch filter attenuates the position feedback signal in the range near its center frequency depending upon its depth and hence not allowing the bearings to produce forces to excite any vibrations.

### 5.3.1 *Optimal Proportional-Derivative gain set which results in maximum value for the minimum value of eigenvalue damping ratio (ζ)*

To find the optimal gain set, an iterative method was employed in the coded algorithm. For each gain set, only which result in all stable eigenvalues, the value of damping ratio (ζ) was obtained for each eigenvalue. The minimum of these damping ratio values is selected for each gain set and from these minimum values, the gain set with the maximum value of Zeta (ζ) is selected for optimum value. Figure 5-5 & Figure 5-6 show the PD gain pairs which produce all stable eigenvalues. After computing the eigenvalue damping ratios corresponding to each of the gain pairs shown in Figure 5-5 & Figure 5-6, the PD gain pair corresponding to a Proportional gain of 3 & Derivative gain of 2 on the A bearing (highlighted red in Figure 5-5) was found to have the minimum eigenvalue damping ratio of 1.4% (maximum of the minimum of all eigenvalue damping ratios corresponding to each gain pair). This optimal gain pair is used as an input to the coded algorithm to obtain the system performance.

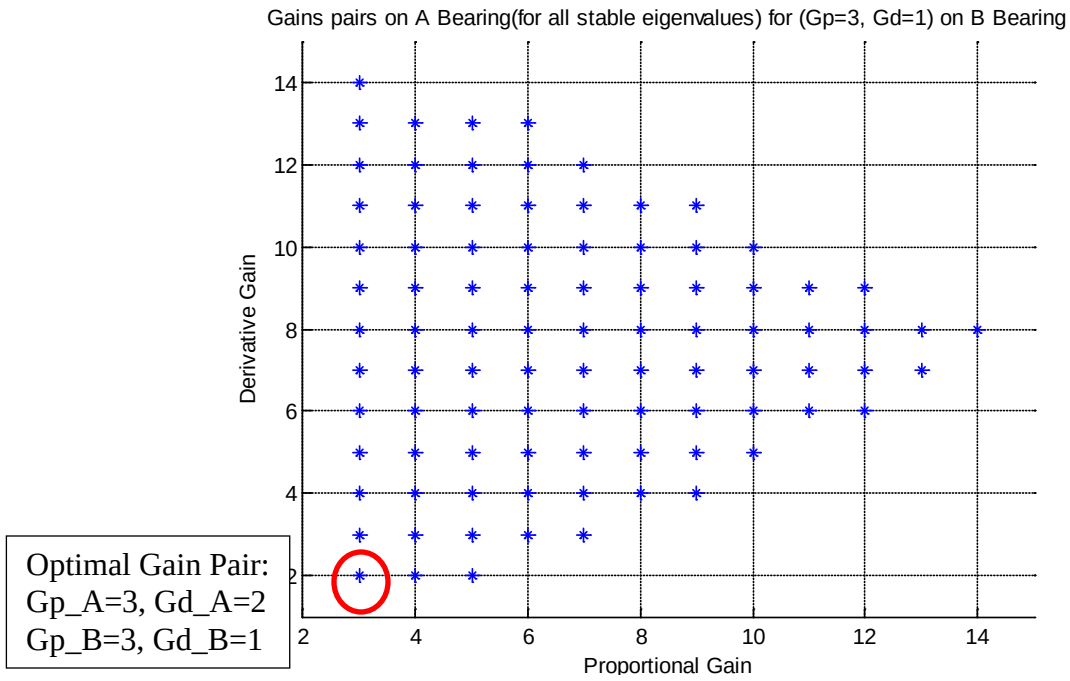


Figure 5-5 2-D plot showing external Proportional-Derivative gain pairs which produce all stable eigenvalues for Gp_B=3 & Gd_B=1

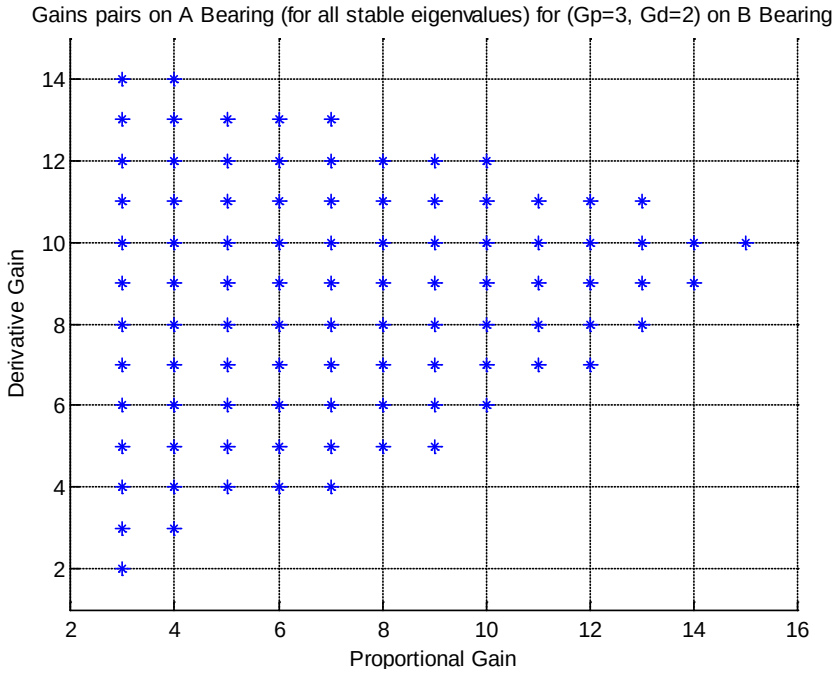


Figure 5-6 2-D plot showing external Proportional-Derivative gain pairs which produce all stable eigenvalues for Gp_B=3 & Gd_B=2

Selecting this value of proportional-derivative gain pair, corresponding to the maximum value for the minimum value of eigenvalue damping ratio (ζ) as an input to the coded algorithm, the system performance is obtained. From Figure 5-7, we see that the closed loop system is stable since all the eigenvalues lie in the left half of complex plane (Stability criterion of a linear control system). Figure 5-8 & Figure 5-9 show a more zoomed in location of eigenvalues near the origin.

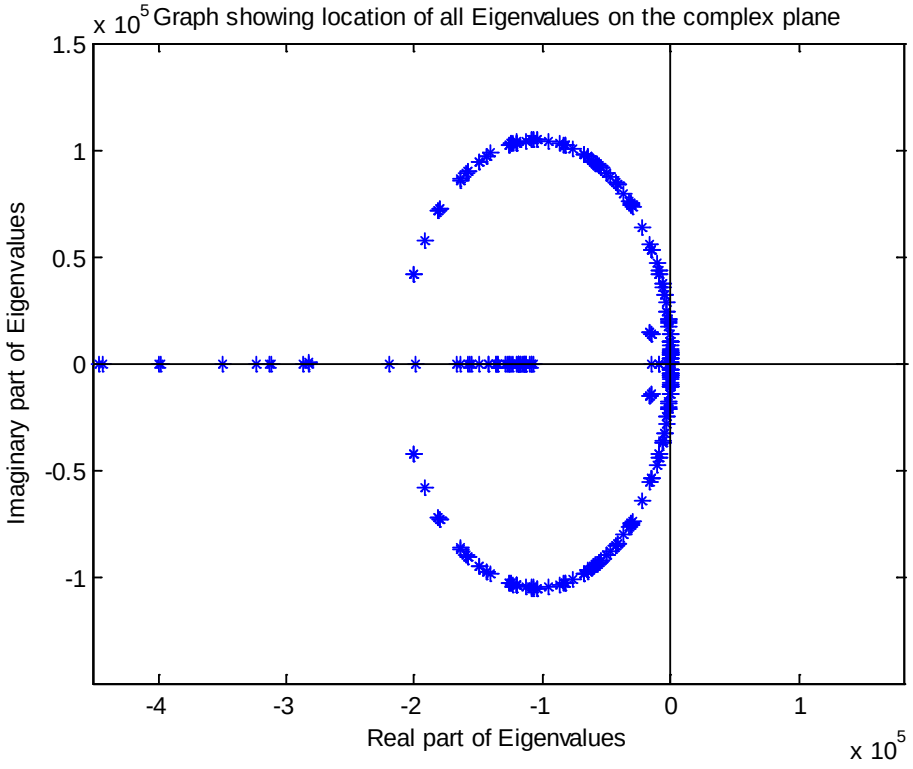


Figure 5-7 Location of all the system eigenvalues on the complex plane

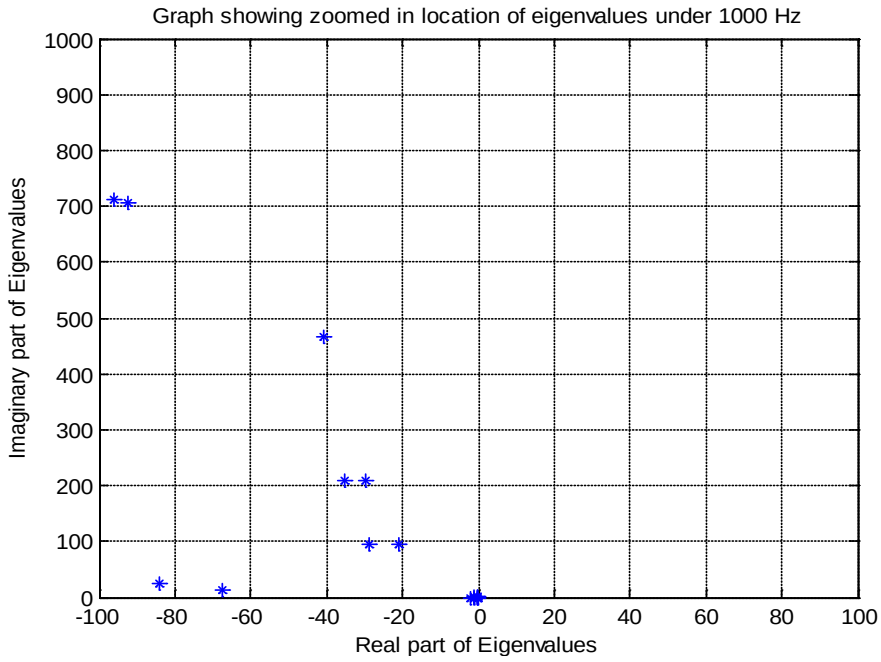


Figure 5-8 Location of system eigenvalues with positive imaginary parts under 1000 Hz (zoom in of Figure 5-6)

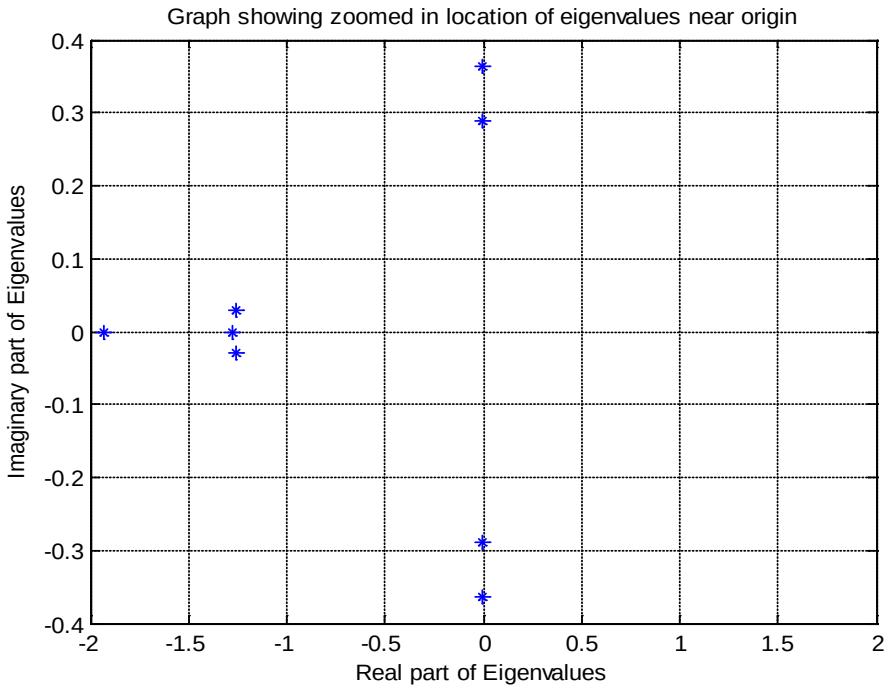


Figure 5-9 Location of system eigenvalues near origin (zoom in of Figure 5-6)

Using this external PD gain set and multiplying it with the transfer function obtained in section 3.4 (for one channel), a bode plot is obtained and superimposed with the analytically derived transfer function used in the coded FEM algorithm. Figure 5-10 shows the superimposed plot.

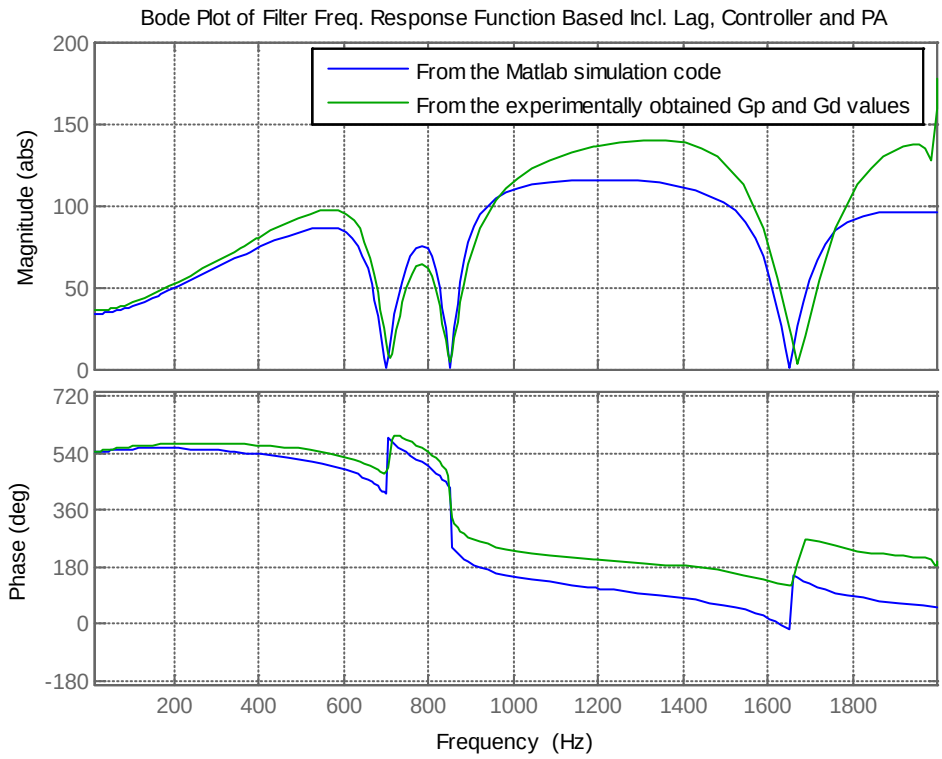


Figure 5-10 Superimposition of bode plots from Matlab code and experimentally obtained values

Figure 5-11 shows the mode shapes of the undamped zero speed system and the closed loop mode shapes are shown in Figure 5-12, Figure 5-13, Figure 5-14, Figure 5-15,

Figure 5-16, Figure 5-17, Figure 5-18, Figure 5-19 & Figure 5-20. Each of these mode shapes have to be controlled and the respective figures show the amount of damping obtained for each mode shape, using the control scheme implemented.

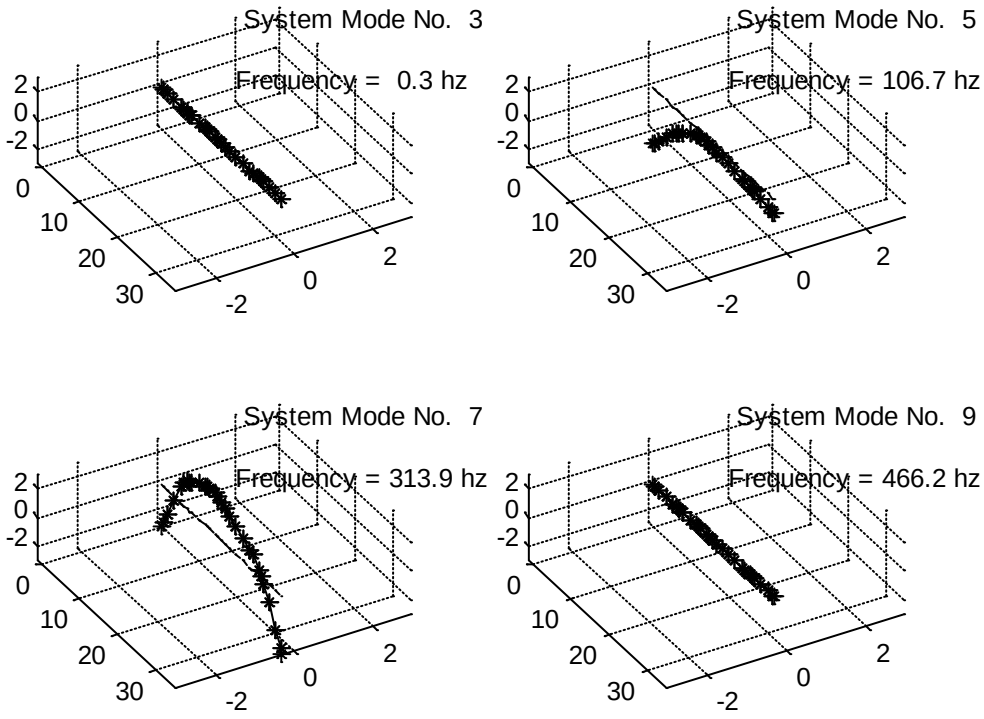


Plot Record = EEC Rotor Model. HT Properties. Full Laminate Stiffness. Motor Inertia at Node 15

Figure 5-11 Mode shapes of undamped ideal (infinite bandwidth), zero speed system

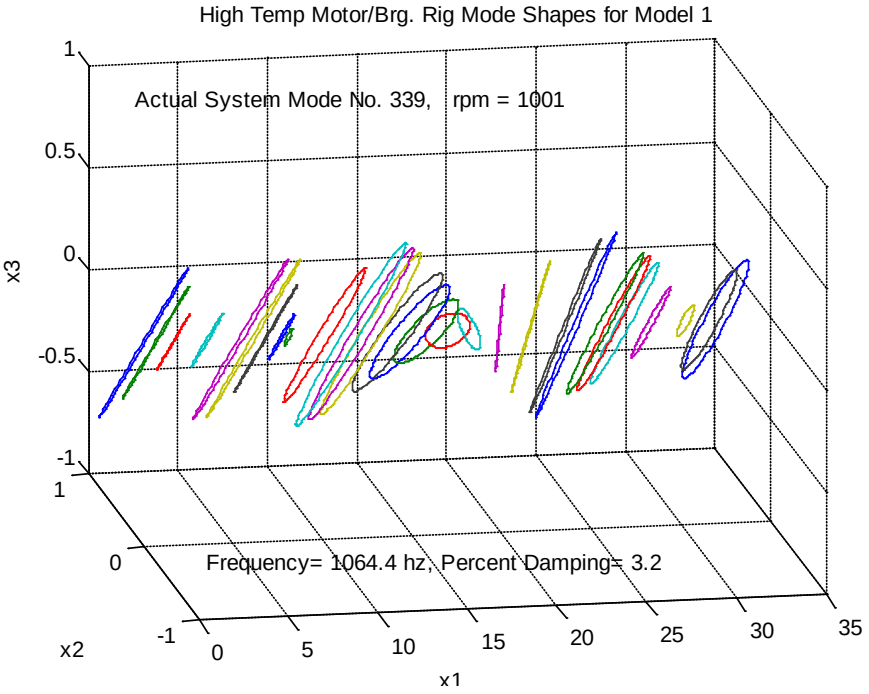


Figure 5-12 Actual (non-ideal) closed loop mode shape no. 339

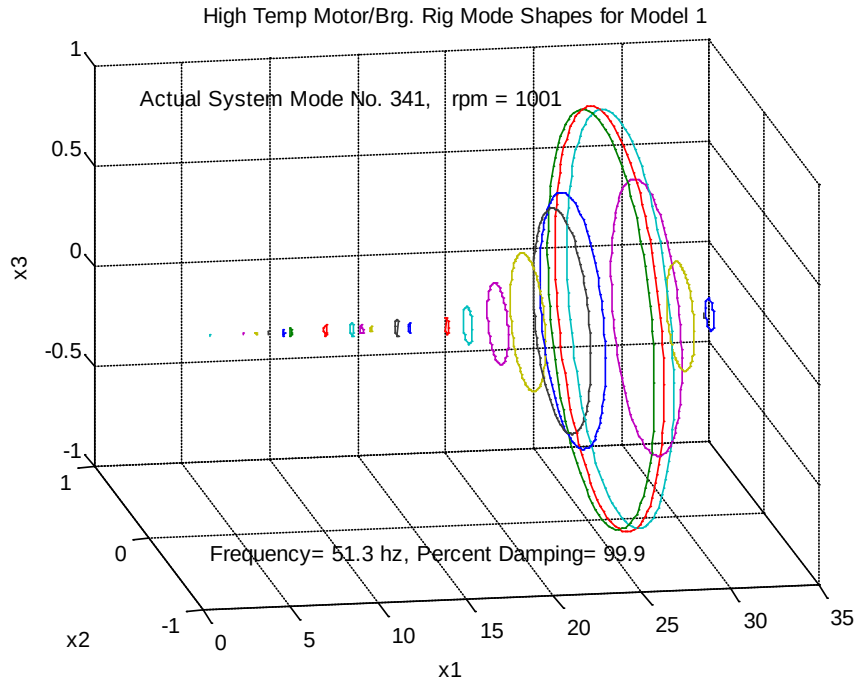


Figure 5-13 Actual (non-ideal) closed loop mode shape no. 341

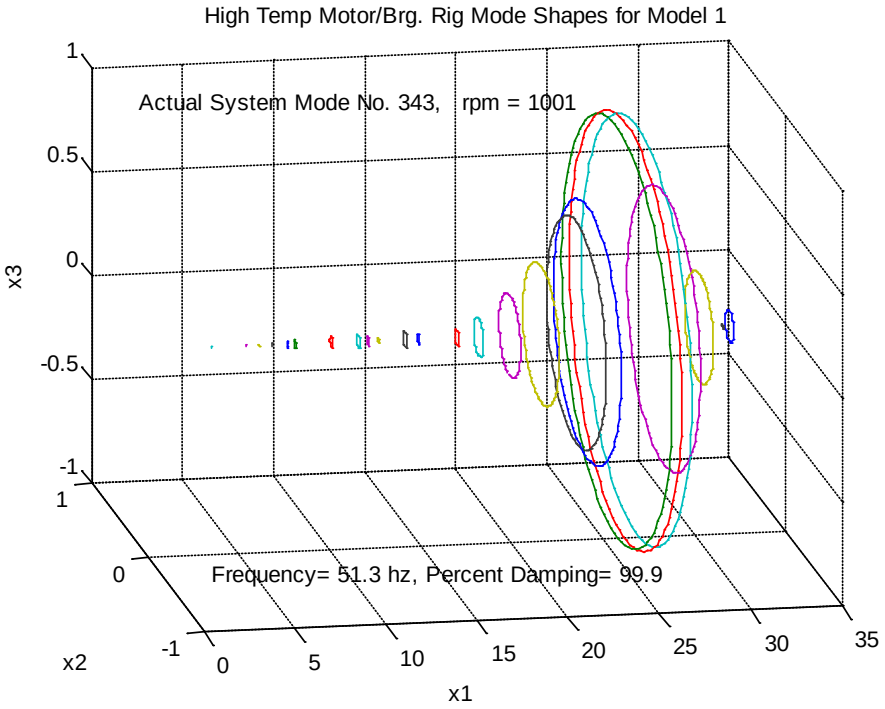


Figure 5-14 Actual (non-ideal) closed loop mode shape no. 343

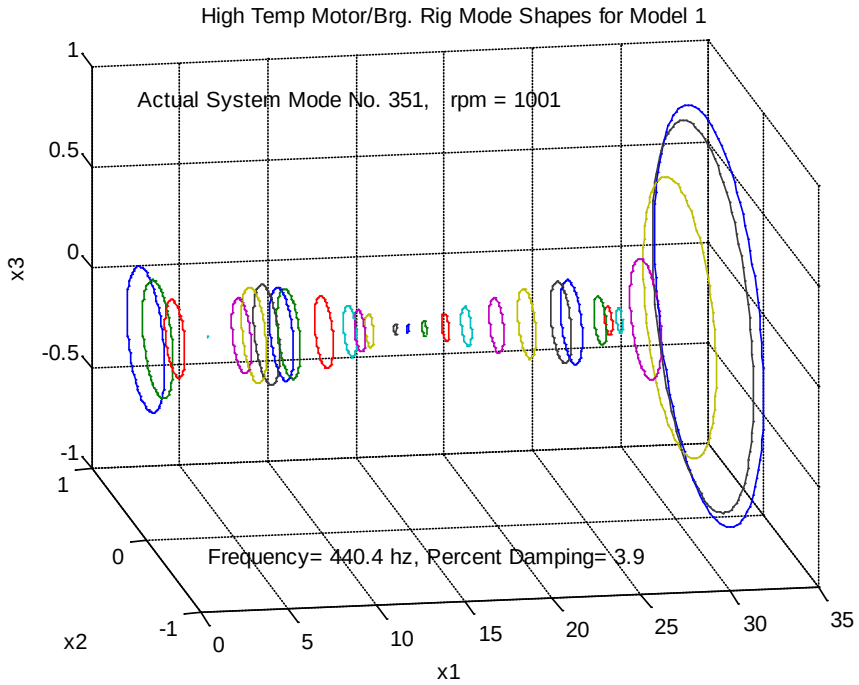


Figure 5-15 Actual (non-ideal) closed loop mode shape no. 351

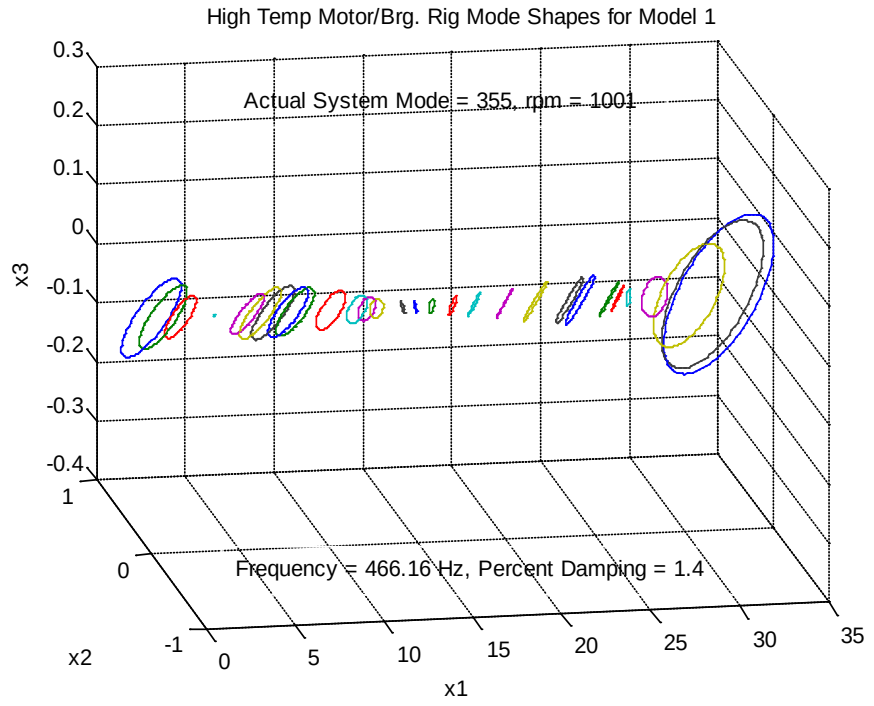


Figure 5-16 Actual (non-ideal) closed loop mode shape no. 355

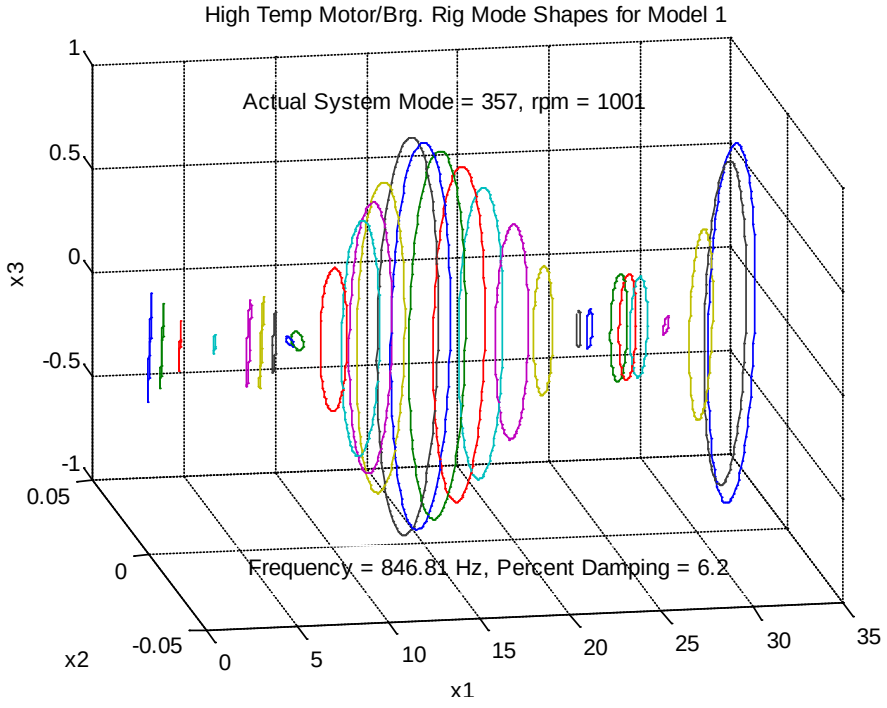


Figure 5-17 Actual (non-ideal) closed loop mode shape no. 357

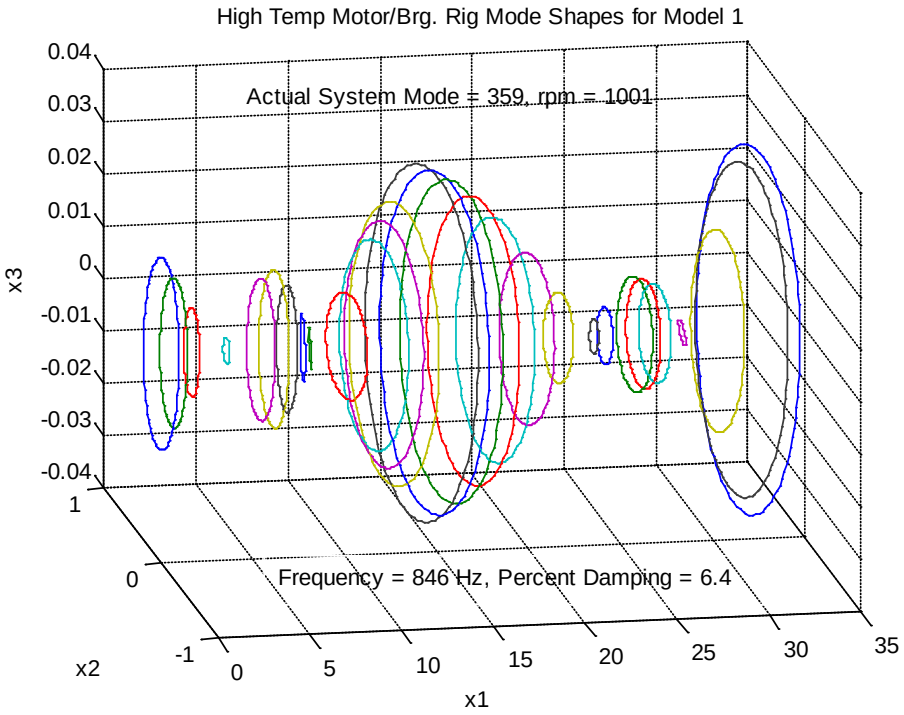


Figure 5-18 Actual (non-ideal) closed loop mode shape no. 359

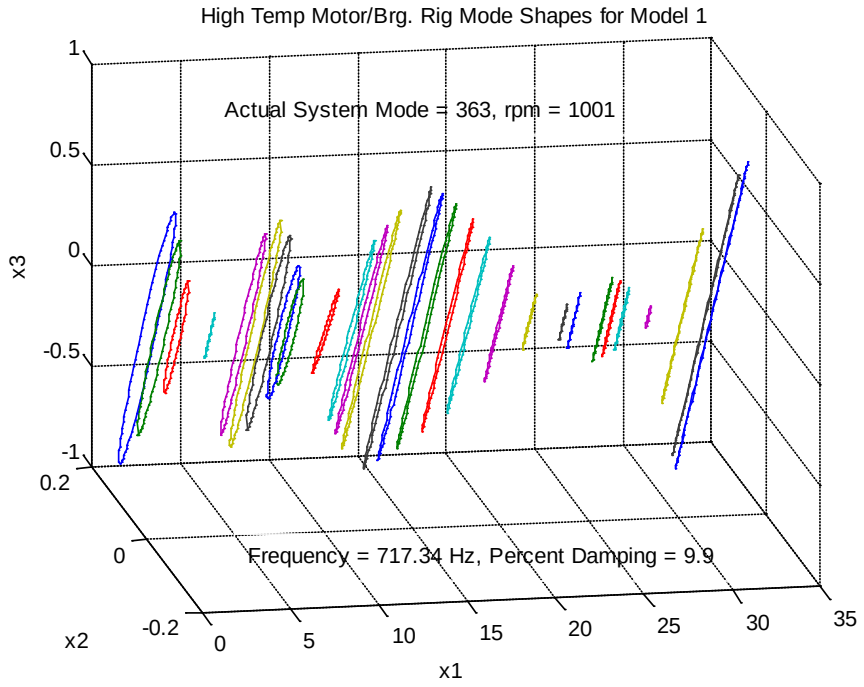


Figure 5-19 Actual (non-ideal) closed loop mode shape no. 363

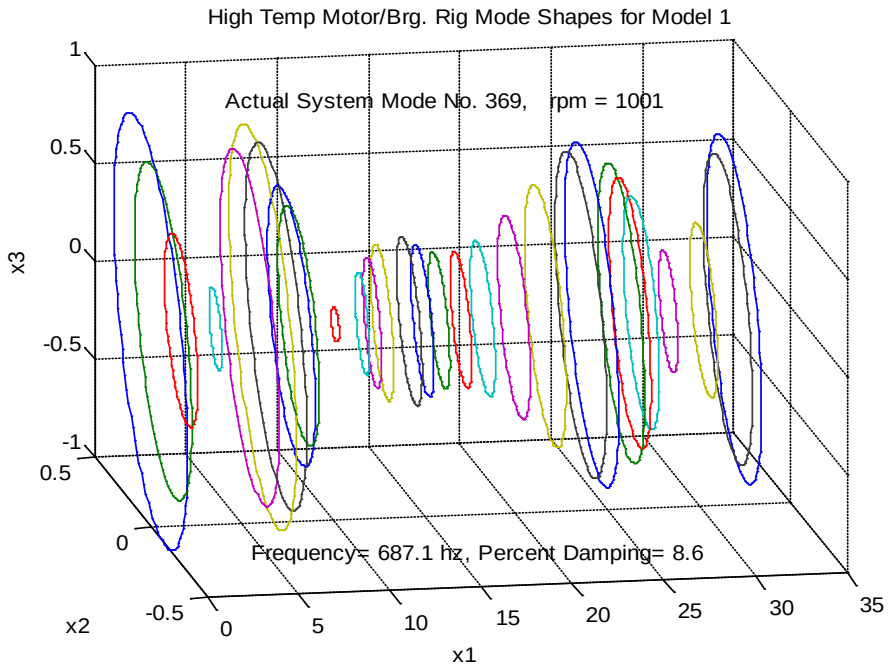


Figure 5-20 Actual (non-ideal) closed loop mode shape no. 369

# 6. CONCLUSION AND FUTURE WORK

## 6.1 Conclusion

The primary objective of this thesis was to assemble the complete universal magnetic bearing system and test for its levitation at low temperatures (300K) and low speeds (≈5000 RPM) by developing an appropriate feedback controller for the complete system.

The following tasks have been accomplished:

- A PD feedback control law was developed for the complete system with appropriate optimal P and D gains (obtained after simulating the dynamics of the assembled system).
- The complete universal magnetic bearing system has been assembled carefully, with the design specifications in mind, by making use of specially designed fixtures and pre-practiced techniques to enable the operation. Details can be found in Section 4.
- Many improved design modifications have been incorporated during the assembly phase to improve reliability and successful operation.

However, during the initial stages of testing, big circulatory and oscillatory movement of the lamination stack (otherwise stationary) was observed at just 1 Amp current value (the system is designed to operate with 10 Amps current value). This led to the fact that the magnetic forces (exerted by the bearings) overcame the sandwich preload forces (force which keeps the lamination stacks stationary with respect to the free shaft)

and concluding to a faulty design which otherwise should have incorporated for a greater sandwich preload. Further action has been stopped due to the scarcity of resources and further course of design improvements have been proposed in future work.

### 6.1.1 *Problem description*

A brief description of the assembly operation and the problem faced has been summarized in the following lines:

- The radial magnetic bearing assembly (along with its rotor shaft) and stator plate was guided carefully into the cylinder test rig as shown in Figure 6-1.

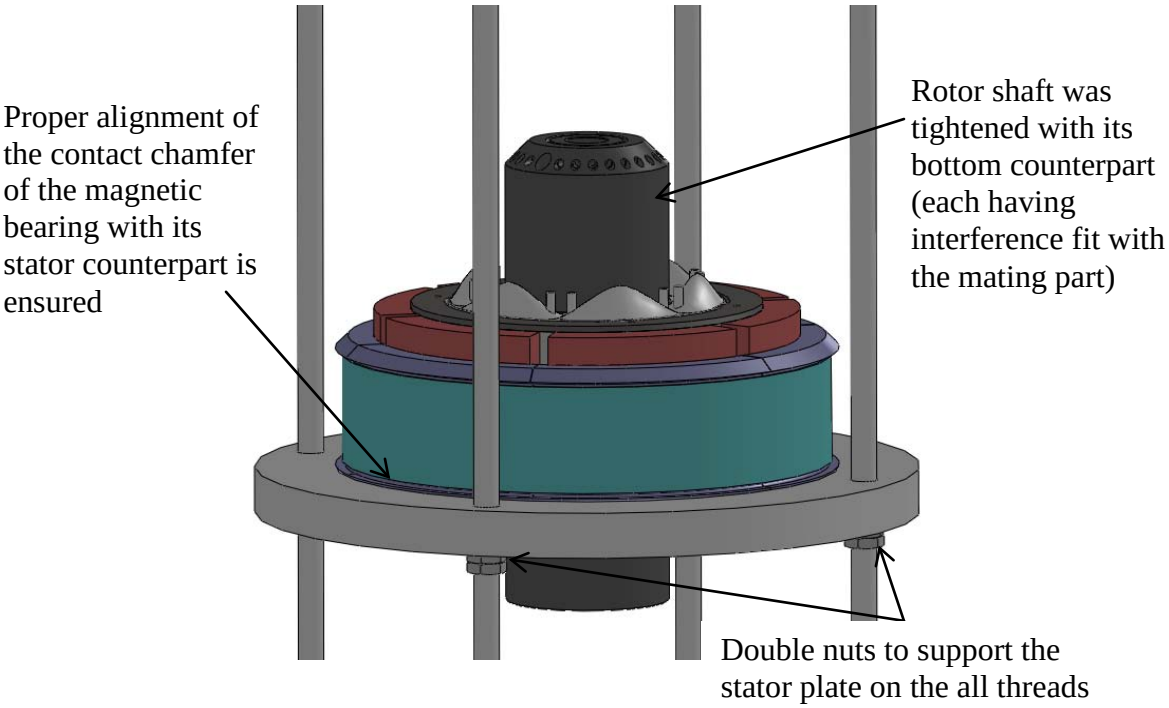


Figure 6-1 Radial magnetic bearing with its sandwich (or stator plate) placed on double nuts with the cylinder test rig (not shown)

- The top stator plate and catcher bearing stator plate were then placed carefully on the already assembled magnetic bearing as shown in Figure 6-2.

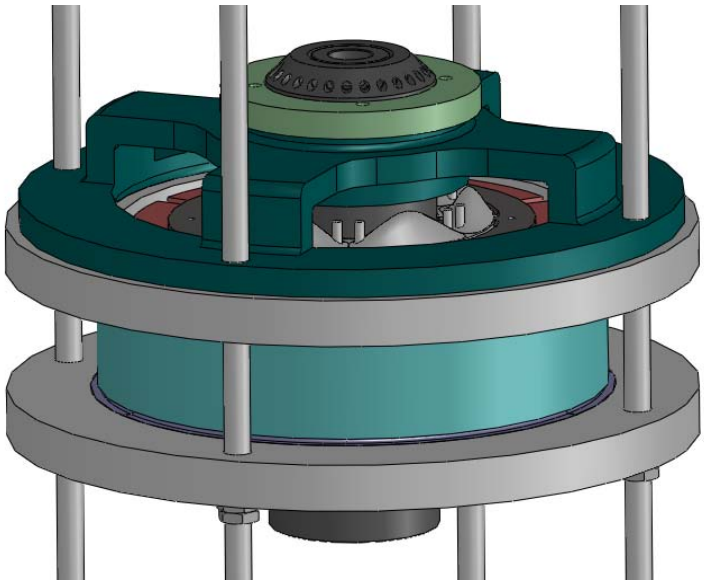

Figure 6-2 Top sandwich (or stator plate) along with the catcher bearing placed on the radial magnetic bearing

- All four top nuts were carefully tightened (one turn at a time) to ensure that the stator plate is translating down in a horizontal plane and it is not crooked on one side while being tightened. All the nuts were tightened to the maximum and ensured that there is no movement of the magnetic bearing between the two sandwiched plates i.e. the sandwich preload was maximum (Figure 6-3).

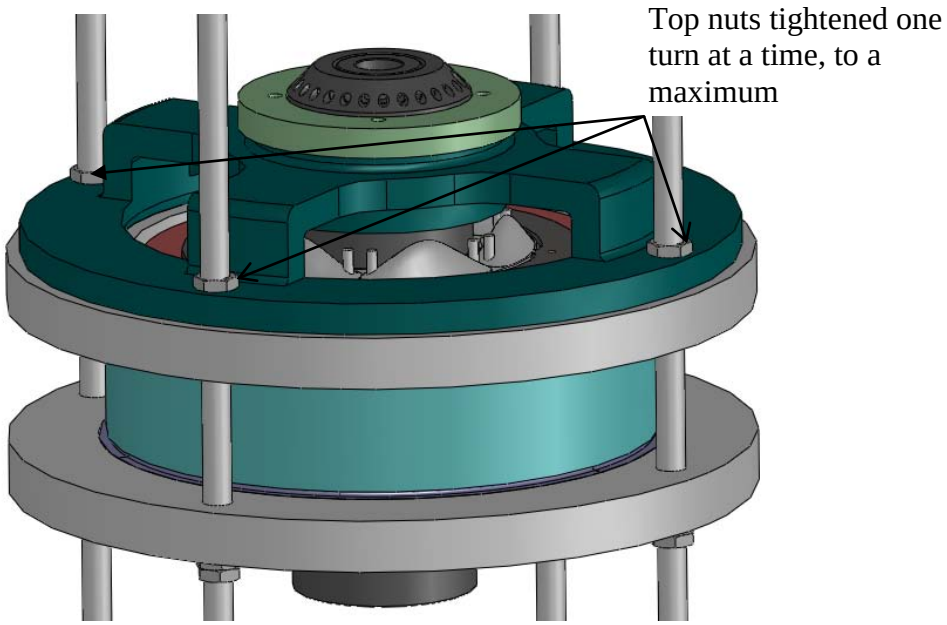


Figure 6-3 Top nuts tightened on the catcher stator plate to induce axial preload

- The radial setscrews were then tightened using an arrangement of dial indicators (indicating the movement of the stator plate in the X and Y direction) such that the net movement of the stator plate is zero or the plate is at its original position (before radial set screws were put in) after the screws had been tightened to the maximum. This approach was adopted for all the four radial set screws as shown in Figure 6-4.

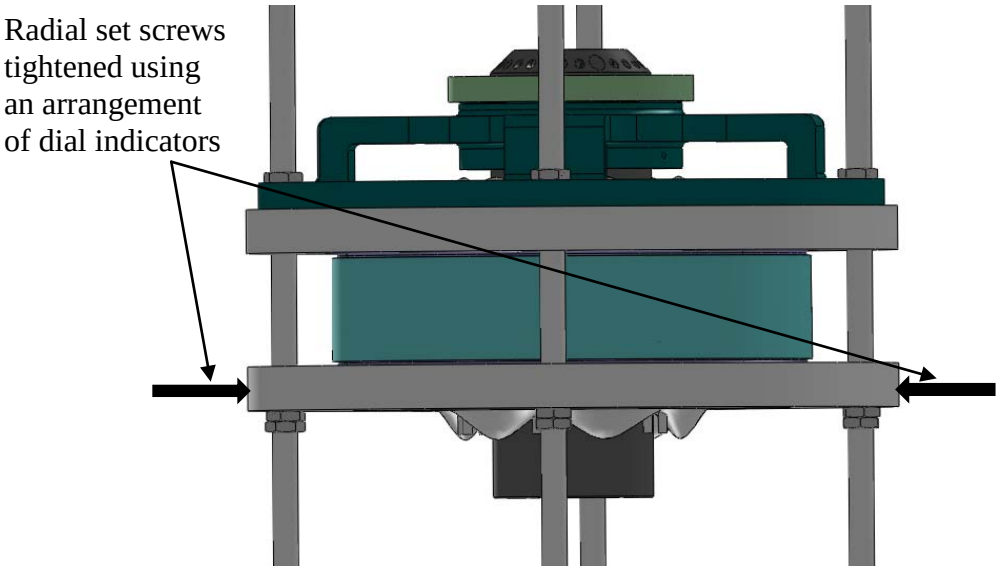


Figure 6-4 Radial set screws tightened to lock the plate radially

- Radial set screws tightened in all four directions using same approach (Figure 6-5).

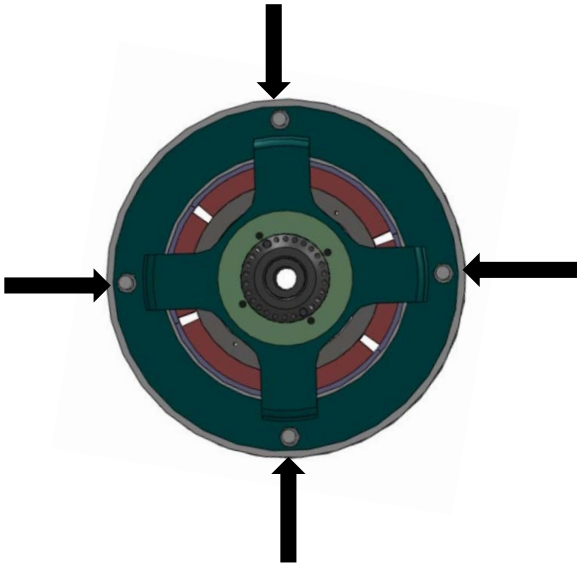

Figure 6-5 Stator plate locked radially with the help of radial set screws

- Similar procedure was repeated for the top stator plate and also the radial set screws were double nutted (i.e. another smaller set screw was inserted behind it) to prevent it from rolling or backing off due to any vibration as shown in Figure 6-6.

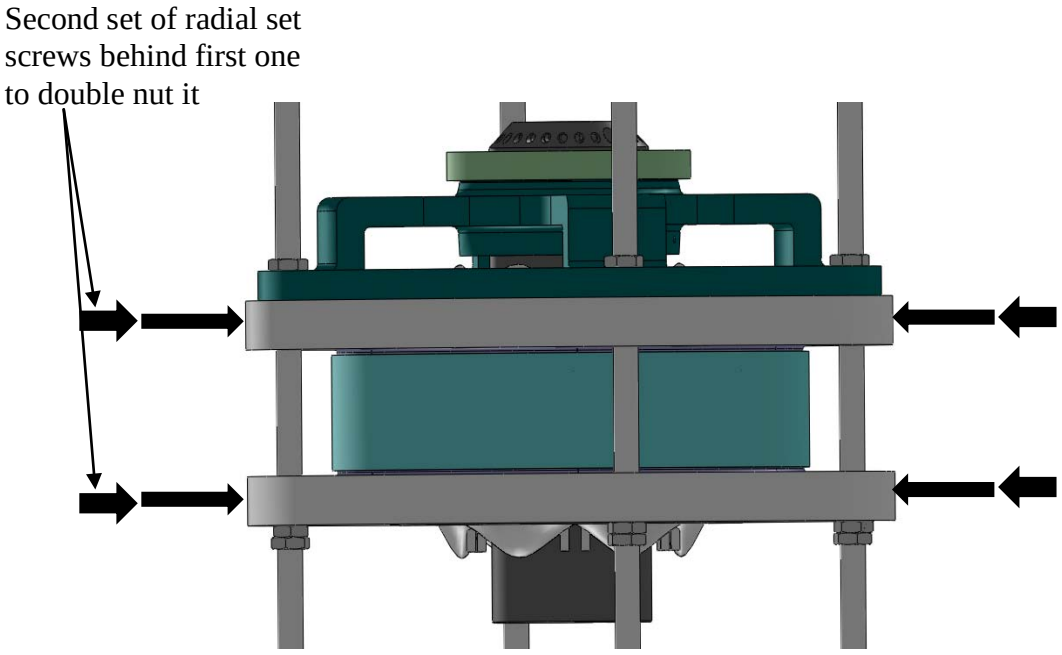


Figure 6-6 Radial set screws double nutted to prevent the first set from rolling back

- **At this point, an assumption was made that the radial load and axial (friction) preload of the set screws (pressing radially against the sandwich or stator plates through the cylinder housing) would be adequate to maintain the sandwich preload (initially provided by the top and bottom nuts on the supporting all thread)**. Now to bump the shaft to and fro in the magnetic bearing gap to find the magnetic center of the shaft through the sensors, the catcher

bearings had to be loosened to permit shaft movement (magnetic bearing clearance is 17 mils and catcher bearing clearance is 9 mils, on the radial). This was facilitated by loosening the top set of the four nuts providing the sandwich preload as shown in Figure 6-7.

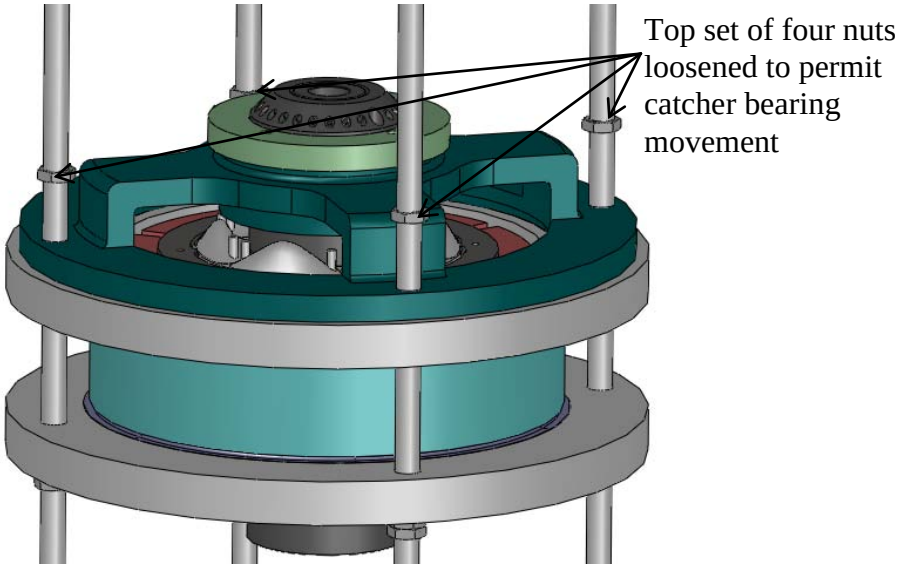


Figure 6-7 Sandwich preload through the top nuts released to permit catcher bearing movement

- Now it was assumed that the radial set screws would provide for the radial load and the axial preload due to friction between its contact surface and the stator plate (shown in Figure 6-8).

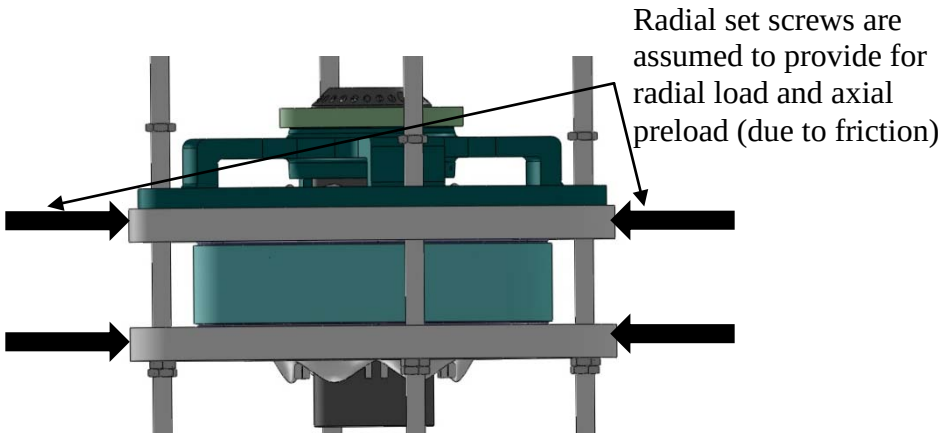


Figure 6-8 Front view of the assembled bearing with the radial forces (exerted by the radial set screws)

- The assumption made proved to be faulty since large movement (Figure 6-9) of the lamination stack was observed at a current rating of just 1 Amp (The system is designed to work with higher current values of the order of 10 Amps) i.e. the

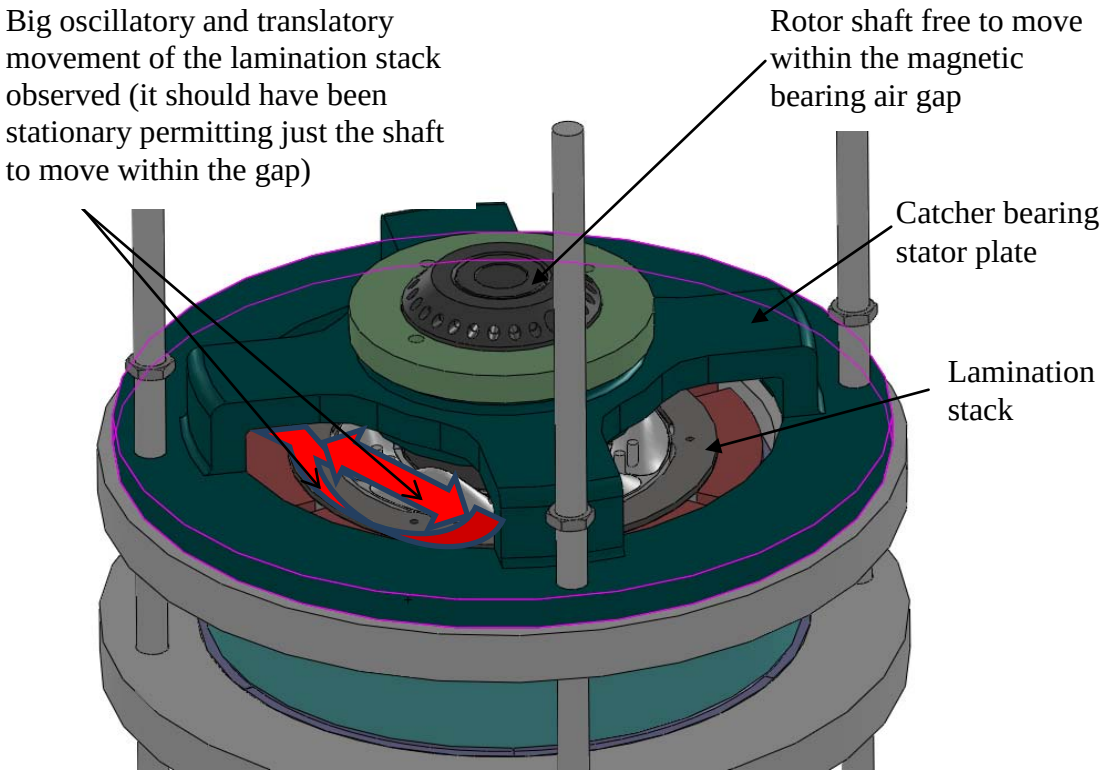


Figure 6-9 Oscillatory and translatory movement of the lamination stack

magnetic force overcame the supposed axial preload provided by the set screws.

- Due to this lamination stack movement, further action has been stopped and some design modifications have to be incorporated, after disassembling the individual parts, to test the magnetic bearings at their designed conditions.

## 6.2 Future work

The following course of further action is required:

- Since the shims have been removed (which was done to find the exact magnetic center), disassembly of the top radial bearing and motor is required to reinsert the shims. This has to be done so that the shaft is approximately in its air gap center in the assembled state (in lieu with the beginning intention).
- Machine the catcher bearing stator plates at the locations highligtened in Figure 6-10 to permit the axial screws to provide the sandwich preload in addition to the radial set screws and clamp down the catcher bearing stator plate to the magnetic bearing stator plate by means of a strong countersunk bolt, when the system is being run.

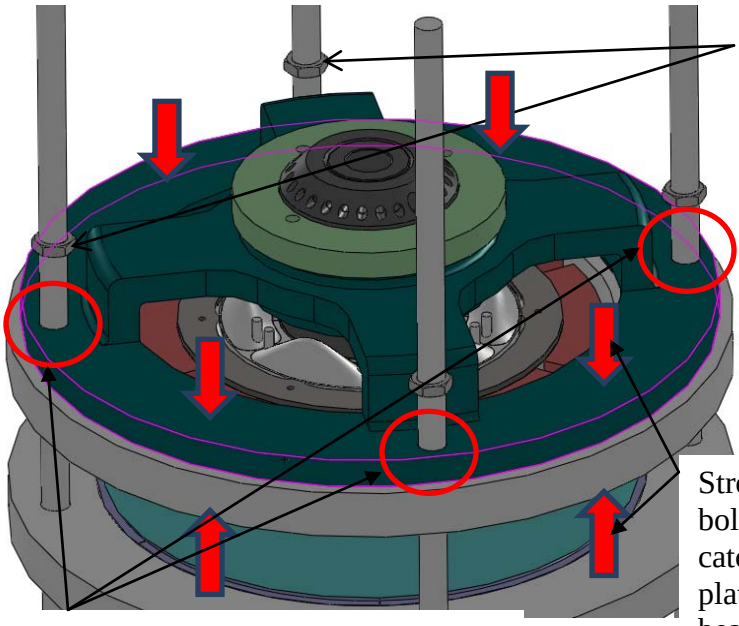


Figure 6-10 Proposed design modification

- Since the complete assembly has two sets of catcher bearings, a complete tear down of the assembled individual parts is required to incorporate the proposed design modifications in the bottom set of catcher bearing stator plate. A special disassembly rod with M20x0.75 external threads has to be fabricated to enable the disassembly of the individual mating parts of the rotor shaft. This rod is required to exert a small force to release the interference fit (Figure 4-2).
- Assemble all the individual parts using the similar method devised in this thesis and test the completely assembled rig at low temperatures of 300F and rotor speeds of 5000 RPM.

- Lower this assembled test rig into the spin pit to test it at designed conditions of 1000F and rotor speed of 20,000 RPM.

# REFERENCES

[1] DDS-Magnetic-Bearings power point slides, 2006, Magnetic Bearing Technology, Direct Drive Systems, Cerritos, CA.

[2] Dever, T. , Brown, G., Duffy, K., Jansen, R., August 16–19, 2004, "Modeling and Development of a Magnetic Bearing Controller for a High Speed Flywheel System," *Second International Energy Conversion Engineering Conference* sponsored by the American Institute of Aeronautics and Astronautics Providence, Rhode Island, NASA/TM - 2005-213877.

[3] Earnshaw, S., 1842, "On the Nature of the Molecular Forces which Regulate the Constitution of the Luminiferous Ether," *Transactions Of the Cambridge Philosophical Society*, Vol. 7, Part I, pp. 97 – 112.

[4] Gibbs, P. and Geim, A., March, 1997, "Is Magnetic Levitation Possible?" http://www.hfml.kun.nl/levitation-possible.html.

[5] Siebert, M., Ebihara, B., Jansen, R., Fusaro, R., Morales, W., Kascak, and A., Kenney, B., July 29 – August 2, 2001, "A Passive Magnetic Bearing Flywheel," 36th *Intersociety Energy Conversion Engineering Conference*, Savannah, Georgia, NASA TM-2002-211159.

[6] Gandhi V. R., 2009, "High Temperature, Permanent Magnet Biased, Magnetic Bearings," M.S. thesis, Texas A&M University, Department of Mechanical Engineering, College Station.

[7] Meeks, C. R., DiRusso, E., and Brown, G. V., 1990, "Development of a Compact, Light Weight Magnetic Bearing," *Proc. of the 26th Joint Propulsion Conference* AIAA/SAE/ASME/ASEE, Orlando, pp. 3420 – 3427.

[8] Sortore, C. K., Allaire, P. E., Maslen, E. H., Humphris, R. R., and Studer, P. A., 1990, "Permanent Magnetic Biased Bearings—Design, Construction, and Testing," *Proc. of the Second International Symposium on Magnetic Bearings*, Tokyo, pp. 175–182.

[9] Lee, A., Hsio, F., and Ko, D., 1994, "Analysis and Testing of Magnetic Bearing With Permanent Magnets for Bias," JSME Int. J., Ser. C, **37**, pp. 774-782.

[10] Imlach, J., Blair, B. J., and Allaire, P. E., 1990, "Measured and Predicted Force and Stiffness Characteristics of Industrial Magnetic Bearings," *Joint ASME/STLE Tribology Conference*, Toronto, **90**-Trib-70. 56.

[11] Masayuk, Y., 1999, "Magnetic Bearing Device," Japanese patent 11101234A.

[12] Nagahiko, N., 1986, "Magnetic Bearing," Japanese patent 61180019A.

[13] Kenny, A., Palazzolo, A., 2003, "Single Plane Radial, Magnetic Bearings Biased With Poles Containing Permanent Magnets," Transactions of the ASME, **125**, pp. 178-185.

[14] Provenza, A., Montague, G., Jansen, M., Palazzolo, A. and Jansen, R., 2005, "High Temperature Characterization of a Radial Magnetic Nearing for Turbomachinery," Journal of Engineering for Gas Turbines and Power, **127,** pp.437-444.

[15] Mohiuddin, M., 2002, "Design of High Temperature High Speed Electromagnetic Axial Thrust Bearing," Master's Thesis, Texas A&M University, Department of Mechanical Engineering, College Station.

[16] Zhenzxin Z, 2010, “High Temperature, Buried Permanent Magnet, Brushless DC Motor,” M.S. thesis, Texas A&M University, Department of Mechanical Engineering, College Station.

[17] Schweitzer, G., Maslen, E. H., 2009, *Magnetic Bearings – Theory, Design, and Application to Rotating Machinery*, Springer.

[18] Franklin, G. F., Powell, J. D., Emami-Naeini, A., 2008, *Feedback Control of Dynamic Systems*, Pearson Education, Inc.

[19] Li, M., 2004, “Fault Tolerant Control of Homopolar Magnetic Bearings and Circular Sensor Arrays”, Ph.D Dissertation, Department of Mechanical Engineering, Texas A&M University, College Station.

[20] Na, U., 1999, “Fault Tolerant Control of Heteropolar Magnetic Bearings”, Ph.D Dissertation, Department of Mechanical Engineering, Texas A&M University, College Station.

[21] Palazzolo, A., Tucker, R., Narain, A., Wadhvani, V., 2010, “Determination of Coefficient of Friction and Young’s Modulus of Graphalloy – A Report,” Experimental Report, Texas A&M University, Department of Mechanical Engineering, College Station.

[22] Lei, S., 2001, “Synthesis and Fuzzy Logic Control of Flexible Rotor Systems with Active Magnetic Suspensions”, Ph.D Dissertation, Department of Mechanical Engineering, Texas A&M University, College Station.

**Supplementary Sources Consulted**

Preuss, J., 2004 “Design and Analysis of a Composite Flywheel Preload Loss Test Rig,” M.S. Thesis, Department of Mechanical Engineering, Texas A&M University, College Station.

Palazzolo, A., Tucker, R., Kenny, A., Kang, K D., Gandhi, V., Liu, J., Choi, H. and Provenza, A., 2008, “High Temperature, Permanent Magnet Biased, Fault Tolerant, Homopolar Magnetic Bearing Development,” *Proceedings of ASME Turbo EXPO 2008: Power for Land, Sea and Air*, Berlin, Germany, GT2008-50917.

# APPENDIX A

## FABRICATION DRAWINGS FOR CATCHER BEARING ASSEMBLY

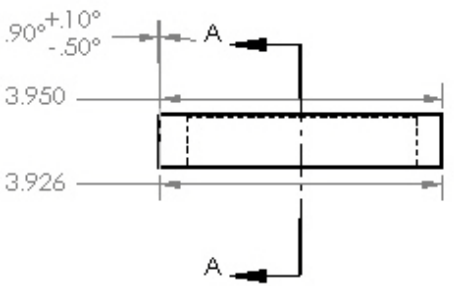


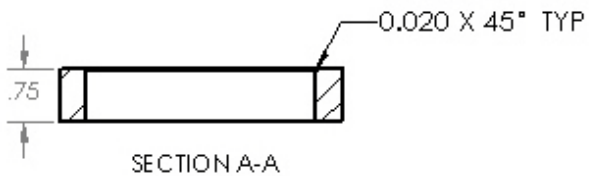


SECTION A-A
SCALE 1 : 2

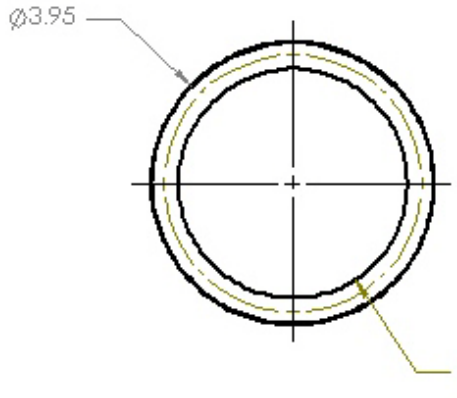


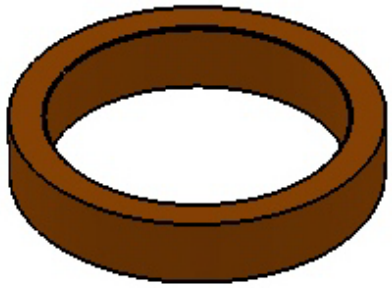

NOTE: FOR MACHINING DETAILS
CONTACT GRAPHALLOY WITH
THE MATERIAL NUMBER
(GMC Number TS126665-1)

| | | | | | | | |
|---|---|---|---|---|---|---|---|
| | | UNLESS OTHERWISE SPECIFIED: | | NAME | DATE | VIBRATION CONTROL AND ELECTROMECHANICS LAB | |
| | | DIMENSIONS ARE IN INCHES<br>TOLERANCES:<br>FRACTIONAL ±<br>ANGULAR: MACH ± BEND ±<br>TWO PLACE DECIMAL ± 0.005<br>THREE PLACE DECIMAL ± 0.001 | DRAWN | VISHAL | 01/20/10 | TITLE: GRAPHALLOY BEARING | |
| | | | CHECKED | | | | |
| | | | ENG APPR | | | | |
| | | | MFG APPR | | | | |
| | | | Q.A | | | | |
| | | INTERPRET GEOMETRIC TOLERANCING PER: | COMMENTS: | | | | |
| | | MATERIAL GRAPHALLOY GMC Number TS 126665-1 | | | | | |
| NEXT ASSY | USED ON | FINISH 8 MICRO-INCHES OR BETTER AS SPECIFIED 125 MICRONICH RMS | QTY : 02 | | | SIZE A | DWG. NO. 3602 (G) REV |
| APPLICATION | | DO NOT SCALE DRAWING | | | | SCALE: 1:4 | WEIGHT: SHEET 1 OF 1 |



5 4 3 2 1

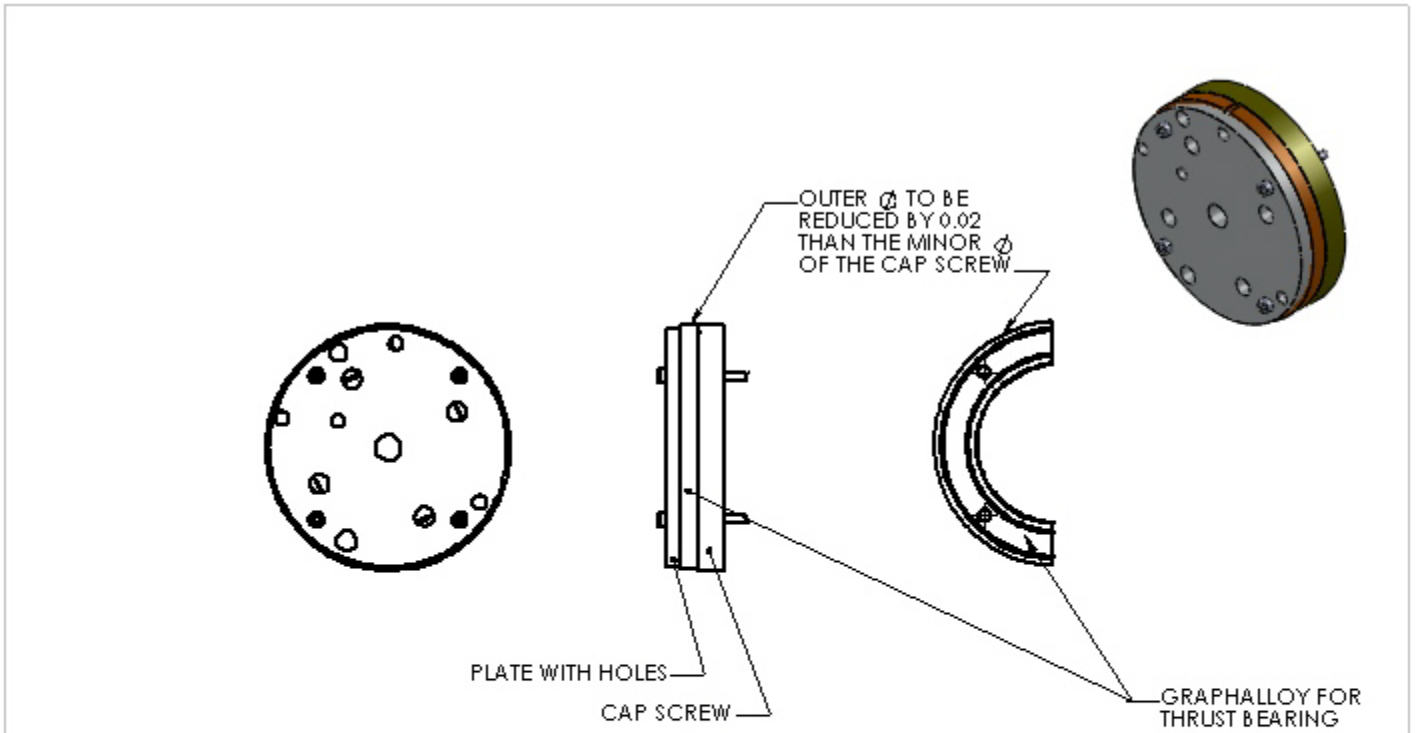


NOTE : THIS DRAWING IS ONLY FOR TURNING THE OUTER DIA OF GRAPHALLOY

| | NAME | DATE |
|---|---|---|
| DRAWN | VENAI | 02/02/10 |
| CHECKED | | |
| ENG APPR | | |
| MFG APPR | | |
| Q A | | |

COMMENTS:

QTY : 04

VIBRATION CONTROLAND ELECTROMECHANICS LAB

TITLE: GRAHALLOY FOR THRUST BEARING

| SIZE | DWG. NO. | REV |
|---|---|---|
| A | 3602 (TG) | |

SCALE: 1:2 | WEIGHT: | SHEET 1 OF 1



UNLESS OTHERWISE SPECIFIED:
DIMENSIONS ARE IN INCHES
TOLERANCES:
FRACTIONAL ±
ANGULAR: MACH ± BEND ±
TWO PLACE DECIMAL ± 0.005
THREE PLACE DECIMAL ±
INTERPRET GEOMETRIC TOLERANCING PER:
MATERIAL GRAPHALLOY
DO NOT SCALE DRAWING
NEXT ASSY | USED ON
APPLICATION

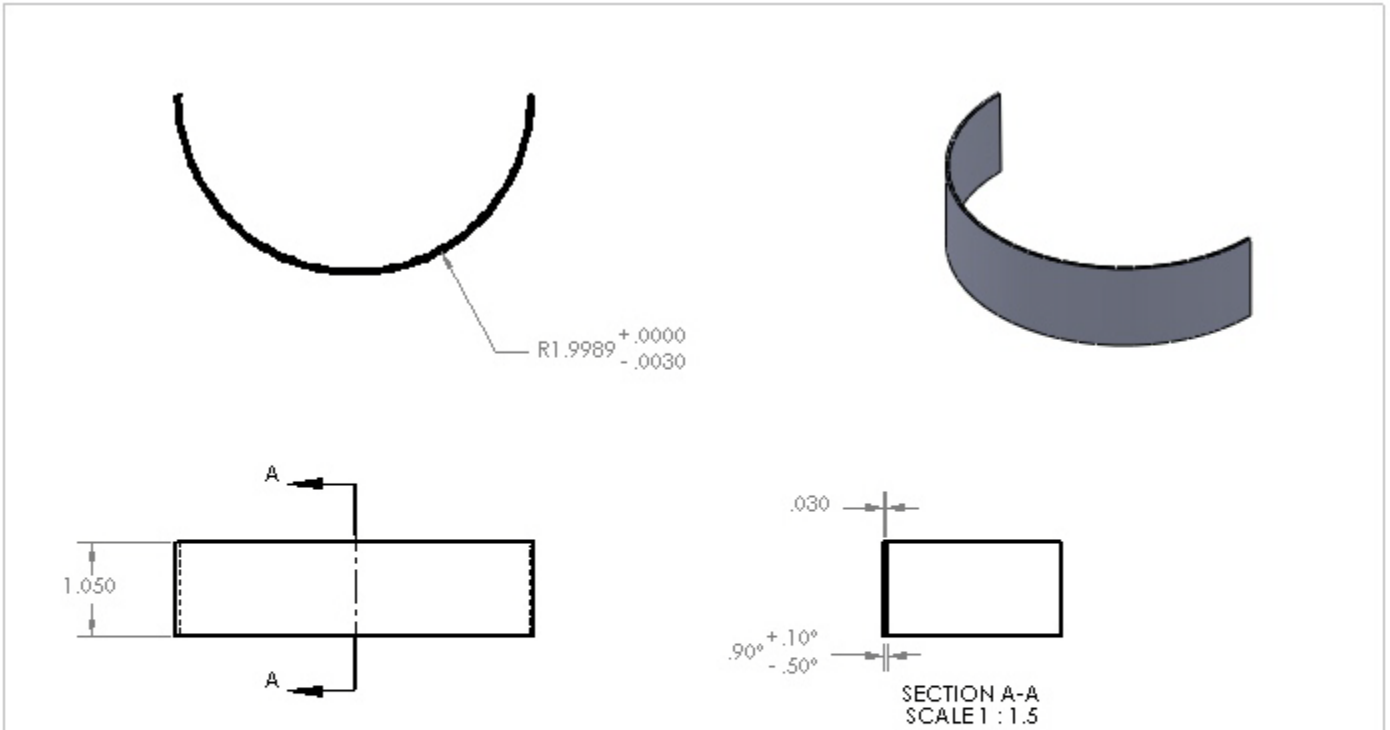
R1.9989 +.0000 -.0030
A
A
1.050
.030
.90° +.10° -.50°
SECTION A-A
SCALE 1 : 1.5
UNLESS OTHERWISE SPECIFIED:
DIMENSIONS ARE IN INCHES
TOLERANCES:
FRACTIONAL ±
ANGULAR: MACH ± BEND ±
TWO PLACE DECIMAL ±.010
THREE PLACE DECIMAL ±.005
INTERPRET GEOMETRIC TOLERANCING PER:
MATERIAL ABS ISEE1 3D4
FINISH
NEXT ASSY
USED ON
APPLICATION
DO NOT SCALE DRAWING
NAME
DATE
DRAWN
VENALI
11/21/09
CHECKED
ENG APPR
MFG APPR
Q.A
COMMENTS:
QTY: 04
(MODIFIED ON 12/19/09)
VIBRATION CONTROL AND ELECTROMECHANICS LAB
TITLE:
FEMALE PART
SHELL
SIZE
A
DWG. NO.
3602(FS)
REV
SCALE: 1:1
WEIGHT:
SHEET 1 OF 1
PROPRIETARY AND CONFIDENTIAL
THE INFORMATION CONTAINED IN THIS DRAWING IS THE SOLE PROPERTY OF <INSERT COMPANY NAME HERE>. ANY REPRODUCTION IN PART OR AS A WHOLE WITHOUT THE WRITTEN PERMISSION OF <INSERT COMPANY NAME HERE> IS PROHIBITED
5
4
3
2
1

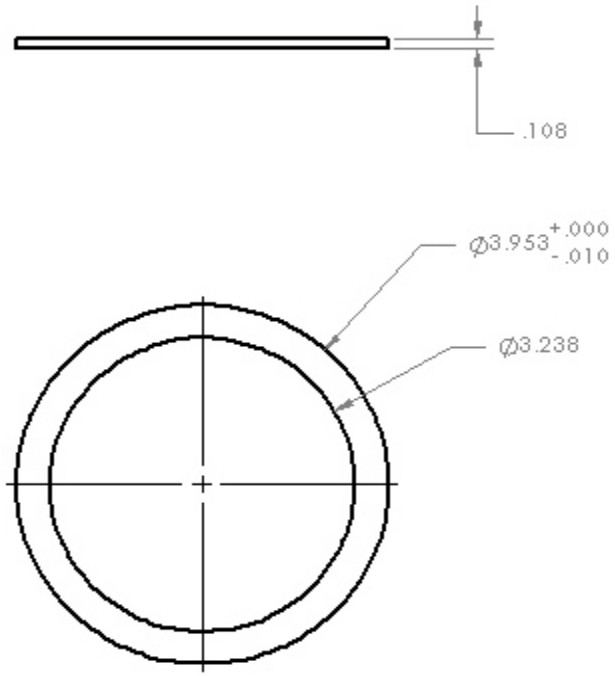


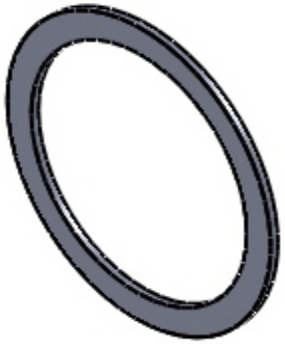

| | | | | | |
|---|---|---|---|---|---|
| | | UNLESS OTHERWISE SPECIFIED: | | NAME | DATE |
| | | DIMENSIONS ARE IN INCHES<br>TOLERANCES:<br>FRACTIONAL ±<br>ANGULAR: MACH ± BEND ±<br>TWO PLACE DECIMAL ±0.005<br>THREE PLACE DECIMAL ±0.001 | DRAWN | VENAI | 11/21/09 |
| | | | CHECKED | | |
| | | | ENG APPR | | |
| | | | MFG APPR | | |
| | | | Q A | | |
| | | INTERPRET GEOMETRIC TOLERANCING PER: | COMMENTS: | | |
| | | MATERIAL ABS/SHEET 30A | QTY: 02 | | |
| NEXT ASSY | USED ON | FINISH | (MODIFIED ON 12/19/09) | | |
| APPLICATION | | DO NOT SCALE DRAWING | | | |



VIBRATION CONTROL AND ELECTRO MECHANICS LAB

TITLE:

**FEMALE PART**
**WASHER**

| SIZE | DWG. NO. | REV |
|---|---|---|
| A | 3602(F) | |
| SCALE: 1:1 | WEIGHT: | SHEET 1 OF 1 |

# APPENDIX B

## FABRICATION DRAWINGS FOR LOCATION WASHER AND MODIFIED EEC MOTORSHAFT ROD

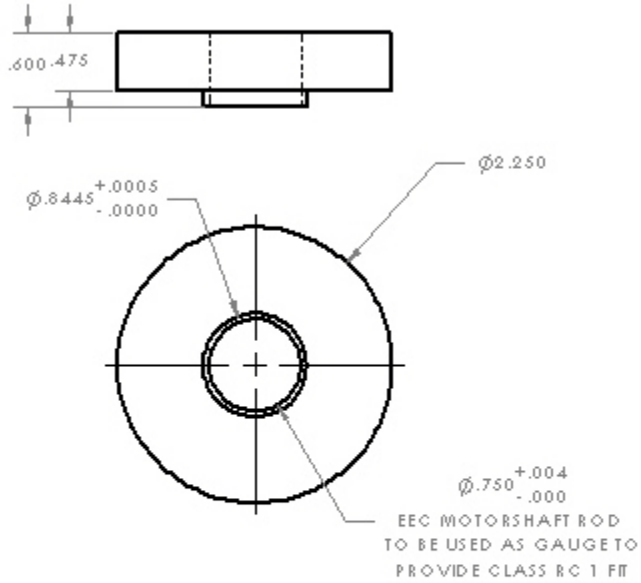


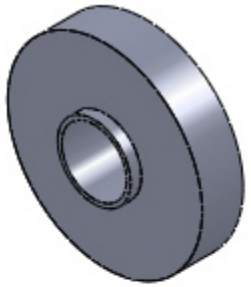

NOTE :

| CLASS RC 1 | | |
|---|---|---|
| CLEARANCE | HOLE H5 | SHAFT g4 |
| 0.3 | 0.4 | -0.3 |
| 0.95 | 0 | -0.55 |

ALL VALUES ARE IN THOUSANDS OF AN INCH

UNLESS OTHERWISE SPECIFIED:

DRAWN VISHAL 15/12/10

MATERIAL STAINLESS STEEL

VIBRATION CONTROL AND ELECTROMECHANICS LABORATORY

TITLE: LOCATION WASHER

SIZE A | DWG. NO. | REV

SCALE: 1:1 | WEIGHT: | SHEET 1 OF 1

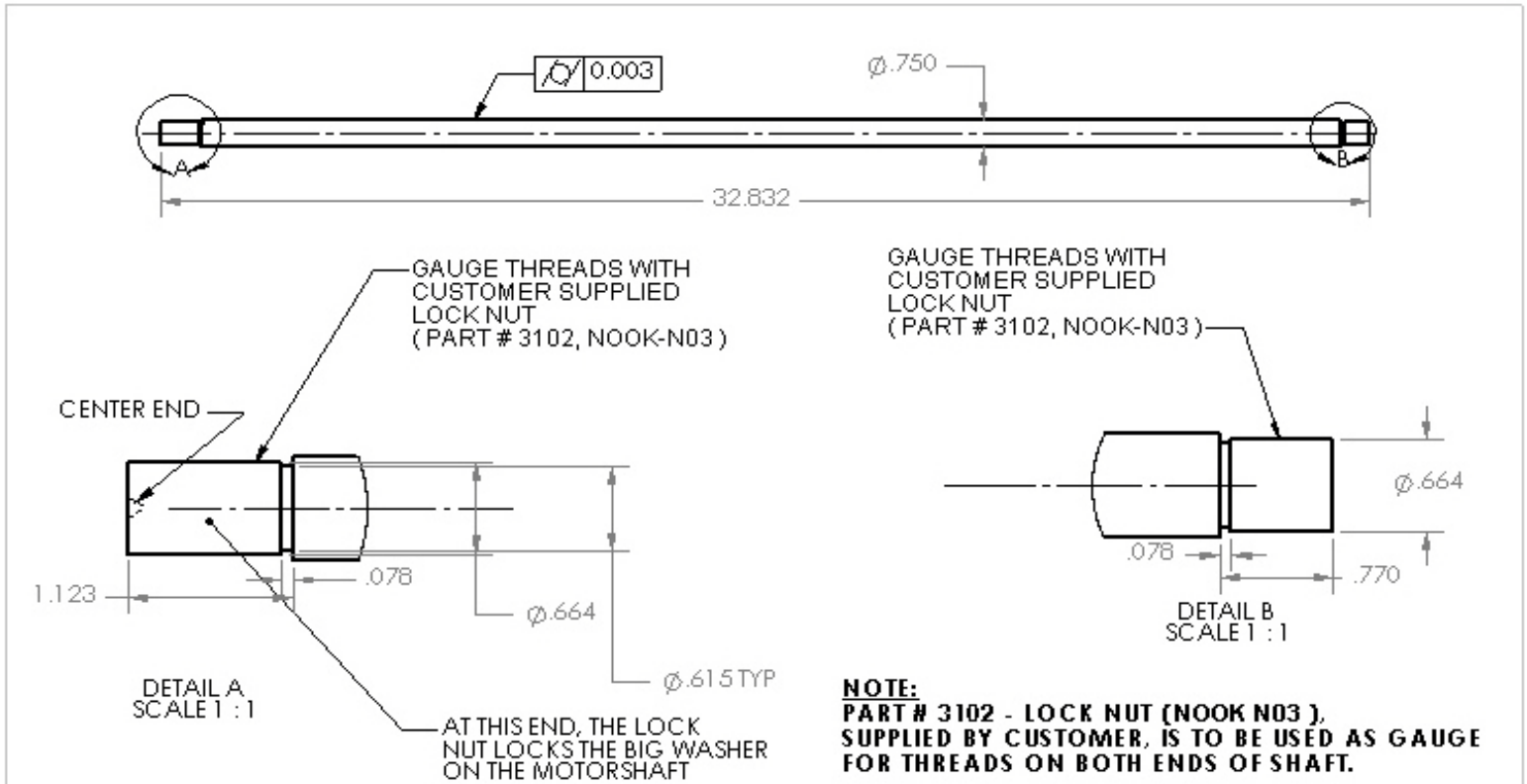


**NOTE:**
**PART # 3102 - LOCK NUT (NOOK N03 ), SUPPLIED BY CUSTOMER, IS TO BE USED AS GAUGE FOR THREADS ON BOTH ENDS OF SHAFT.**

UNLESS OTHERWISE SPECIFIED:

DIMENSIONS ARE IN INCHES
TOLERANCES:
FRACTIONAL ±1/64
ANGULAR: MACH ±1° BEND ±1°
TWO PLACE DECIMAL ±0.005
THREE PLACE DECIMAL ±0.001

INTERPRET GEOMETRIC TOLERANCING PER: ASME Y14.5M-1994

MATERIAL
INCONEL - 718

FINISH
UNLESS OTHERWISE SPECIFIED
125 MICROINCH RMS

| | NAME | DATE |
|---|---|---|
| DRAWN | VIBM | |
| CHECKED | | |
| ENG APPR | | |
| MFG APPR | | |
| Q A | | |

COMMENTS:
FOR DETAILS -
CONTACT 1)ASHWANTH
21479 68287
2)RANDY

VIBRATION CONTROL AND ELECTROMECHANICS LABORATORY

TITLE:
EEC MOTORSHAFT ROD

| SIZE | DWG. NO. | REV |
|---|---|---|
| A | | |



NEXT ASSY | USED ON

# VITA

Vishal Ashok Wadhvani was born in 1985 and grew up in Pune, Maharashtra, India. He graduated with his Bachelor's degree in Mechanical Engineering from the prestigious University of Pune in May 2007. After a year's hiatus to gain industrial exposure, he joined the Master's program with the Mechanical Engineering Department at Texas A&M University, in Fall 2008. He started working in the Vibration Control and Electromechanics Laboratory with Dr. Alan Palazzolo as his research advisor in the following spring semester and pursued research in the field of High Temperature Permanent Magnet Biased Magnetic Bearings and was awarded a Master of Science degree in Mechanical Engineering in May 2011. Vishal began employment in March, 2011 with FMC Technologies (Direct Drive Systems) as a Magnetic Bearing Control Engineer Intern.

Vishal may be reached at:

3123, Texas A&M University,

College Station, TX 77843-3123, USA

v.a.wadhvani@gmail.com